Microscope

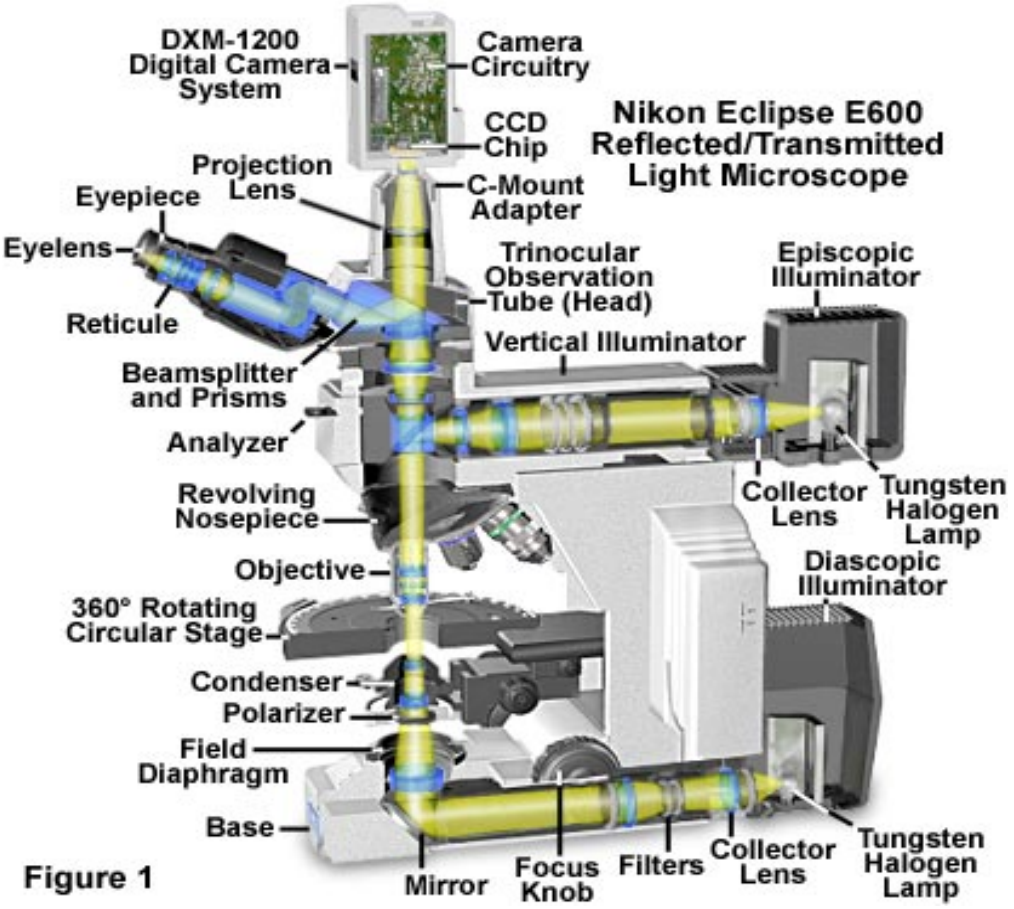

Figure 1

Diffraction Limit

$$d = \lambda/(2n \sin \alpha)$$

$$, k_0 = 2NA/\lambda_{em}$$

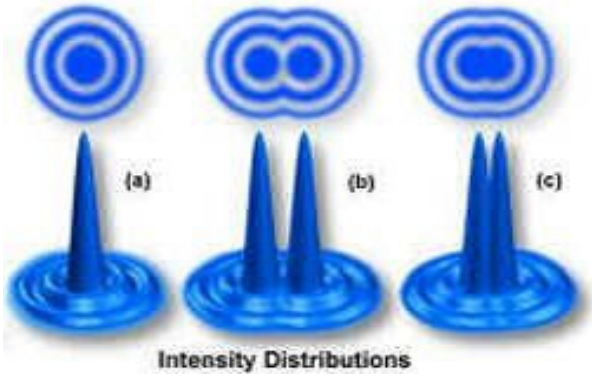

Confocal vs Wide Field

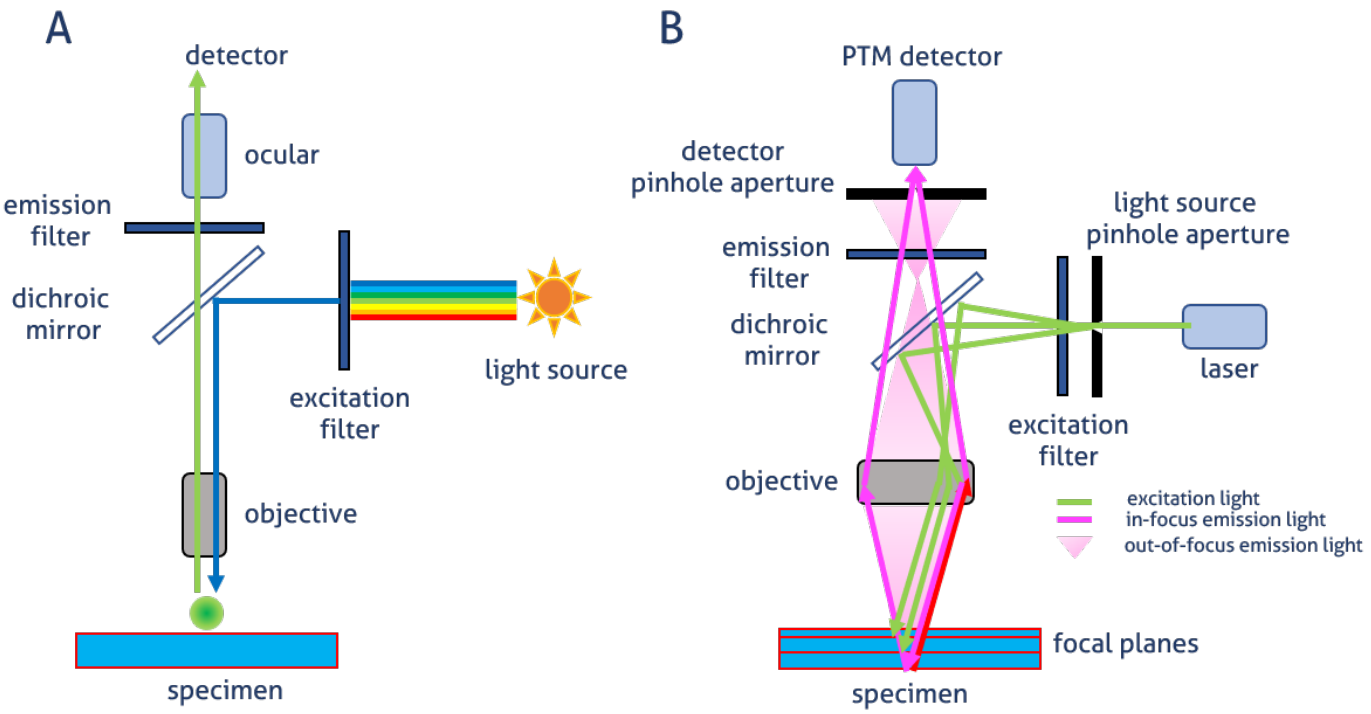

Confocal vs Wide Field

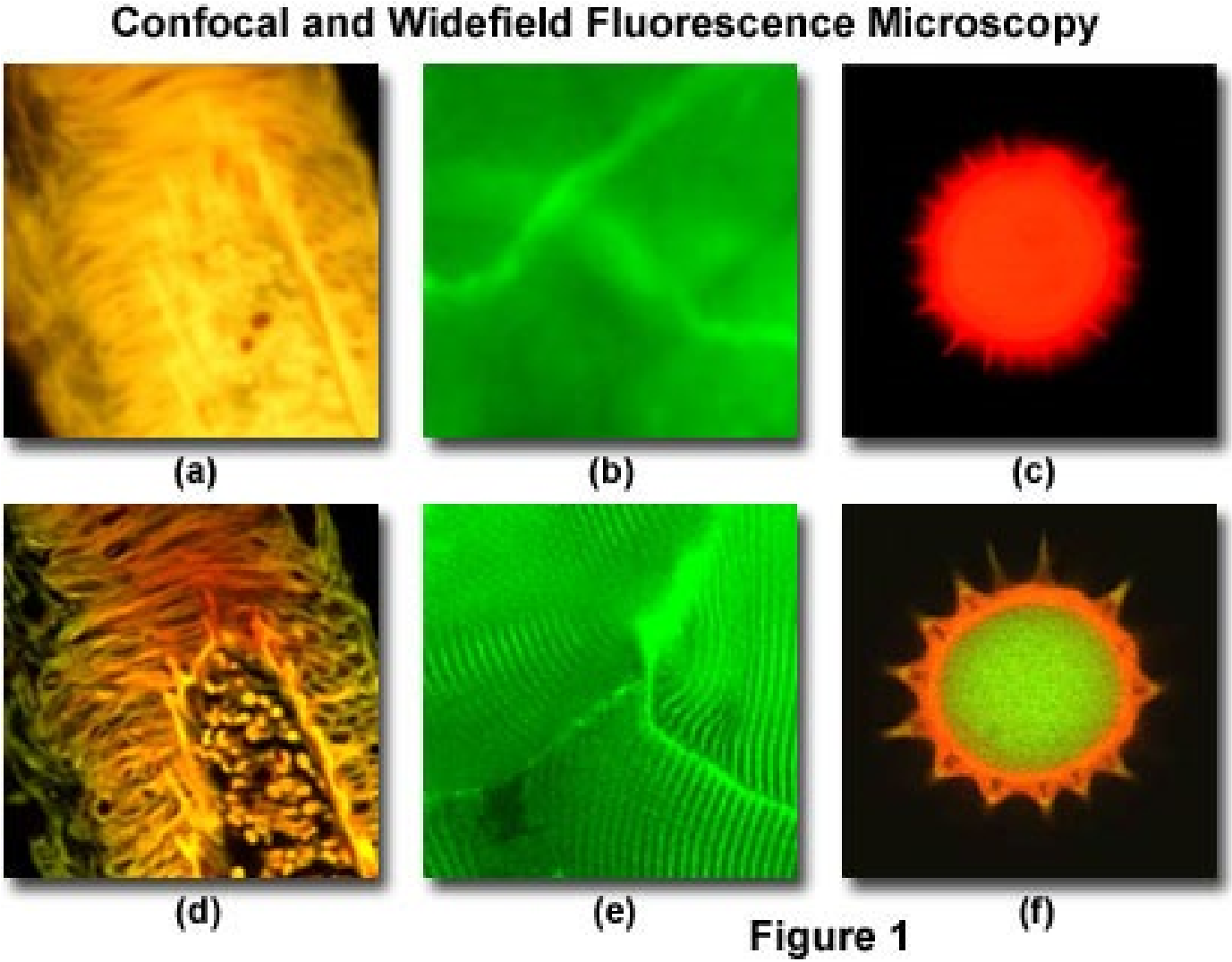

Super-Resolution Microscopy

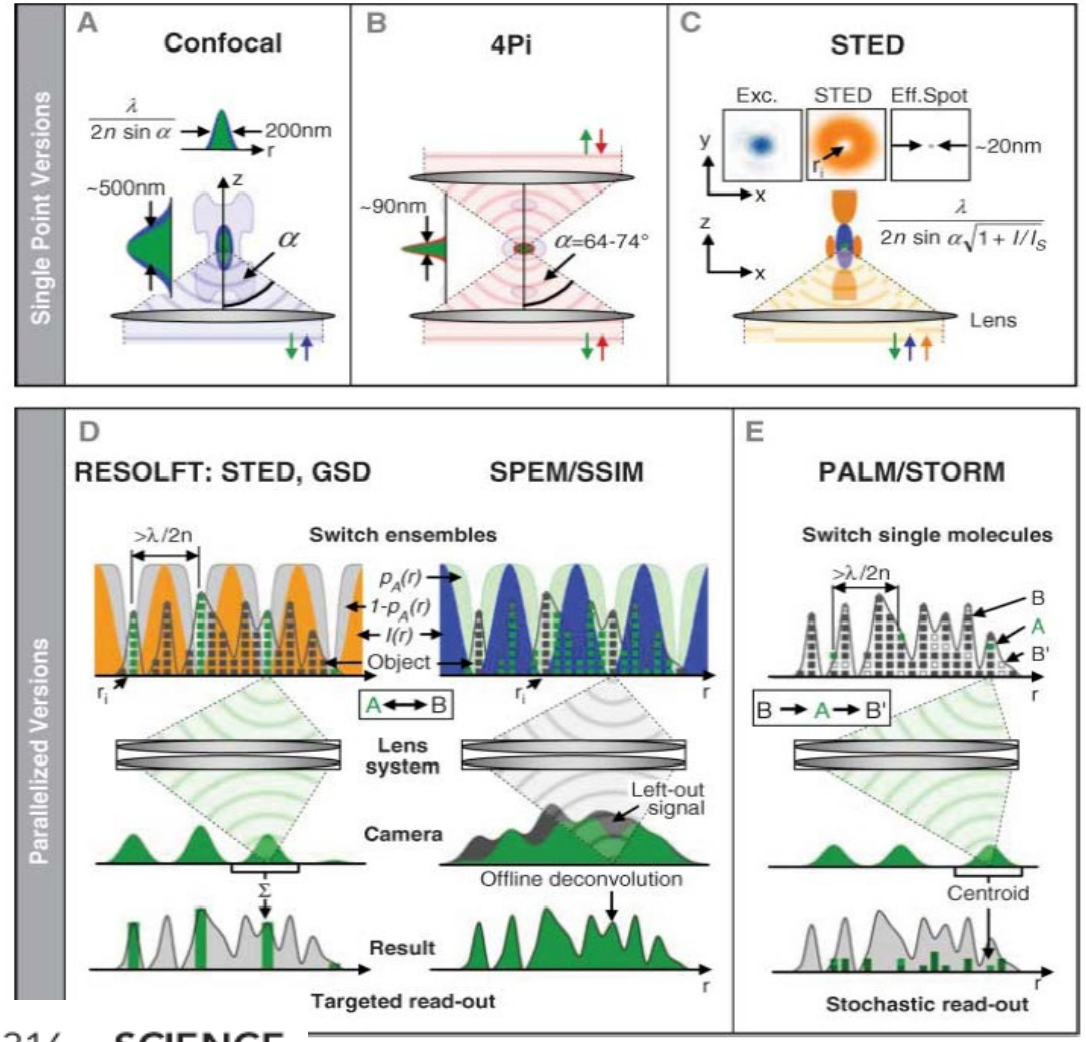

Localization

$$I(x, y) = I_{\text{background}} + A. \exp\left\{-1/2\left[\left(\frac{x - x_0}{s_x}\right)^2 + \left(\frac{y - y_0}{s_y}\right)^2\right]\right\},$$

$$\sigma^{\mu}_{x,y} = \sqrt{\frac{s^2_{x,y}}{N_{\text{photons}}} + \frac{a^2}{12.N_{\text{photons}}} + \frac{8.\pi.s^4_{x,y}.b^2}{a^2.N_{\text{photons}}}},$$

Photoactivation localization microscopy (PALM)

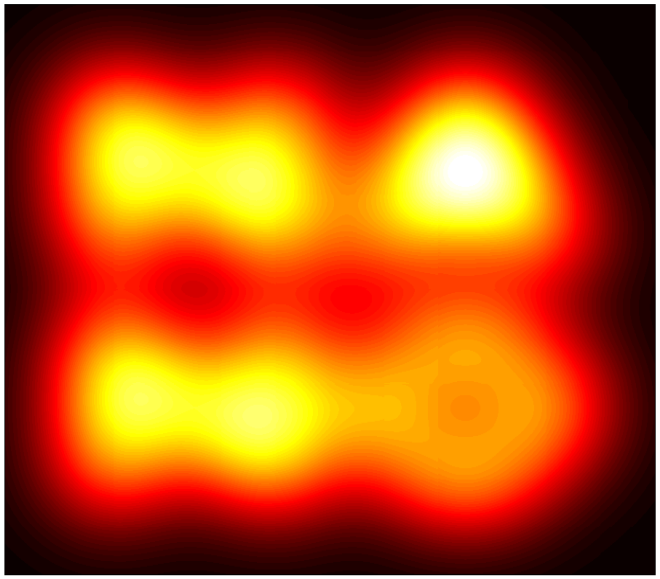

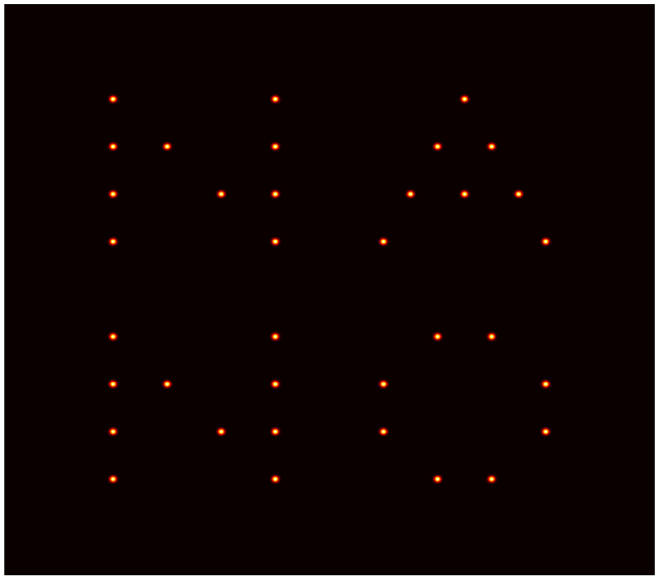

Diffraction-limited system:

Lateral resolution $\Delta xy \approx 0.61\,\lambda$ / N.A.
$\approx$ 200 nm

Axis resolution $\Delta z \approx 2\lambda$ / N.A.^{2}
$\approx$ 450 nm

Mean-squared position error:

$$\left(\sigma_{x,y}^2\right)_m \approx \frac{s^2 + a^2/12}{N_m} + \frac{4\sqrt{\pi}s^3 b_m^2}{aN_m^2}$$

s is the standard deviation of the PSF.
a is the pixel size in the image
N_m is the total number of photons measured from molecule *m*
b_m is the number of background photons collected in the fitting window

Russell E. Thompson, Daniel R. Larson, and Watt W. Webb, **Biophysical Journal** 82, 2775 (2002).
Eric Betzig, et al., **Science** 313, 1642 (2006).

Imaging Intracellular Fluorescent Proteins at Nanometer Resolution

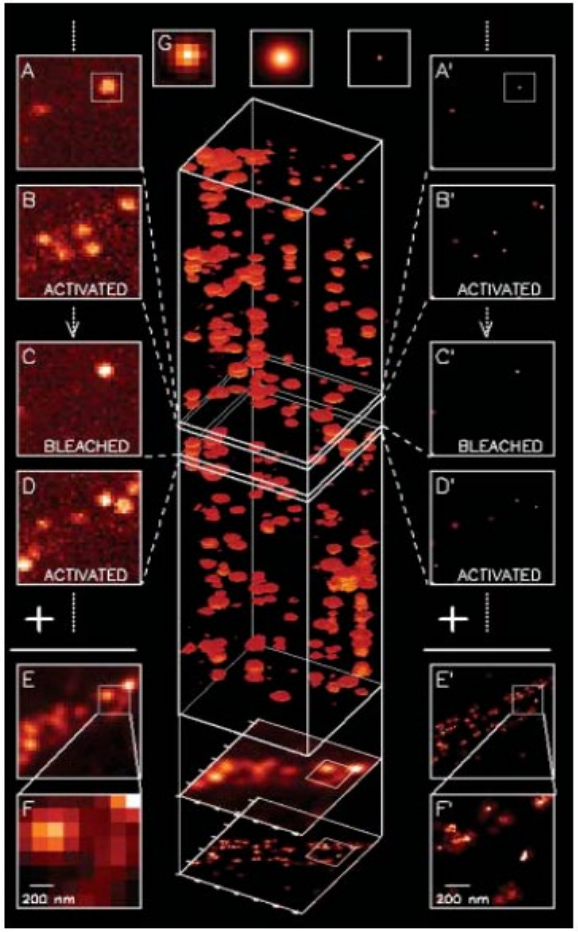

$$(\sigma_{x,y}{}^2)_m \approx \frac{s^2 + a^2/12}{N_m} + \frac{4\sqrt{\pi}s^3 b_m{}^2}{aN_m{}^2}$$

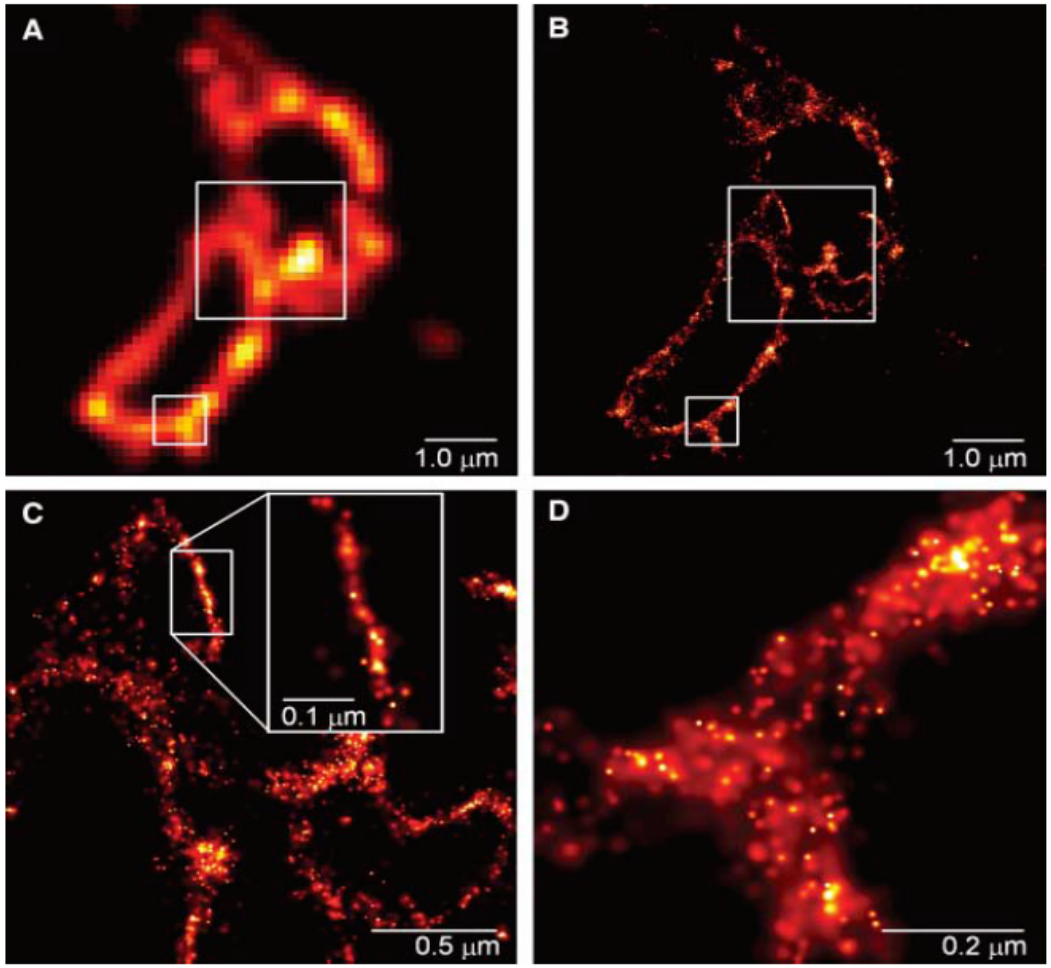

Fig. 2. Comparative summed-molecule TIRF (**A**) and PALM (**B**) images of the same region within a cryo-prepared thin section from a COS-7 cell expressing the lysosomal transmembrane protein CD63 tagged with the PA-FP Kaede. The larger boxed region in (B), when viewed at higher magnification (**C**) reveals smaller associated membranes that may represent interacting lysosomes or late endosomes that are not resolvable by TIRF. In a region where the section is nearly orthogonal to the lysosomal membrane, the most highly localized molecules fall on a line of width ~10 nm (inset). In an obliquely cut region [(**D**), from the smaller boxed region in (B)], the distribution of CD63 within the membrane plane can be discerned.

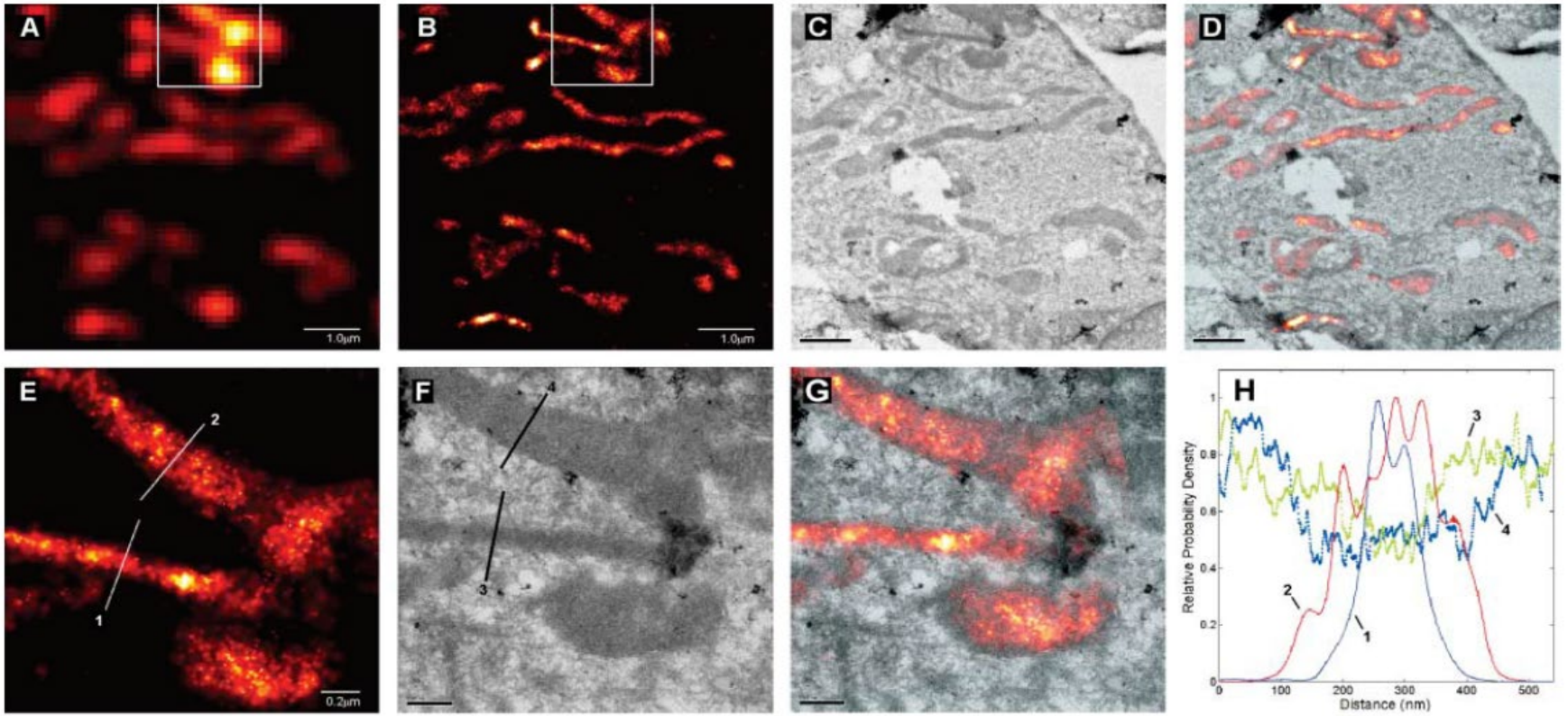

Fig. 3. Comparative summed-molecule TIRF (**A**), PALM (**B**), TEM (**C**), and PALM/TEM overlay (**D**) images of mitochondria in a cryo-prepared thin section from a COS-7 cell expressing dEosFP-tagged cytochrome-C oxidase import sequence. Higher magnification PALM (**E**), TEM (**F**), and overlay (**G**) images within the box in (B) reveal that these matrix reporter molecules extend up to, but not into, the ~20-nm outer mitochondrial membrane. The molecular distribution across two mitochondria along lines 1 and 2 in PALM image (E) are compared in (**H**) to the TEM signal along lines 3 and 4 in (F) across the same mitochondria. Scale bars: 1.0 μm in (A) to (D); 0.2 μm in (E) to (G).

Sub-diffraction-limit imaging by stochastic optical reconstruction microscopy (STORM)

Michael J Rust[1,5], Mark Bates[2,5] & Xiaowei Zhuang[1,3,4]

NATURE METHODS

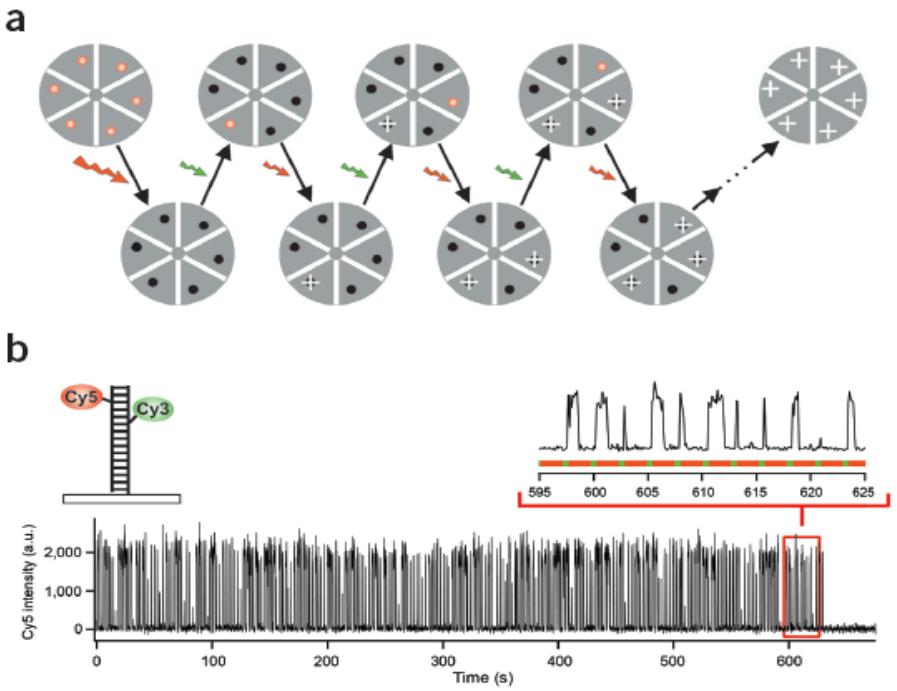

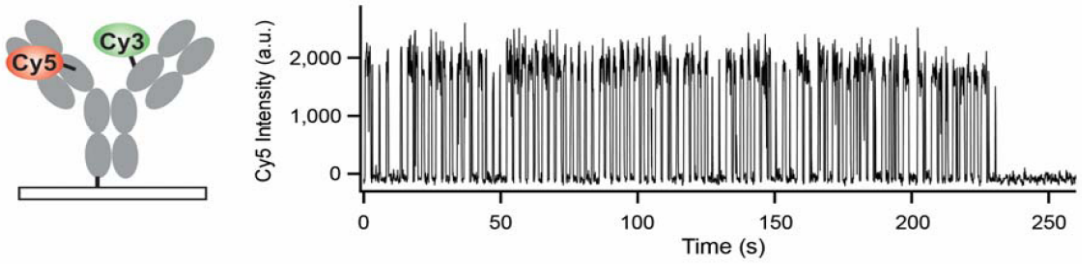

: 2.2 : 1 for Cy3 and 0.1 : 1 for Cy5

Goat anti-mouse secondary antibody labeled with the cyanine switch exhibits photoswitching behavior similar to switch-labeled DNA. The antibody was labeled with Cy3 and Cy5 (as described in **Supplementary Methods** online) and bound to a quartz slide coated with unlabeled mouse anti-transferrin primary antibody. The trace shows the Cy5 fluorescence intensity detected from a single labeled antibody as it switches on and off until permanent photobleaching occurs after 230 seconds. A red laser (633 nm, 30 W/cm^2) is used to excite fluorescence from Cy5 and to switch Cy5 to the dark state. A green laser (532 nm, 1 W/cm^2) is used to switch the Cy5 back to the fluorescent state. The sample was excited with a sequence of alternating green and red laser pulses (0.5 s green followed by 2 s red).

$$I(x,y) = A + I_0 e^{\left[-(x'/a)^2-(y'/b)^2\right]/2}$$

$$x' = (x - x_0)\cos\theta - (y - y_0)\sin\theta$$
$$y' = (x - x_0)\sin\theta + (y - y_0)\cos\theta$$

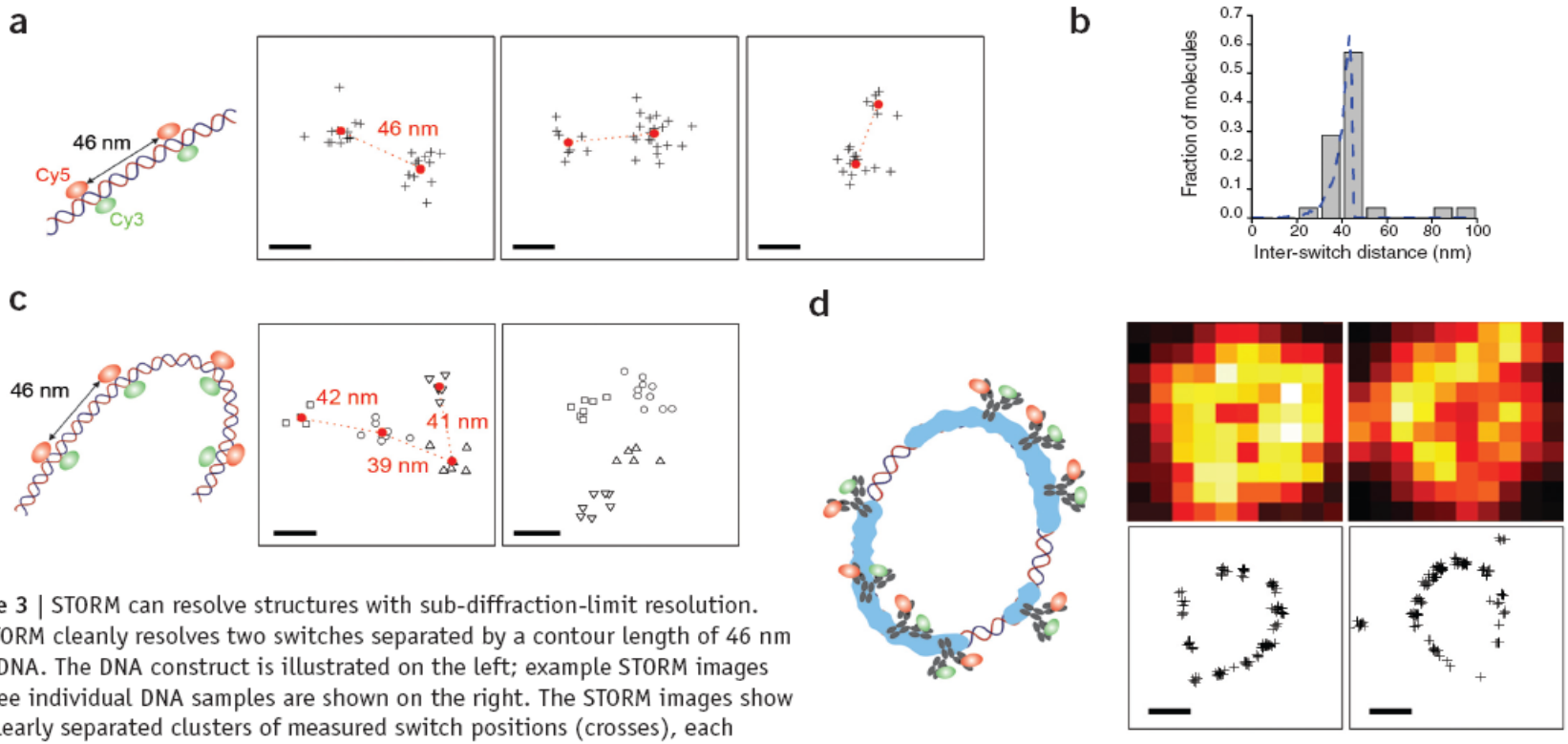

Figure 3 | STORM can resolve structures with sub-diffraction-limit resolution. (**a**) STORM cleanly resolves two switches separated by a contour length of 46 nm on dsDNA. The DNA construct is illustrated on the left; example STORM images of three individual DNA samples are shown on the right. The STORM images show two clearly separated clusters of measured switch positions (crosses), each corresponding to a single switch. The center-of-mass position of each cluster is marked by a red dot. The inter-switch distances are 46 nm, 44 nm and 34 nm for these three examples. Scale bars, 20 nm. (**b**) Comparison between the inter-switch distances measured using STORM (columns) and the predicted distance distribution considering the flexibility of DNA (dashed line). (**c**) STORM images of four switches attached to a dsDNA, pair-wise separated by a contour length of 46 nm. The measured switch positions are clustered by an automated algorithm and different clusters are indicated by different symbols. Scale bars, 20 nm. (**d**) STORM images of RecA-coated circular plasmid DNA. Indirect immunofluorescence images with switch-labeled secondary antibody taken by a total internal reflection microscope (top); the reconstructed STORM images of the same filaments (bottom). Scale bars, 300 nm.

Multicolor Super-Resolution Imaging with Photo-Switchable Fluorescent Probes

SCIENCE VOL 317 21 SEPTEMBER 2007

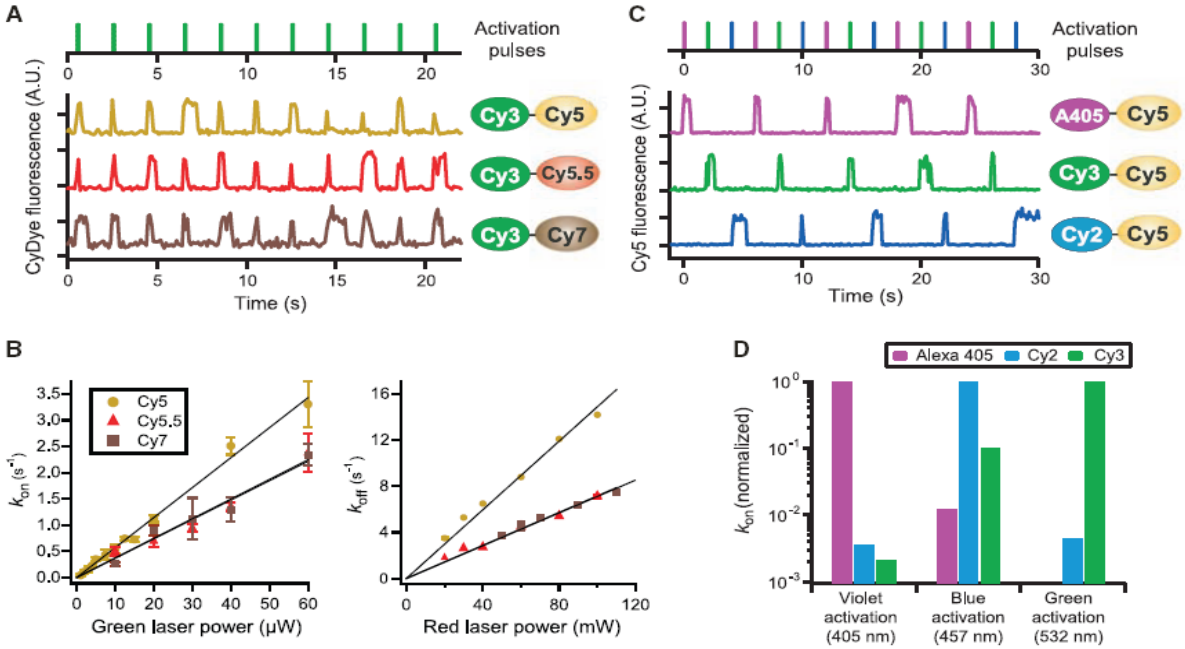

Fig. 1. Photo-switchable probes constructed from activator-reporter pairs. (**A**) Spectrally distinct reporters exhibit photo-switching behavior. The lower panel shows the fluorescence time traces of three photo-switchable reporters Cy5 (dark yellow line), Cy5.5 (red line), and Cy7 (brown line), each paired with a Cy3 dye as the activator on a DNA construct. The upper panel shows the green laser pulses (532 nm) used to activate the reporters. The red laser (657 nm) was continuously on, serving to excite fluorescence from the reporters and to switch them to the dark state. Traces were shifted relative to each other for clarity. (**B**) Switching rate constants k_{on} and k_{off} of the Cy3-Cy5, Cy3-Cy5.5, and Cy3-Cy7 pairs as a function of green and red laser power. Error bars indicate SEM from about three data sets. The laser power to intensity calibration may vary between different samples because of moderate differences in the laser spot size at the sample. (**C**) The same reporter can be activated by spectrally distinct activators. The lower panel shows the fluorescence time traces of Cy5 paired with three different activators, Alexa 405 (magenta line), Cy2 (blue line), and Cy3 (green line). The upper panel shows the violet (405 nm, magenta line), blue (457 nm, blue line), and green (532 nm, green line) activation pulses. (**D**) Normalized activation rate constants of the three dye pairs at three activation wavelengths: 405, 457, and 532 nm. The k_{on} values of Alexa 405-Cy5, Cy2-Cy5, and Cy3-Cy5 were used for normalization at 405, 457, and 532 nm, respectively. The absolute activation rates were rapid for each pair at its corresponding optimal wavelength, with values of 10 s^{-1} or greater at only a few hundred μW of laser power. The activation rate of the Alexa 405-Cy5 pair by the 532-nm laser was too small to be measured reliably.

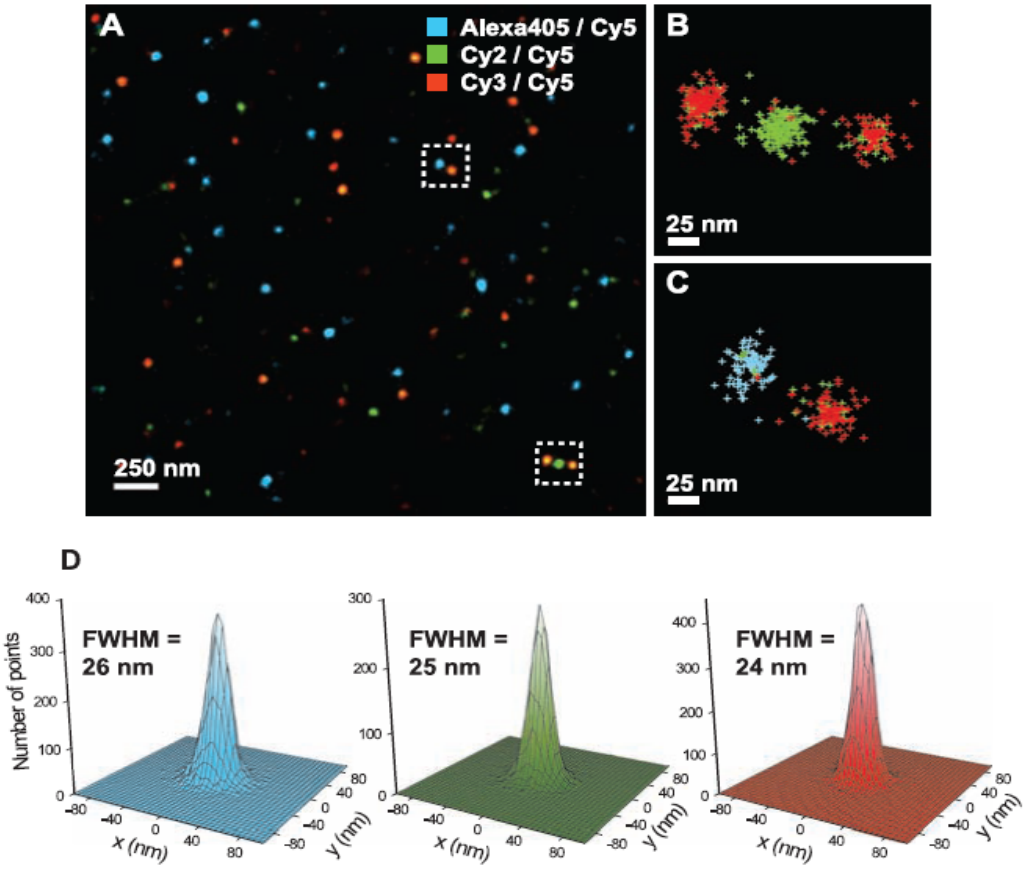

Fig. 2. Three-color STORM imaging of a model DNA sample. (**A**) Three-color STORM image of three different DNA constructs labeled with Alexa 405-Cy5, Cy2-Cy5, or Cy3-Cy5 mixed at a high surface density on a microscope slide. The image was plotted by rendering each localization as a Gaussian peak, the width of which was scaled with the theoretical localization accuracy given by the number of photons detected (*26*). Each colored spot in this image represents a cluster of localizations from a single DNA molecule. A conventional fluorescence image of the same area is shown in fig. S3 for comparison. (**B** and **C**) Higher-magnification views of the boxed regions in (A) show several examples of closely spaced DNA molecules. Each localization was plotted as a cross, colored according to the following code: If the molecule was activated by a 405-, 457-, or 532-nm laser pulse, the color of the cross was assigned as blue, green, or red, respectively. (**D**) The localization distributions of the blue, green, or red clusters. The two-dimensional histograms of localizations were generated by aligning multiple (50 to 60) clusters by their center of mass. The histograms were fit to a Gaussian profile to determine their FWHM.

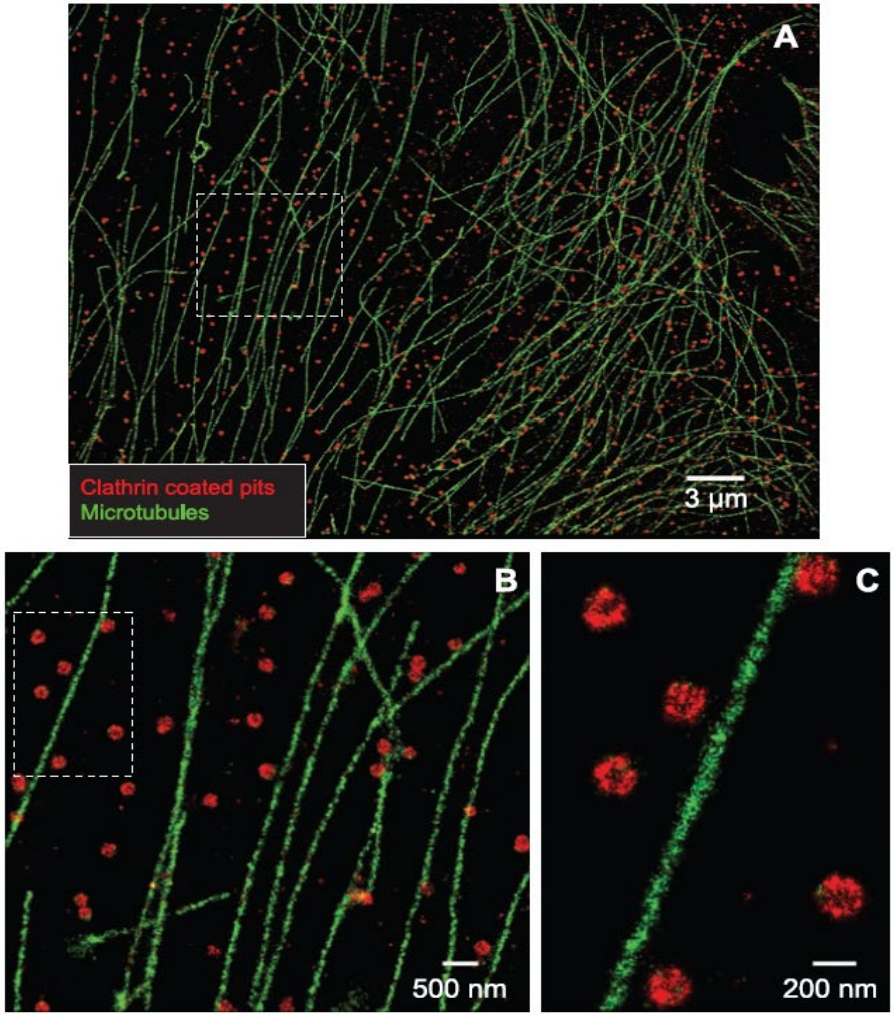

Fig. 4. Two-color STORM imaging of microtubules and CCPs in a mammalian cell. (**A**) STORM image of a large area of a BS-C-1 cell. The secondary antibodies used for microtubule staining were labeled with Cy2 and Alexa 647, and those for clathrin were labeled with Cy3 and Alexa 647. The 457- and 532-nm laser pulses were used to selectively activate the two pairs. Each localization was false colored according to the following code: green for 457-nm activation and red for 532-nm activation. (**B**) STORM image corresponding to the boxed region in (A) shown at a higher magnification. (**C**) Further magnified view of the boxed region in (B).

Three-Dimensional Super-Resolution Imaging by Stochastic Optical Reconstruction Microscopy

8 FEBRUARY 2008 VOL 319 SCIENCE

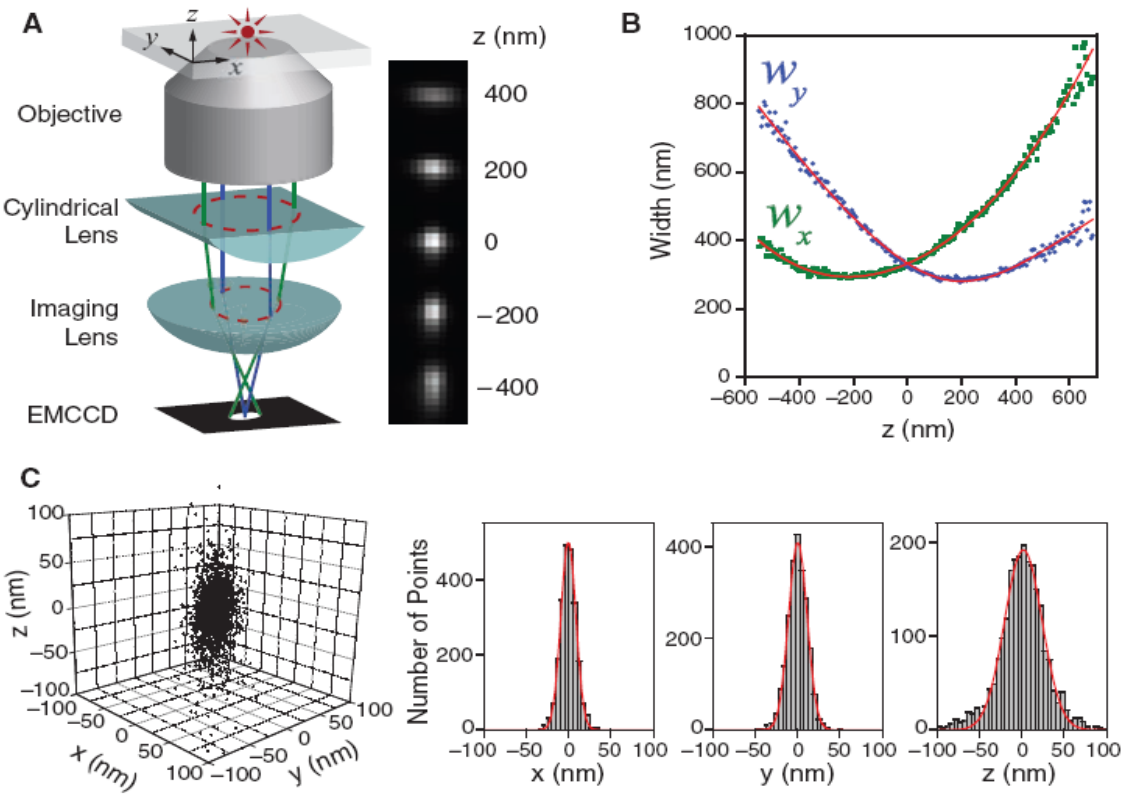

Fig. 1. The scheme of 3D STORM. (**A**) Three-dimensional localization of individual fluorophores. The simplified optical diagram illustrates the principle of determining the *z* coordinate of a fluorescent object from the ellipticity of its image by introducing a cylindrical lens into the imaging path. The right panel shows images of a fluorophore at various *z* positions. EMCCD, electron-multiplying charge-coupled device. (**B**) Calibration curve of image widths w_x and w_y as a function of *z* obtained from single Alexa 647 molecules. Each data point represents the average value obtained from six molecules. The data were fit to a defocusing function (red curve) as described in (*27*). (**C**) Three-dimensional localization distribution of single molecules. Each molecule gives a cluster of localizations due to repetitive activation of the same molecule. Localizations from 145 clusters were aligned by their center of mass to generate the overall 3D presentation of the localization distribution (left panel). Histograms of the distribution in *x*, *y*, and *z* (right panels) were fit to a Gaussian function, yielding standard deviations of 9 nm in *x*, 11 nm in *y*, and 22 nm in *z*.

Fig. 2. Three-dimensional STORM imaging of microtubules in a cell. (**A**) Conventional indirect immunofluorescence image of microtubules in a large area of a BS-C-1 cell. (**B**) The 3D STORM image of the same area, with the *z*-position information color-coded according to the color scale bar. Each localization is depicted in the STORM image as a Gaussian peak, the width of which is determined by the number of photons detected (*5*). (**C** to **E**) The *x*-*y*, *x*-*z*, and *y*-*z* cross sections of a small region of the cell outlined by the white box in (B), showing five microtubule filaments. Movie S1 shows the 3D representation of this region, with the viewing angle rotated to show different perspectives (*27*). (**F**) The *z* profile of two microtubules crossing in the *x*-*y* projection but separated by 102 nm in *z*, from a region indicated by the arrow in (B). The histogram shows the distribution of *z* coordinates of the localizations, fit to two Gaussians with identical widths (FWHM = 66 nm) and a separation of 102 nm (red curve). The apparent width of 66 nm agrees quantitatively with the convolution of our imaging resolution in *z* (represented by a Gaussian function with FWHM of 55 nm) and the previously measured width of antibody-coated microtubules (represented by a uniform distribution with a width of 56 nm) (*5*).

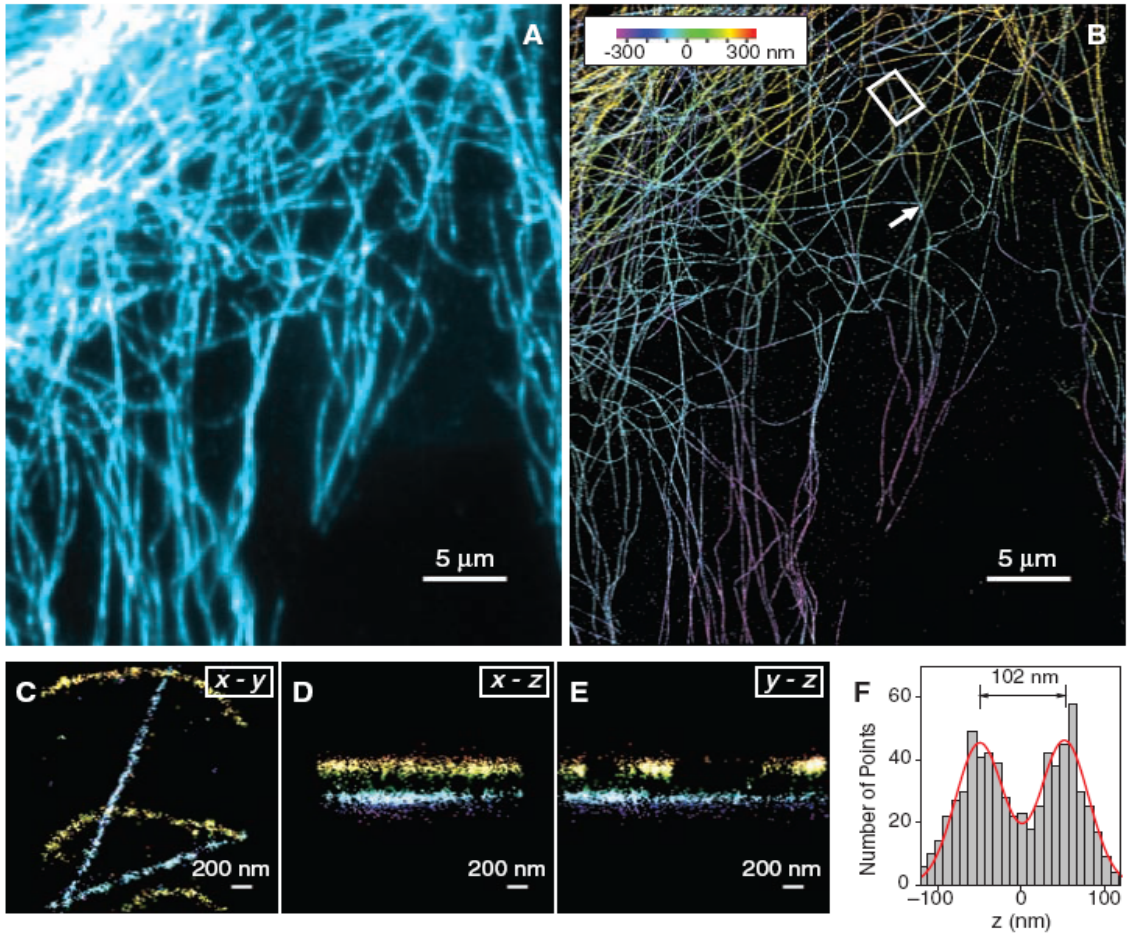

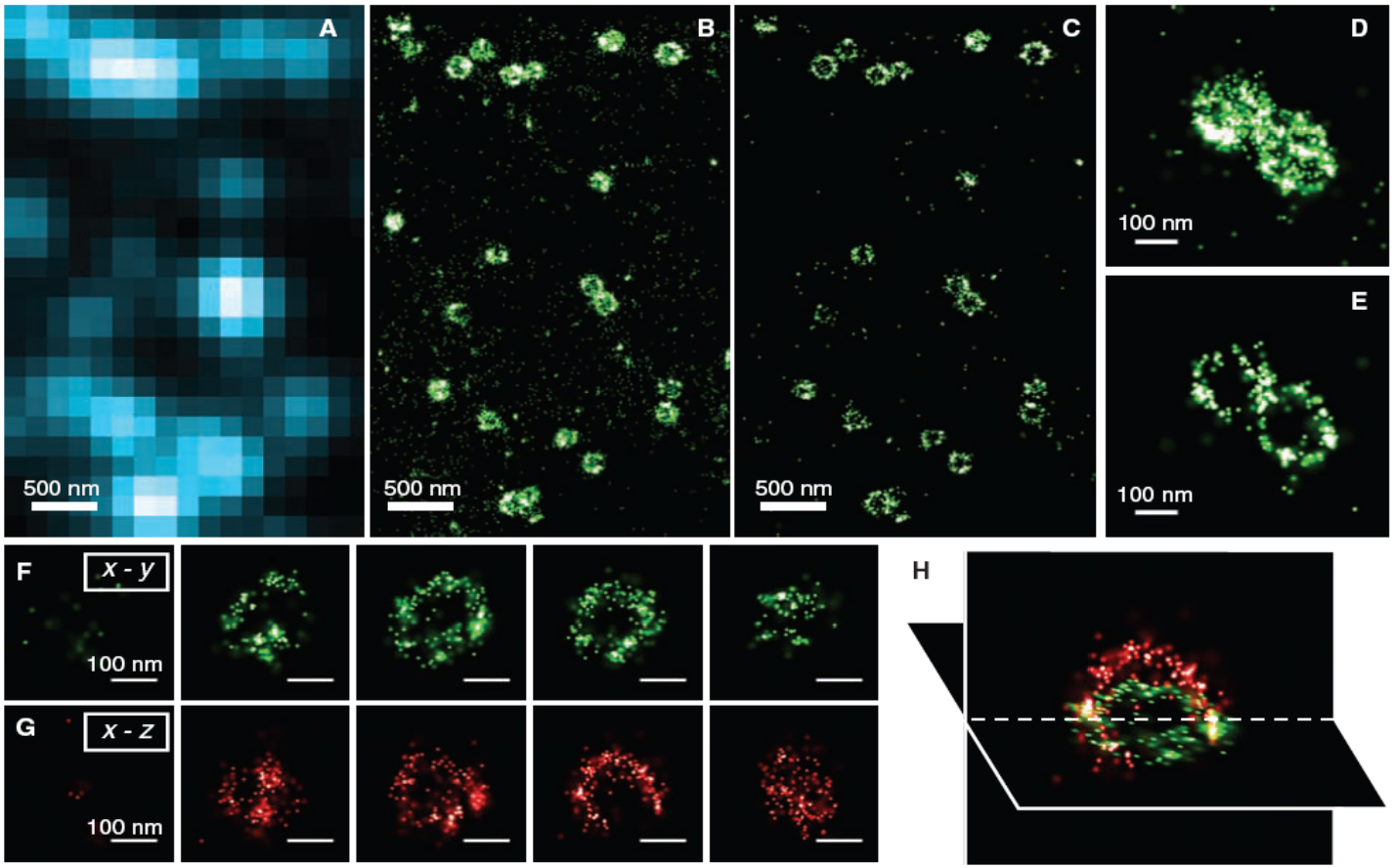

Fig. 3. Three-dimensional STORM imaging of clathrin-coated pits in a cell. (**A**) Conventional direct immunofluorescence image of clathrin in a region of a BS-C-1 cell. (**B**) The 2D STORM image of the same area, with all localizations at different *z* positions included. (**C**) An *x-y* cross section (50 nm thick in *z*) of the same area, showing the ring-like structure of the periphery of the CCPs at the plasma membrane. (**D** and **E**) Magnified view of two nearby CCPs in 2D STORM (D) and their *x-y* cross section (100 nm thick) in the 3D image (E). (**F** to **H**) Serial *x-y* cross sections (each 50 nm thick in *z*) (F) and *x-z* cross sections (each 50 nm thick in *y*) (G) of a CCP, and an *x-y* and *x-z* cross section presented in 3D perspective (H), showing the half-spherical cage-like structure of the pit.

Appl. Phys. B 60, 495–497 (1995)

Applied Physics B Lasers and Optics

Rapid communication

Ground-state-depletion fluorscence microscopy: a concept for breaking the diffraction resolution limit

S.W. Hell, M. Kroug

Department of Medical Physics, University of Turku, and Centre for Biotechnology, P.O. Box 123, FIN-20521 Turku, Finland
(Fax: +358-21/633-8000, E-mail: STEFAN.HELL@utu.fi)

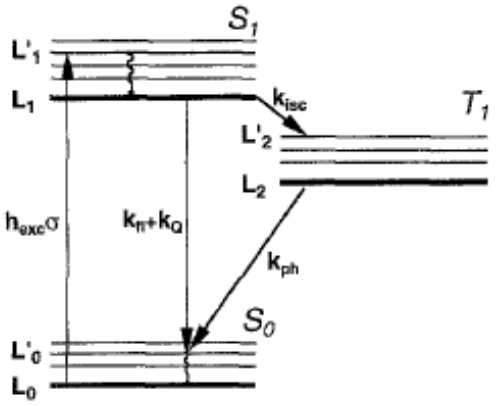

Fig. 1. Energy states of a typical dye: S_0 is the ground state, S_1 is the first singlet state, and T_1 the first triplet state

Direct stochastic optical reconstruction microscopy (dSTORM)

Reversible photoswitching mechanism of standard fluorophores

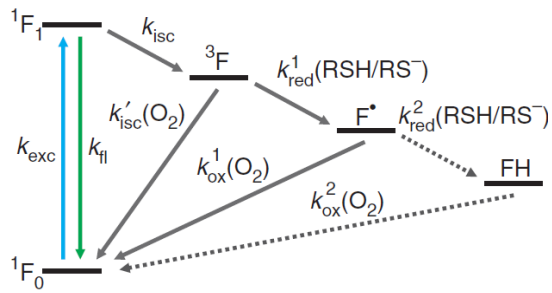

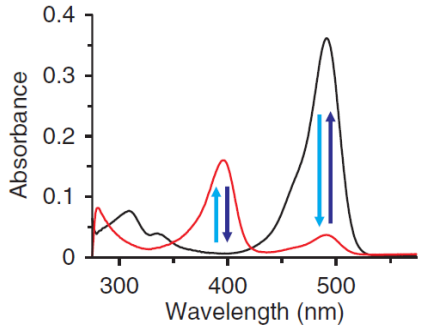

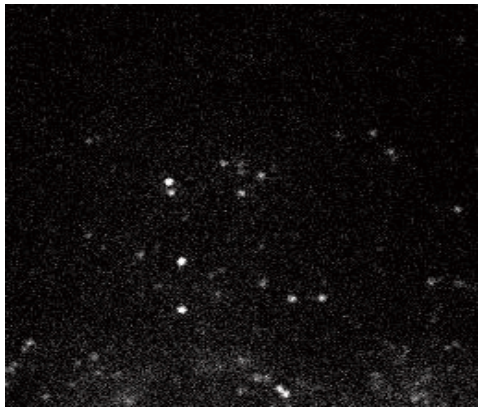

Localization imaging concept

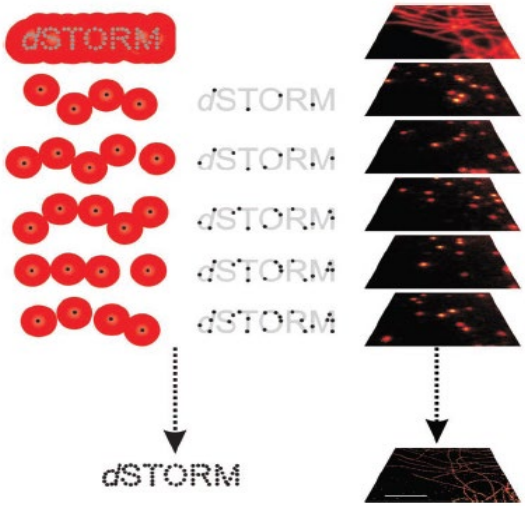

Multicolor imaging

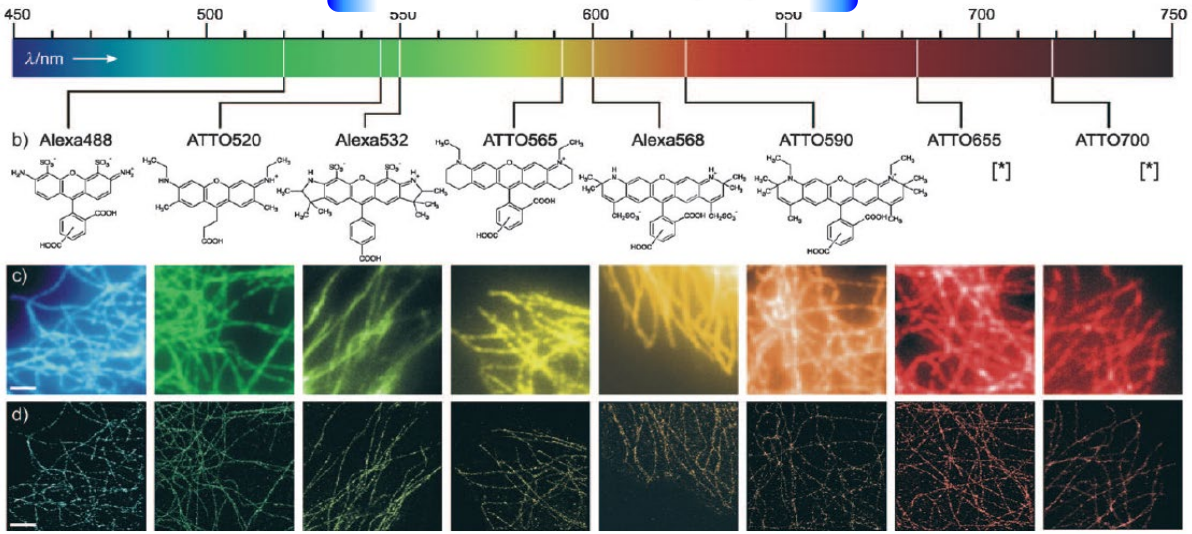

Angew. Chem. Int. Ed. 2008, 2009, Nature protocols 2011

Multicolor superresolution fluorescence imaging

Objective

1. Characteristic distance between focal adhesion complexes.
2. Cross-correlation between different focal adhesion complexes.
3. Number of focal adhesion complexes at different adhesion types.

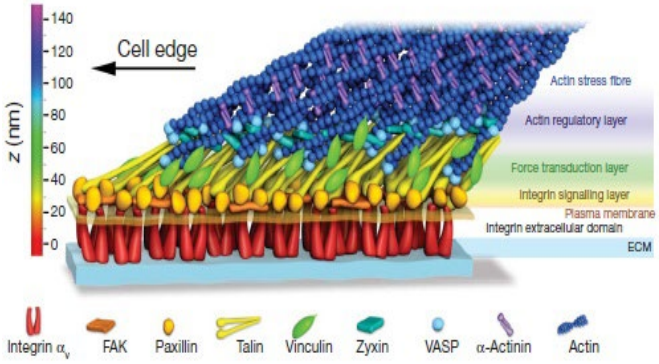

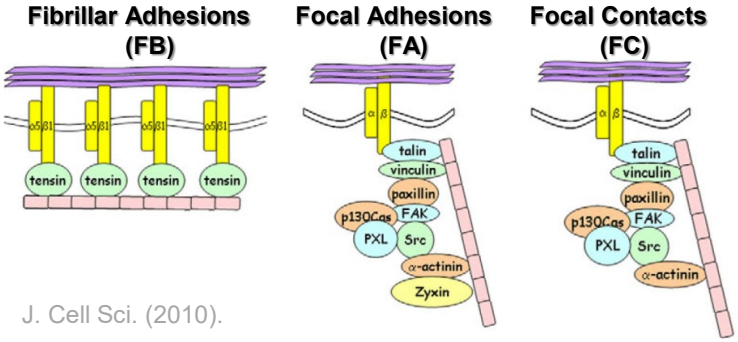

J. Cell Sci. (2010).

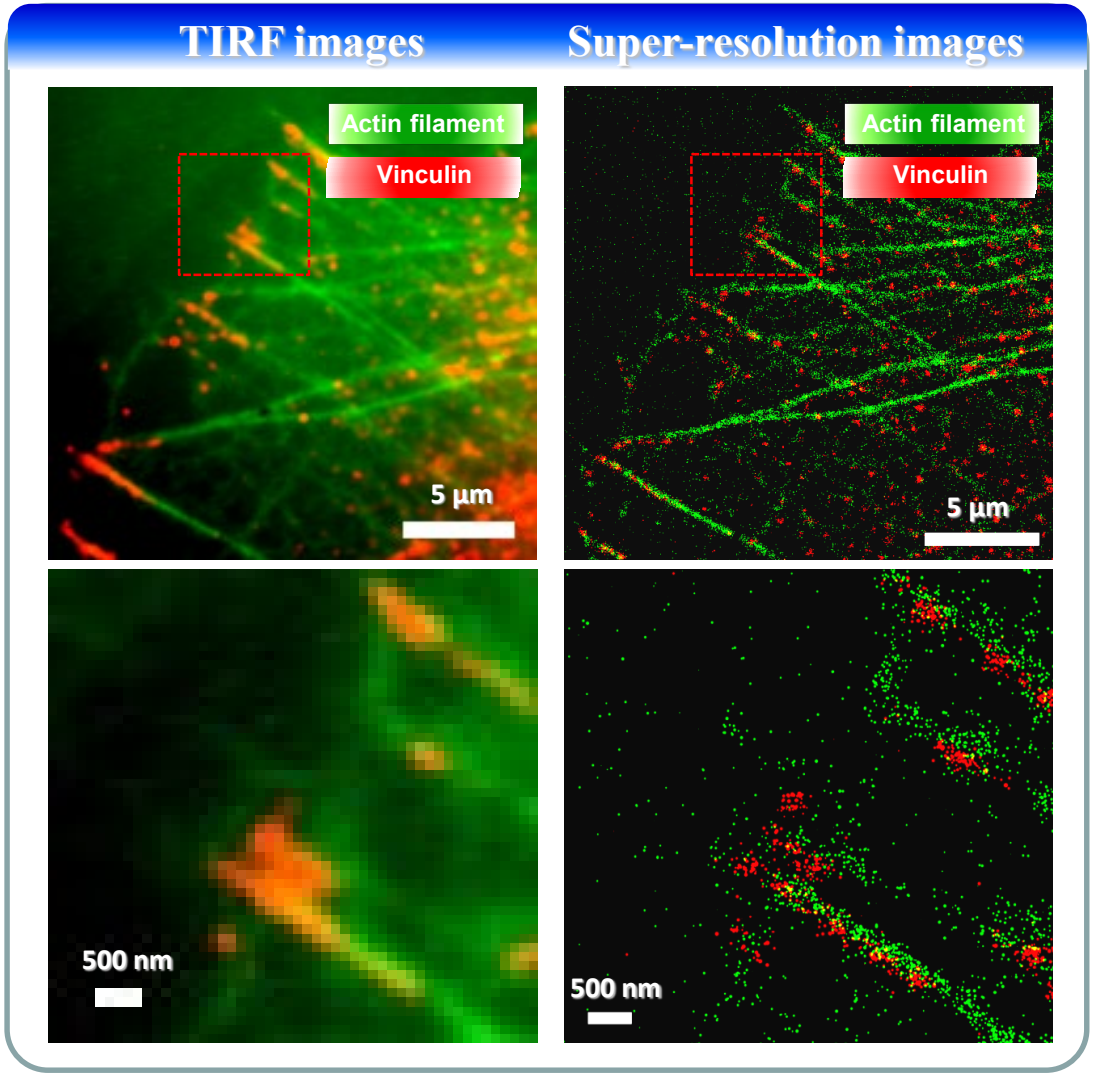

4 Pi

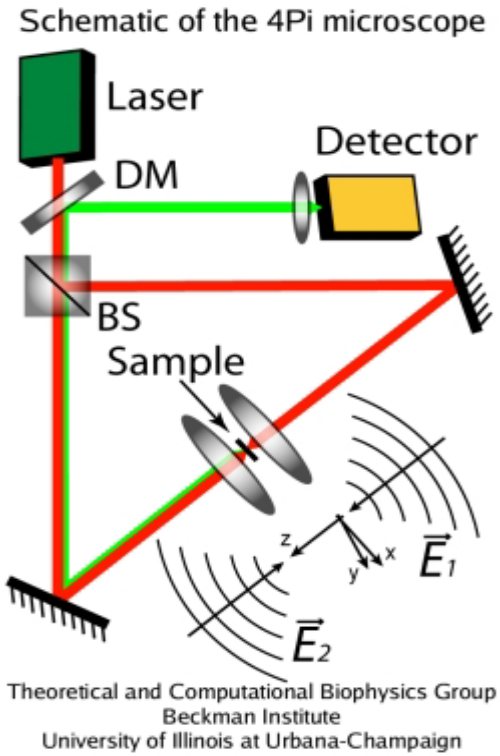
Schematic of the 4Pi microscope
Laser
Detector
DM
BS
Sample
$\vec{E}_1$
$\vec{E}_2$
Theoretical and Computational Biophysics Group
Beckman Institute
University of Illinois at Urbana-Champaign

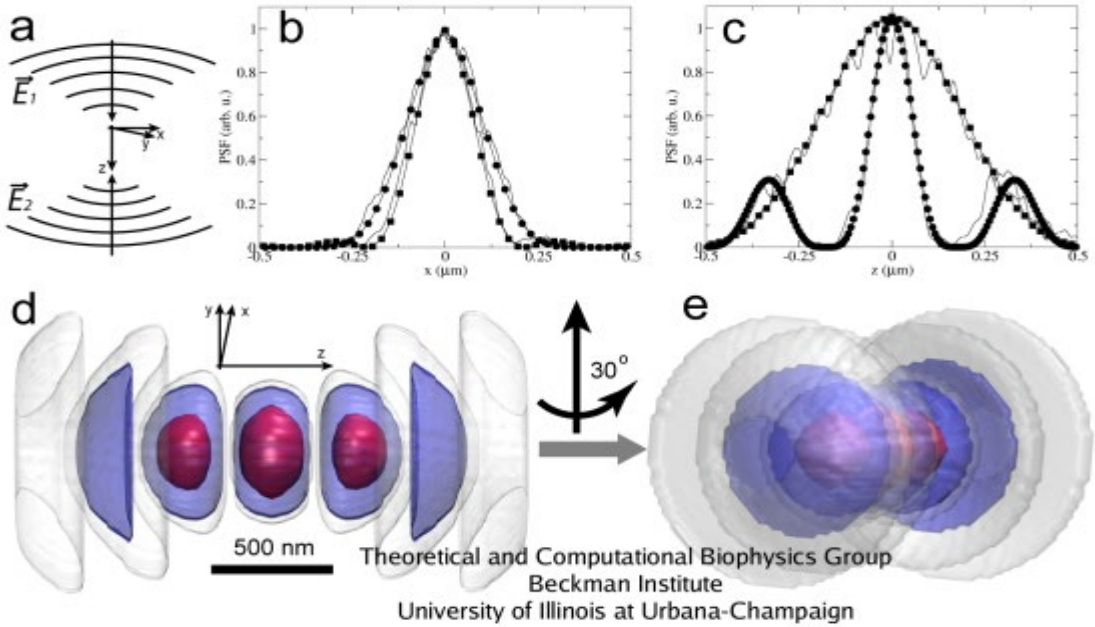
a
b
c
d
e
$\vec{E}_1$
$\vec{E}_2$
PSF (arb. u.)
x (μm)
z (μm)
30°
500 nm
Theoretical and Computational Biophysics Group
Beckman Institute
University of Illinois at Urbana-Champaign

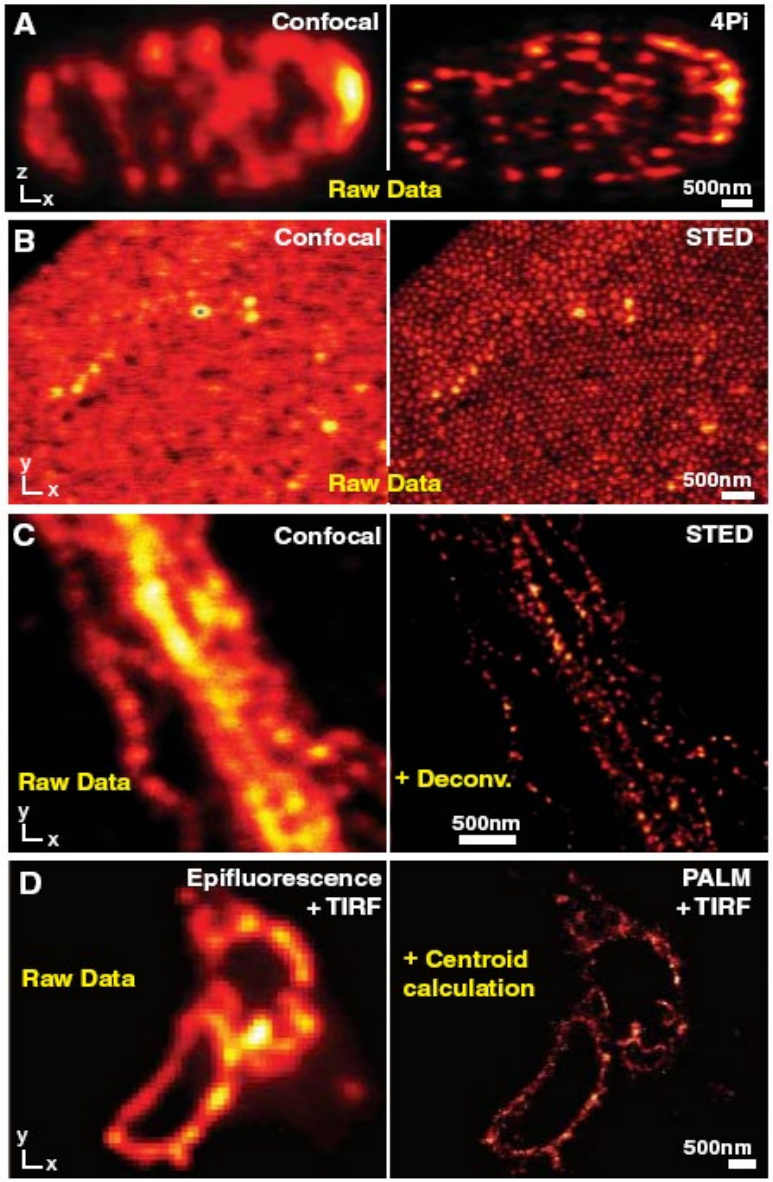

Fig. 4. Side-by-side comparisons. (**A**) Confocal versus 4Pi axial (*xz*) image of microtubules in a neuron: 4Pi image displays 140-nm *z* resolution; lens of $\alpha = 74°$ and with two-photon excitation at 800 nm. The plain 4Pi image is due to a narrow solitary peak without lobes; mathematical lobe-removal is not required. (**B**) Unlike the confocal reference, the STED image reveals the spatial order of self-assembled fused silica nanobeads containing a fluorescence core (*45*). (**C**) Neurofilaments in human neuroblastoma recorded in the confocal mode (left) and with STED after nonlinear deconvolution (right) displaying a focal plane resolution of 20 to 30 nm (*39*). (**D**) Epifluorescence versus PALM recording of a cryoprepared section from a mammalian cell expressing a lysosomal transmembrane protein tagged with a photoswitchable protein; both images were recorded with a TIRF setup. PALM resolution ranges between 20 and 60 nm, whereas individual protein localizations can be 2 nm (*12*).

STED microscopy

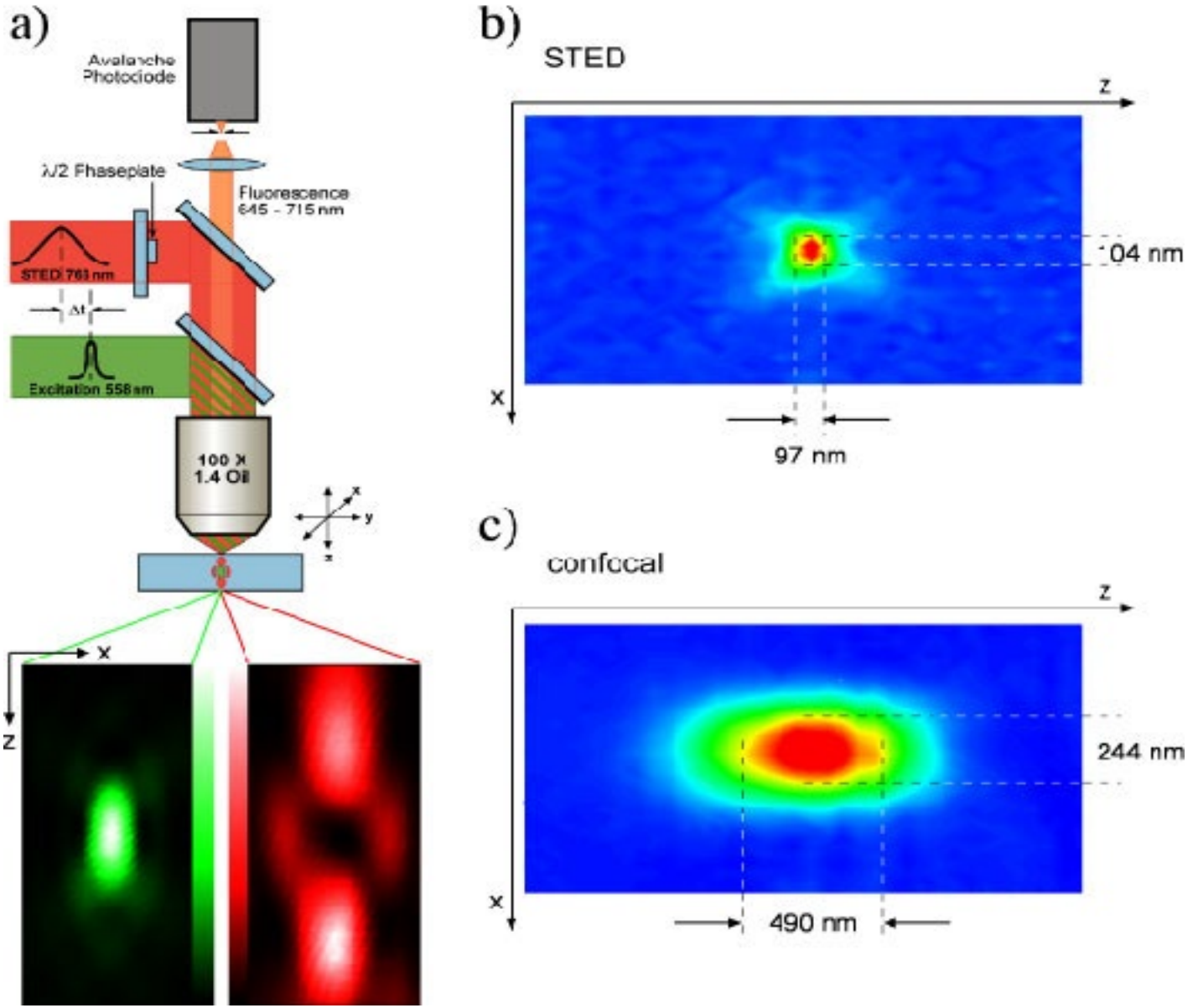

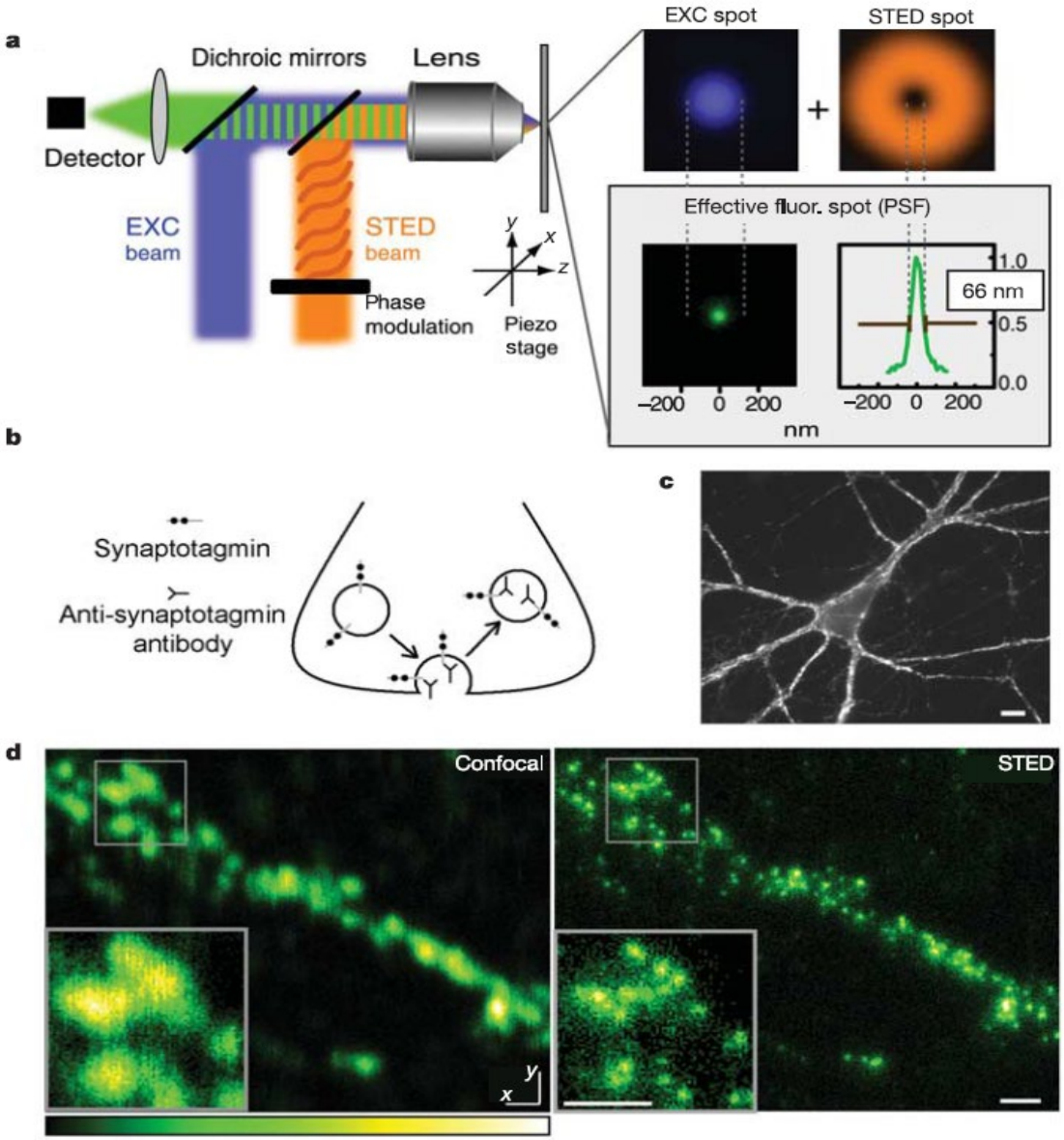
a
Dichroic mirrors
Lens
Detector
EXC beam
STED beam
Phase modulation
Piezo stage
y
x
z
EXC spot
STED spot
+
Effective fluor. spot (PSF)
66 nm
1.0
0.5
0.0
–200 0 200
–200 0 200
nm
b
Synaptotagmin
Anti-synaptotagmin antibody
c
d
Confocal
STED
y
x

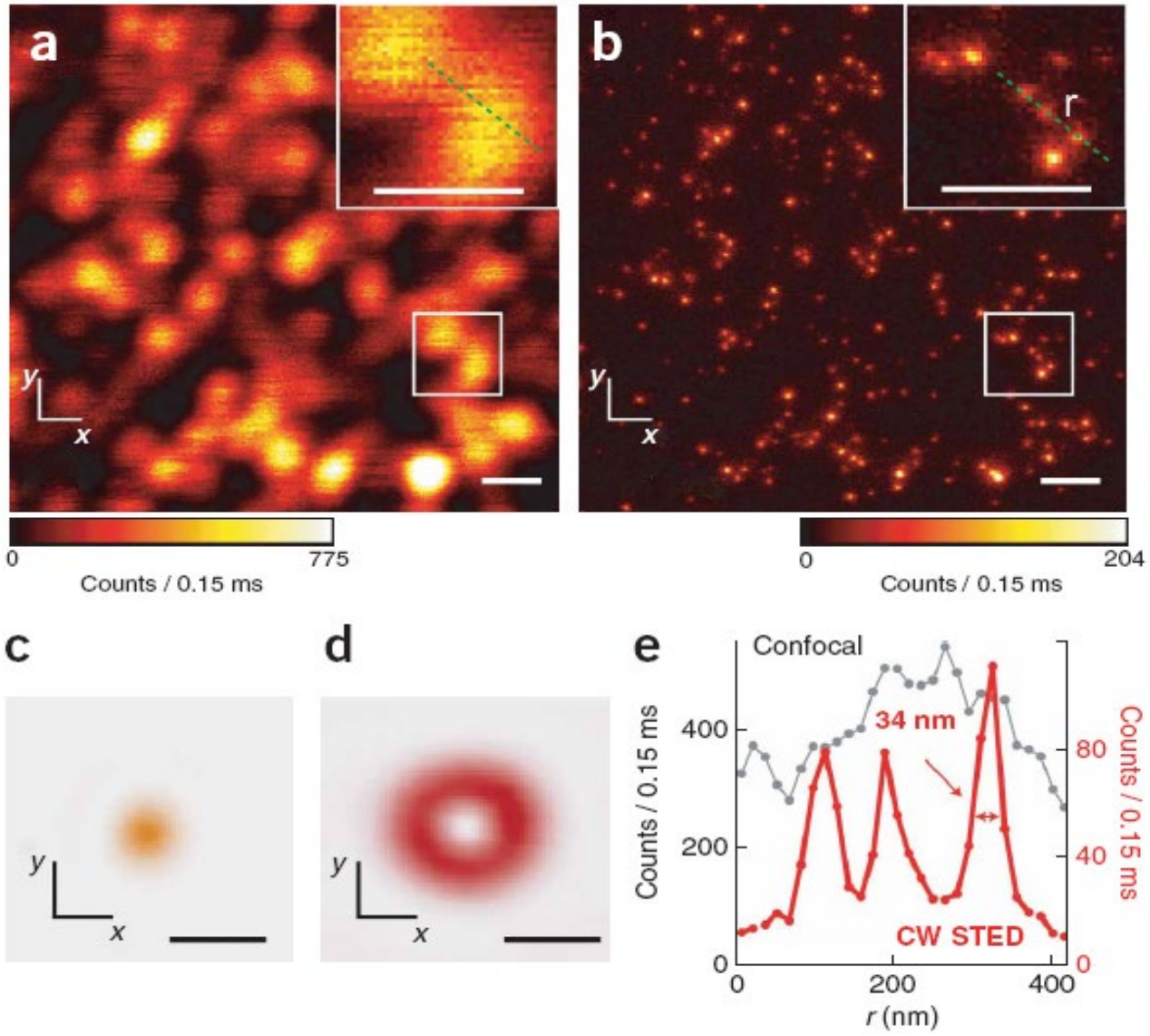
a
b
r
y
x
0
775
Counts / 0.15 ms
0
204
Counts / 0.15 ms
c
d
e
Confocal
34 nm
CW STED
Counts / 0.15 ms
Counts / 0.15 ms
400
200
0
80
40
0
0
200
400
r (nm)

Journal of Microscopy, Vol. 198, Pt 2, May 2000, pp. 82–87.
Received 12 January 2000; accepted 3 March 2000

SHORT COMMUNICATION

Surpassing the lateral resolution limit by a factor of two using structured illumination microscopy

M. G. L. GUSTAFSSON
Department of Biochemistry and Biophysics, University of California San Francisco, San Francisco, California 94143-0448, U.S.A.

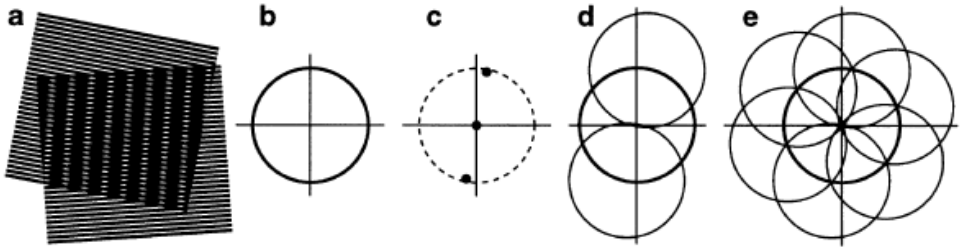

Fig. 1. Concept of resolution enhancement by structured illumination. (a) If two line patterns are superposed (multiplied), their product will contain moiré fringes (seen here as the apparent vertical stripes in the overlap region). (b) A conventional microscope is limited by diffraction. The set of low-resolution information that it can detect defines a circular 'observable region' of reciprocal space. (c) A sinusoidally striped illumination pattern has only three Fourier components. The possible positions of the two side components are limited by the same circle that defines the observable region (dashed). If the sample is illuminated with such structured light, moiré fringes will appear which represent information that has changed position in reciprocal space. The amounts of that movement correspond to the three Fourier components of the illumination. The observable region will thus contain, in addition to the normal information, moved information that originates in two offset regions (d). From a sequence of such images with different orientation and phase of the pattern, it is possible to recover information from an area twice the size of the normally observable region, corresponding to twice the normal resolution (e).

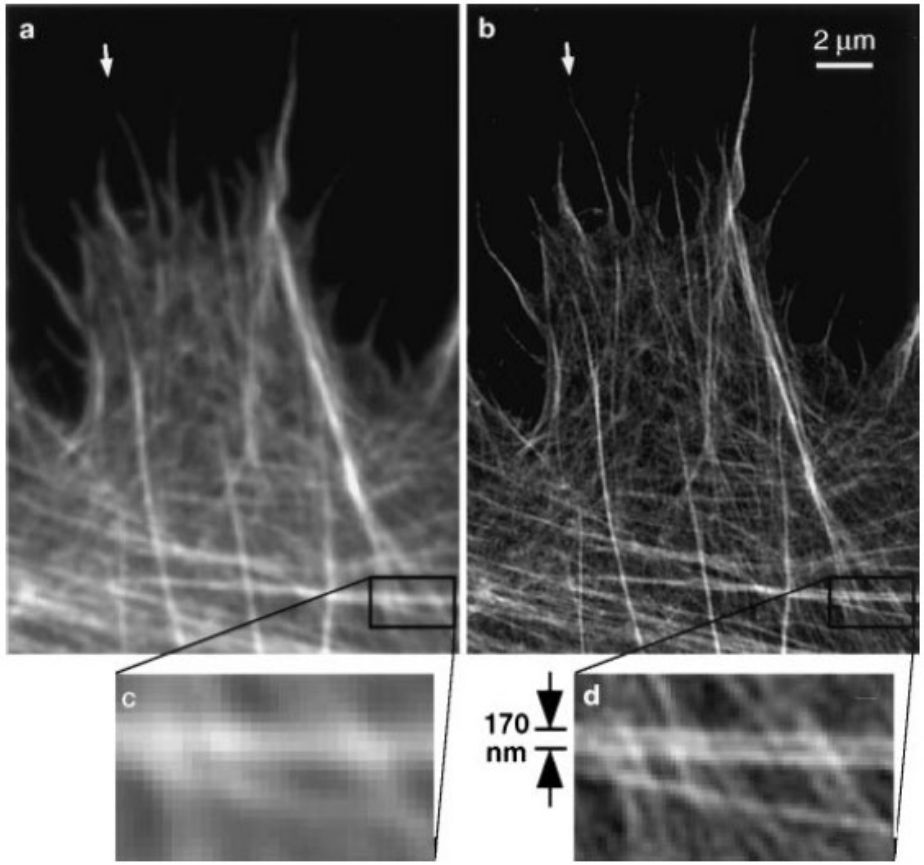

Fig. 4. The actin cytoskeleton at the edge of a HeLa cell, as imaged by (a, c) conventional and (b, d) structured illumination microscopy. (c, d) Enlargements of the boxed areas in (a) and (b), respectively. Fibres separated by less than the resolution limit of the conventional microscope are well resolved using structured illumination (d). The apparent widths (FWHM) of the finest protruding fibres [small arrows in (a, b)] are lowered to 110–120 nm in (b), compared to 280–300 nm in (a).

Nonlinear structured-illumination microscopy: Wide-field fluorescence imaging with theoretically unlimited resolution

PNAS | September 13, 2005 | vol. 102 | no. 37 | 13081–13086

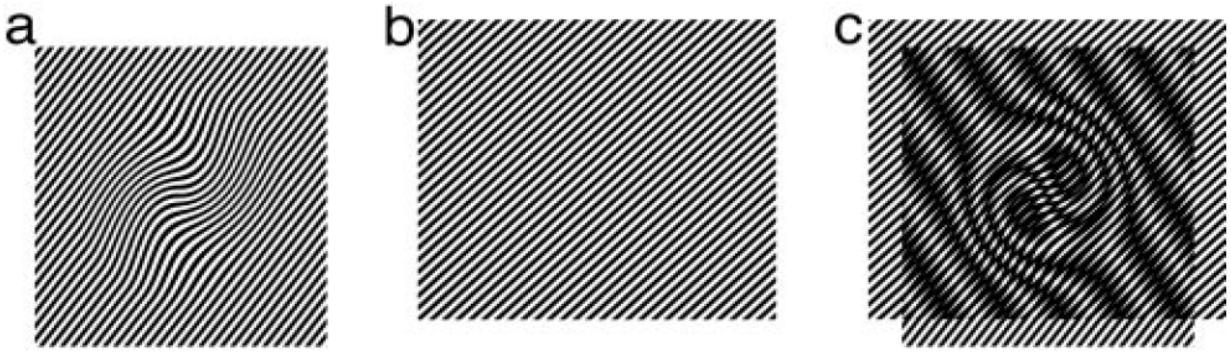

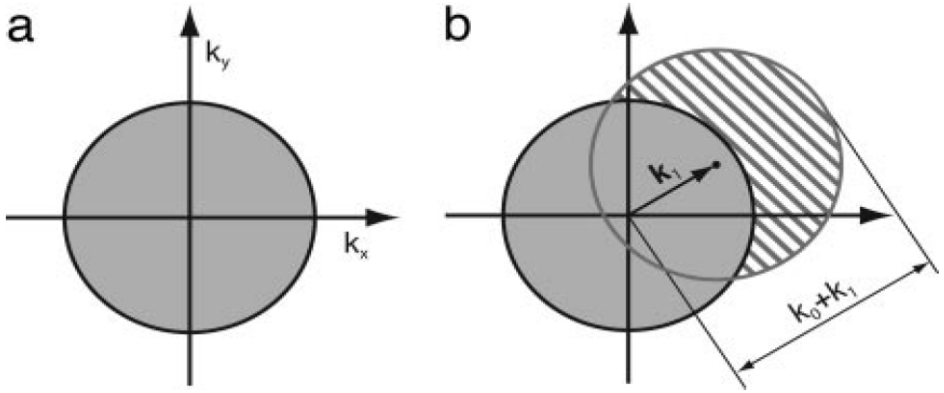

Fig. 2. Structured-illumination concept. (*a*) The set of sample spatial frequencies that can be observed by the conventional microscope defines a circular observable region of radius k_0 in frequency space. (*b*) If the excitation light contains a spatial frequency k_1, a new set of information becomes visible in the form of moiré fringes (hatched circle). This region has the same shape as the normal observable region but is centered at k_1. The maximum spatial frequency that can be detected (in this direction) is $k_0 + k_1$.

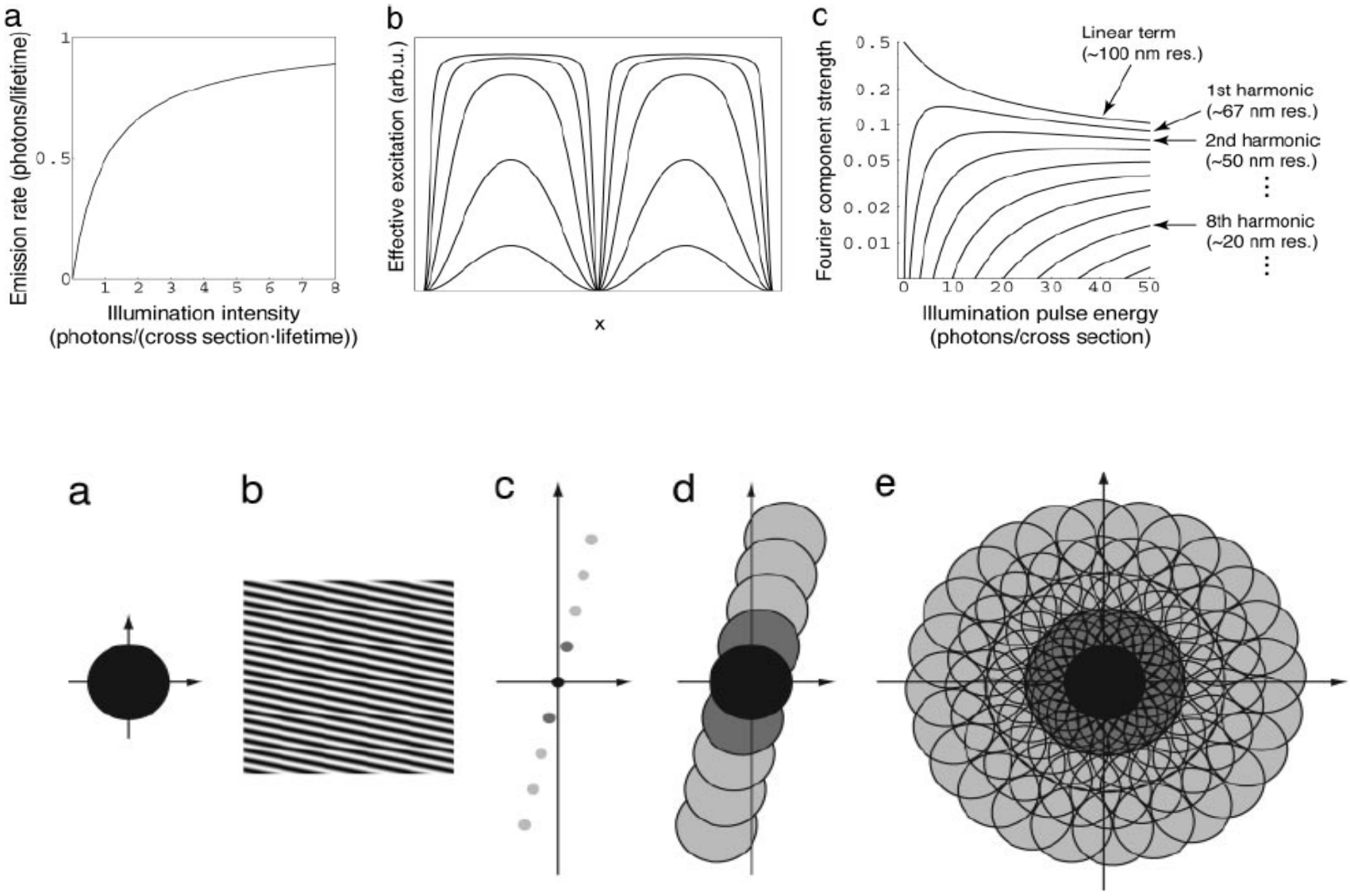
a
Emission rate (photons/lifetime)
1
0.5
0
1 2 3 4 5 6 7 8
Illumination intensity
(photons/(cross section·lifetime))
b
Effective excitation (arb.u.)
x
c
Fourier component strength
0.5
0.2
0.1
0.05
0.02
0.01
0 10 20 30 40 50
Illumination pulse energy
(photons/cross section)
Linear term
(~100 nm res.)
1st harmonic
(~67 nm res.)
2nd harmonic
(~50 nm res.)
8th harmonic
(~20 nm res.)
a
b
c
d
e

Subdiffraction Multicolor Imaging of the Nuclear Periphery with 3D Structured Illumination Microscopy

6 JUNE 2008 VOL 320 SCIENCE

Lothar Schermelleh,[1]* Peter M. Carlton,[2]* Sebastian Haase,[2,4] Lin Shao,[2] Lukman Winoto,[2] Peter Kner,[2] Brian Burke,[3] M. Cristina Cardoso,[4] David A. Agard,[2] Mats G. L. Gustafsson,[5] Heinrich Leonhardt,[1]*† John W. Sedat[2]*†

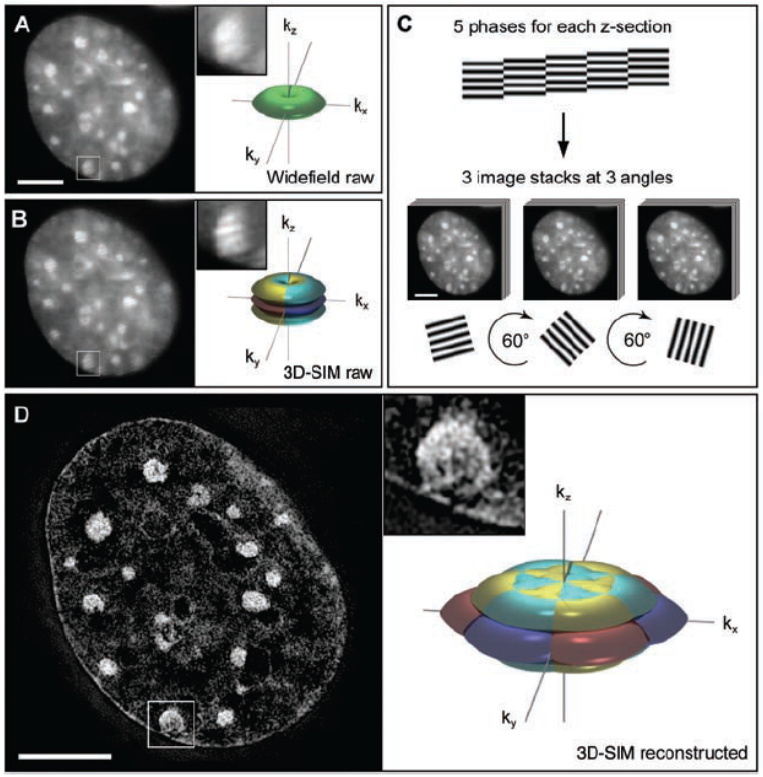

Fig. 1. Subdiffraction resolution imaging with 3D-SIM. (**A** and **B**) Cross section through a DAPI-stained C2C12 cell nucleus acquired with conventional wide-field illumination (A) and with structured illumination (B), showing the striped interference pattern (inset). The renderings to the right illustrate the respective support of detection in frequency space. The axes k_x, k_y, and k_z indicate spatial frequencies along the *x*, *y*, and *z* directions. The surfaces of the renderings represent the corresponding resolution limit. The depression of the frequency support ("missing cone") in *z* direction in (A) indicates the restriction in axial resolution of conventional wide-field microscopy. With 3D-SIM, the axial support is extended but remains within the resolution limit. (**C**) Five phases of the sine wave pattern are recorded at each *z* position, allowing the shifted components to be separated and returned to their proper location in frequency space. Three image stacks are recorded with the diffraction grating sequentially rotated into three positions 60° apart, resulting in nearly rotationally symmetric support over a larger region of frequency space. (**D**) The same cross section of the reconstructed 3D-SIM image shows enhanced image details compared with the original image (insets). The increase in resolution is shown in frequency space on the right, with the coverage extending two times farther from the origin. Scale bars indicate 5 μm.

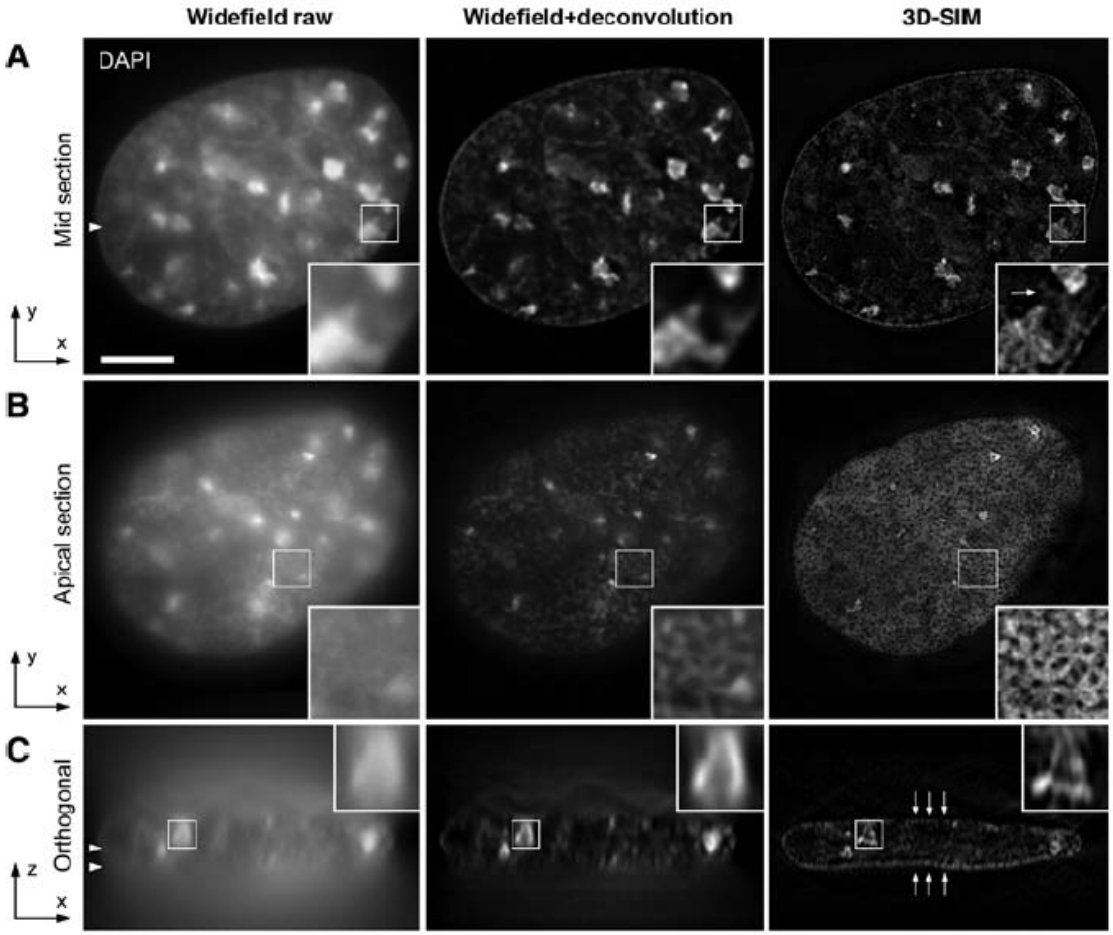
Widefield raw
Widefield+deconvolution
3D-SIM
A
DAPI
Mid section
y
x
B
Apical section
y
x
C
Orthogonal
z
x

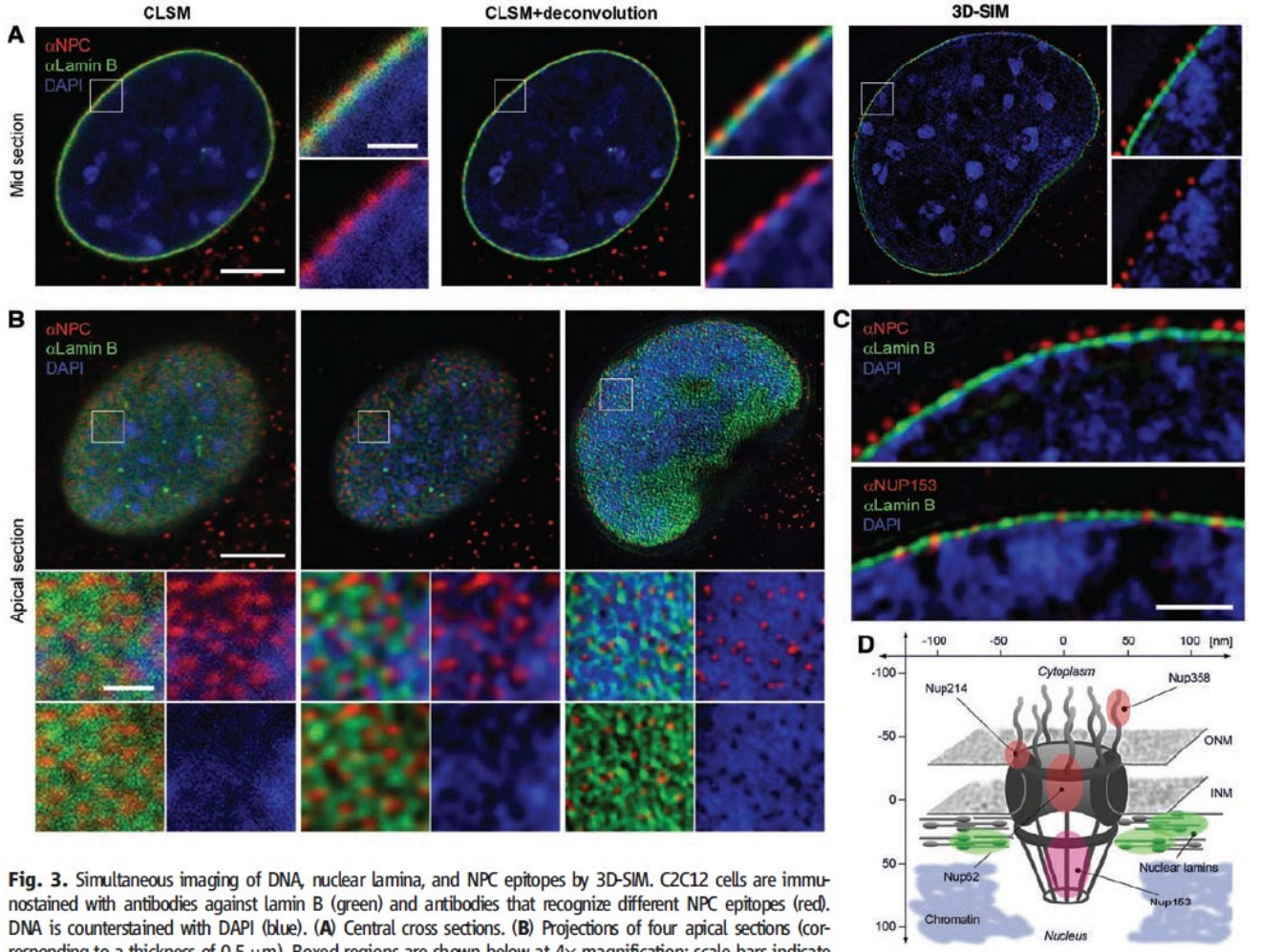

Fig. 3. Simultaneous imaging of DNA, nuclear lamina, and NPC epitopes by 3D-SIM. C2C12 cells are immunostained with antibodies against lamin B (green) and antibodies that recognize different NPC epitopes (red). DNA is counterstained with DAPI (blue). (**A**) Central cross sections. (**B**) Projections of four apical sections (corresponding to a thickness of 0.5 μm). Boxed regions are shown below at 4× magnification; scale bars indicate 5 μm and 1 μm, respectively. (A) CLSM and deconvolution still show partially overlapping signals. In contrast, with 3D-SIM the spatial separation of NPC, lamina, and chromatin and chromatin-free channels underneath nuclear pores are clearly visible. (B) Top view on the nuclear envelope. Whereas CLSM fails to resolve close nuclear pores, 3D-SIM shows clearly separated NPC signals at voids of peripheral chromatin and surrounded by an irregular network of nuclear lamina. (**C**) Mid sections comparing stainings with an antibody that mainly reacts with Nup214, Nup358, and Nup62 (αNPC) and one specifically recognizing Nup153 (αNup153). The αNPC signal is above the lamina (140 ± 8 nm), whereas the αNup153 pore signal is at the same level as the lamina (−15 ± 20 nm). Scale bars 1 μm. (**D**) Schematic outline of the NPC, showing the relative position of Nup proteins and surrounding structures. ONM, outer nuclear membrane; INM, inner nuclear membrane.

Super-resolution video microscopy of live cells by structured illumination

Peter Kner[1,2,7,8], Bryant B Chhun[1,8], Eric R Griffis[3,4], Lukman Winoto[5] & Mats G L Gustafsson[5,6]

NATURE METHODS | VOL.6 NO.5 | MAY 2009 | 339

Structured-illumination microscopy can double the resolution of the widefield fluorescence microscope but has previously been too slow for dynamic live imaging. Here we demonstrate a high-speed structured-illumination microscope that is capable of 100-nm resolution at frame rates up to 11 Hz for several hundred time points. We demonstrate the microscope by video imaging of tubulin and kinesin dynamics in living *Drosophila melanogaster* S2 cells in the total internal reflection mode.

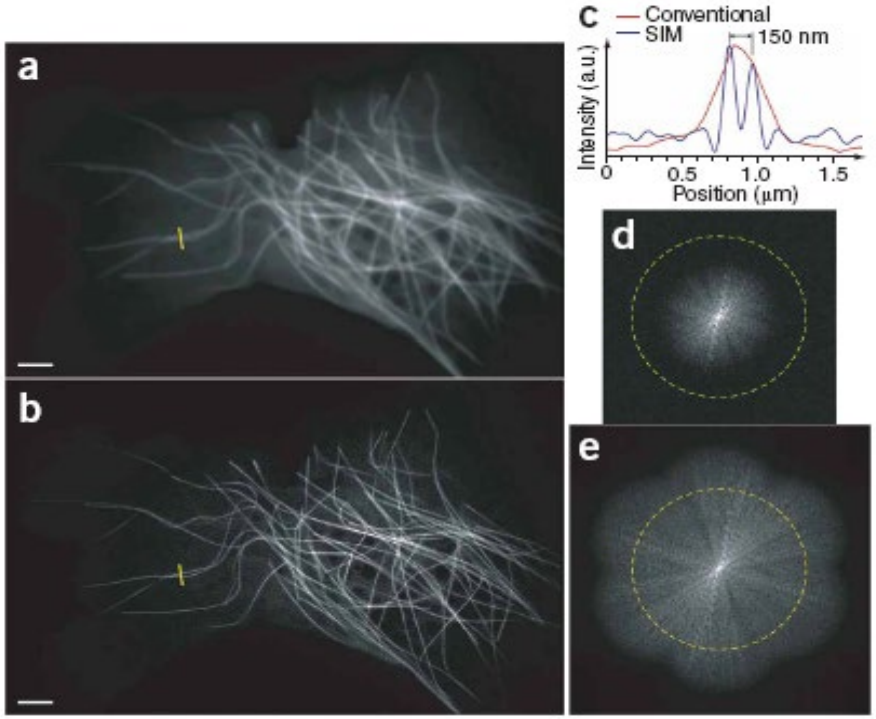

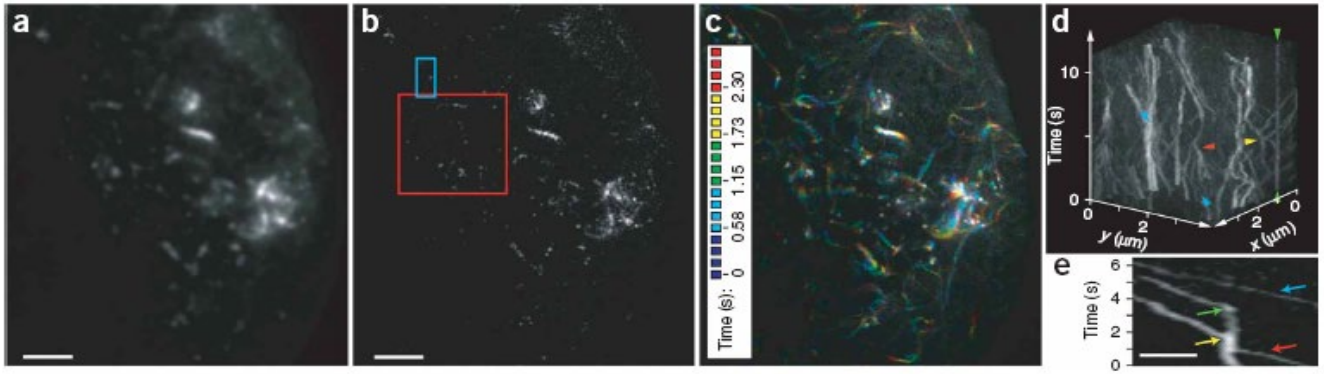

Light sheet fluorescence microscopy

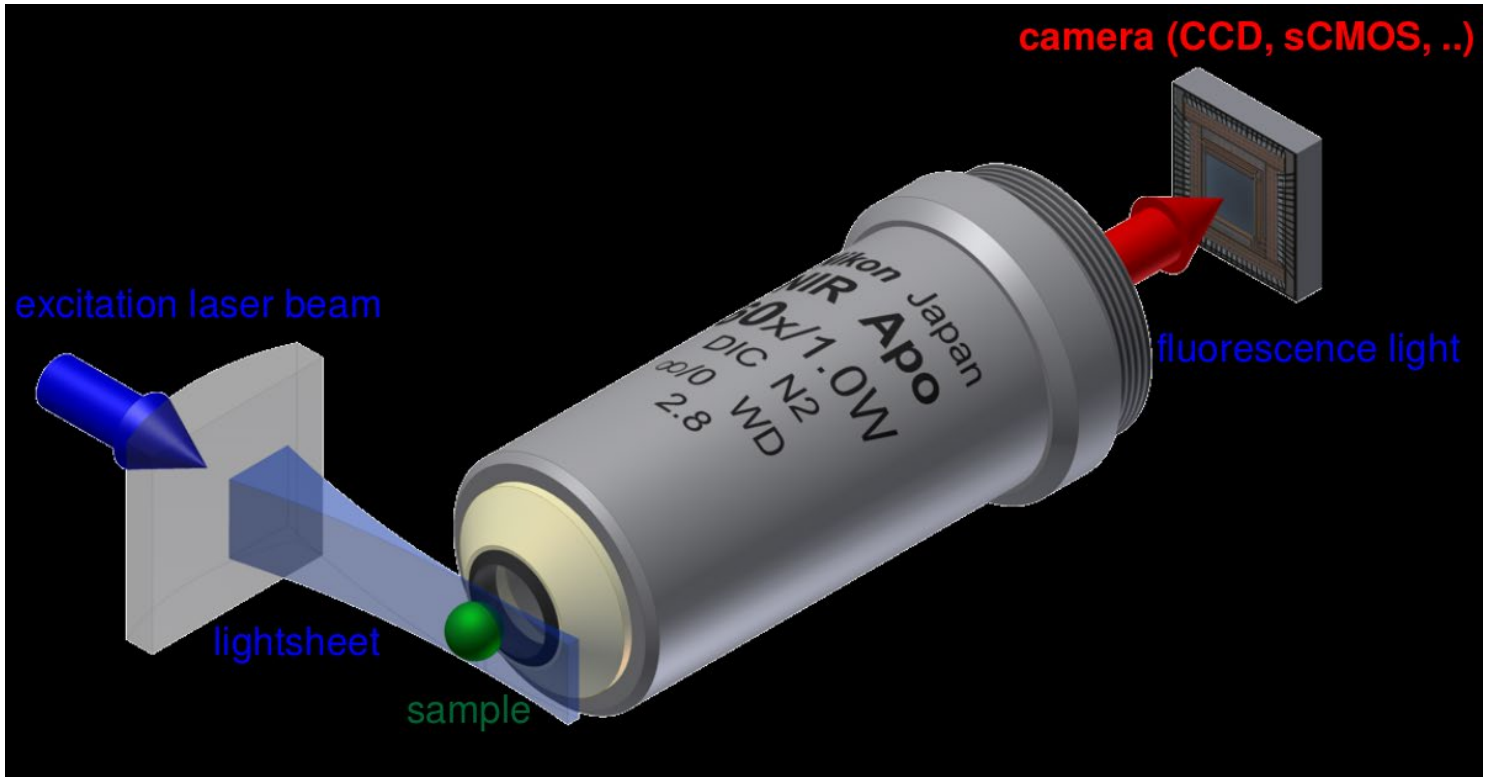

Rapid three-dimensional isotropic imaging of living cells using Bessel beam plane illumination

Thomas A Planchon[1,6], Liang Gao[1,6], Daniel E Milkie[2], Michael W Davidson[3], James A Galbraith[4], Catherine G Galbraith[5] & Eric Betzig[1]

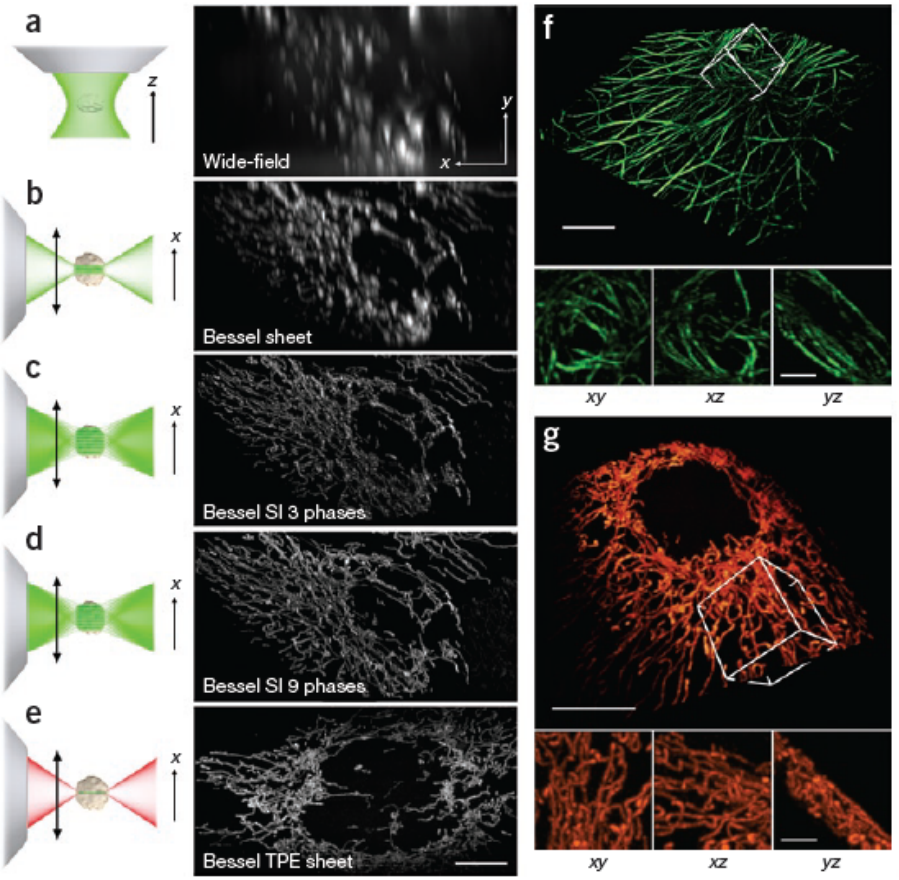

Figure 2 | Modes of Bessel beam plane illumination microscopy. (**a**) Wide-field illumination geometry (left) and maximum-intensity projection (MIP) in the *x*–*z* plane (right; *z*, detection axis) from a 3D image stack of a fixed human osteosarcoma cell (U2OS) transfected with plasmids encoding mEmerald fused to human pyruvate dehydrogenase alpha 1 (PDHA1). (**b**) Bessel sheet mode geometry (left), showing fluorescence excitation from Bessel side lobes (light green) as well as the central peak (dark green), and *x*–*z* plane MIP (right) from same cell as in **a**. (**c**,**d**) Bessel SI mode geometry, showing periodic Bessel beam excitation pattern (left) and *x*–*z* plane MIPs with single-harmonic (**c**) and multiharmonic (**d**) excitation (right). (**e**) Two-photon excitation (TPE) Bessel sheet mode geometry (left), showing infrared excitation (red) of fluorescence in the central peak (green), with negligible fluorescence in side lobes and *x*–*z* plane MIP from a cell (right) similar to those in **a**–**d**. (**f**) Volume rendering in the multiharmonic SI mode (9 phases, 2.4 μm period) of mEmerald-tagged microtubule associated protein 4 (MAP4) in a live U2OS cell. (**g**) Volume rendering in the TPE sheet mode of mEmerald-labeled mitochondria in a live pig kidney epithelial cell (LLC-PK1 cell line). Insets in **f** and **g** show MIPs along orthogonal axes of the cubical volumes shown. Scale bars, 10 μm except 3 μm in insets.

Figure 4 | Three-dimensional isotropic imaging of live-cell dynamics. (**a**) Images of ER in a live U2OS cell, visualized in the Bessel multiharmonic 9 phase SI mode, over 45 image volumes: representation of a subset of the 321 image planes (brown lines) comprising each volume (top); images from three indicated image planes; and image volumes after 10 and 30 min of observation. (**b**) Filopodia at the apical surface of a live HeLa cell, visualized in the Bessel TPE sheet mode over three consecutive image volumes from 100 such volumes taken at 6-s intervals. Filaments that wave (magenta and yellow arrowheads), extend outward (cyan arrowhead) or retract inward (green arrowhead) are marked. (**c**) African green monkey kidney cell (COS-7) transfected with plasmids encoding mEmerald–c-Src, demonstrating retrograde flow of membrane ruffles (left) and vacuole formation by macropinocytosis (right; arrowheads) in an exemplary plane in a translucent cell view (top). All data were extracted from 73 image stacks taken at 12-s intervals. Scale bars, 5 μm (**a**,**b**) and 10 μm (**c**).

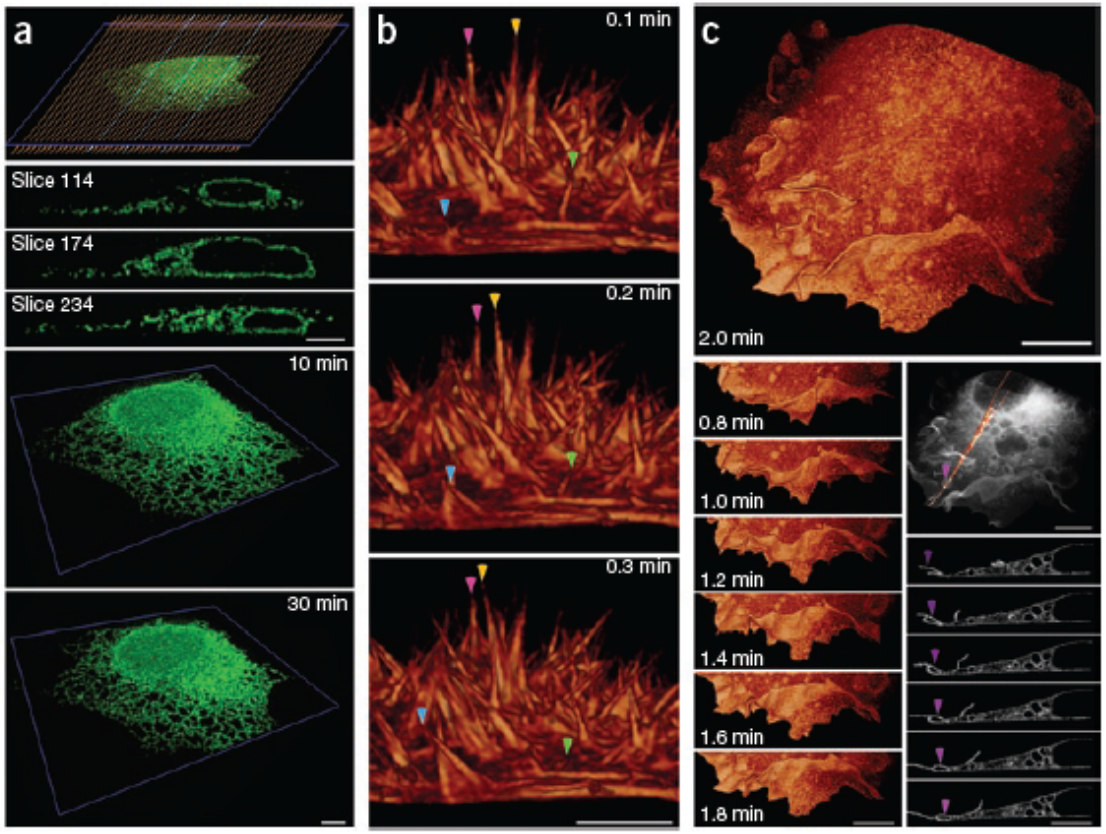

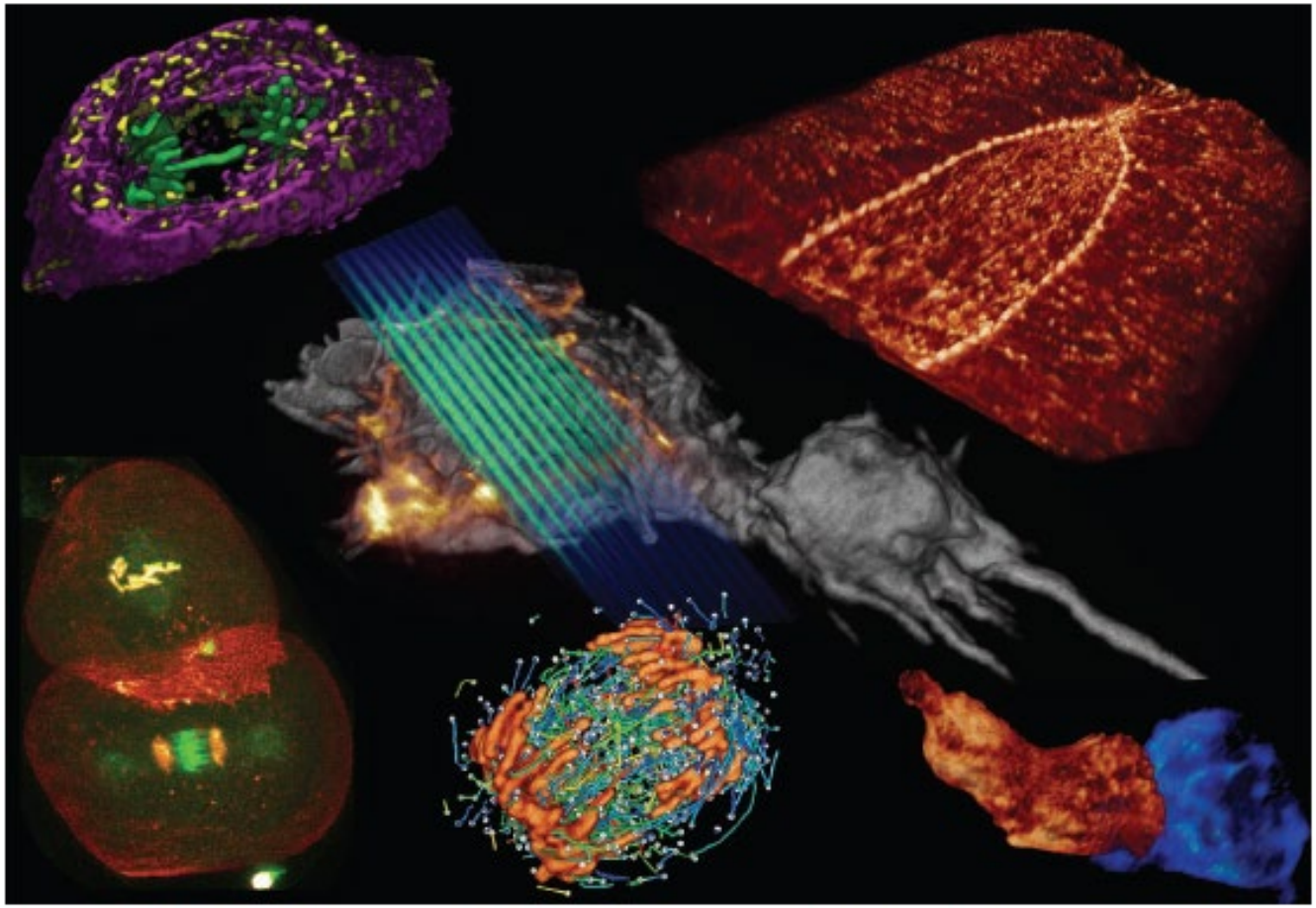

Lattice light-sheet microscopy. An ultrathin structured light sheet (blue-green, center) excites fluorescence (orange) in successive planes as it sweeps through a specimen (gray) to generate a 3D image. The speed, noninvasiveness, and high spatial resolution of this approach make it a promising tool for in vivo 3D imaging of fast dynamic processes in cells and embryos, as shown here in five surrounding examples.

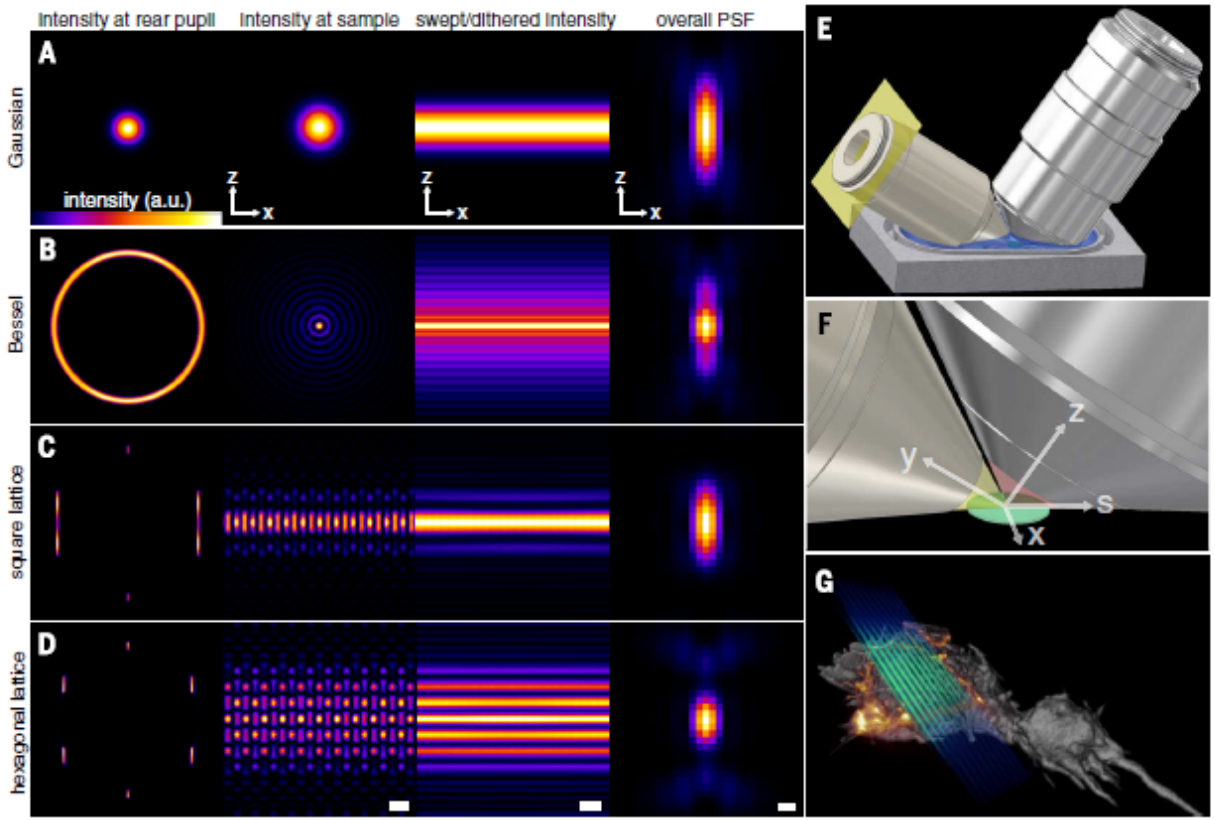

Fig. 1. Methods of light-sheet microscopy. (**A**) The traditional approach, where a Gaussian beam is swept across a plane to create the light sheet. a.u., arbitrary units. (**B**) A Bessel beam of comparable length produces a swept sheet with a much narrower core but flanked by sidebands arising from concentric side lobes of the beam. (**C** and **D**) Bound optical lattices (compare with movie S1) create periodic patterns of high modulation depth across the plane, greatly reducing the peak intensity and, as we have found, the phototoxicity in live cell imaging. The square lattice in (C) optimizes the confinement of the excitation to the central plane, and the hexagonal lattice in (D) optimizes the axial resolution as defined by the overall PSF of the microscope. The columns in (A) to (D) show the intensity pattern at the rear pupil plane of the excitation objective; the cross-sectional intensity of the pattern in the *xz* plane at the focus of the excitation objective (scale bar, 1.0 μm); the cross-sectional intensity of the light sheet created by dithering the focal pattern along the *x* axis (scale bar, 1.0 μm); and the *xz* cross section of the overall PSF of the microscope (scale bar, 200 nm). (**E**) Model showing the core of our microscope, with orthogonal excitation (left) and detection (right) objectives dipped in a media-filled bath (compare with fig. S4). (**F**) Higher magnification view, showing the excitation (yellow) and detection (red) light cones, which meet at a common focus within a specimen that is either mounted or cultured onto a cover glass within the media. The *x*, *y*, and *z* directions are indicated. The *s*-axis defines the direction the specimen moves from image plane to image plane. (**G**) Representation of a lattice light sheet (blue-green) intersecting a cell (gray) to produce fluorescence (orange) in a single plane. The cell is swept through the light sheet to generate a 3D image (compare with movie S2).

Optical Clearing

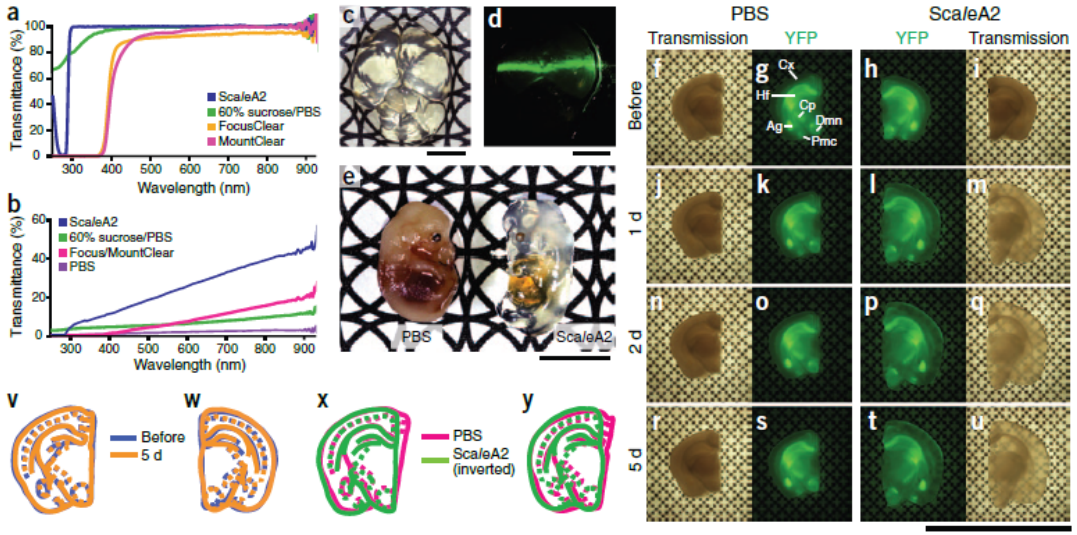

Whole-Brain Imaging with Single-Cell Resolution Using Chemical Cocktails and Computational Analysis

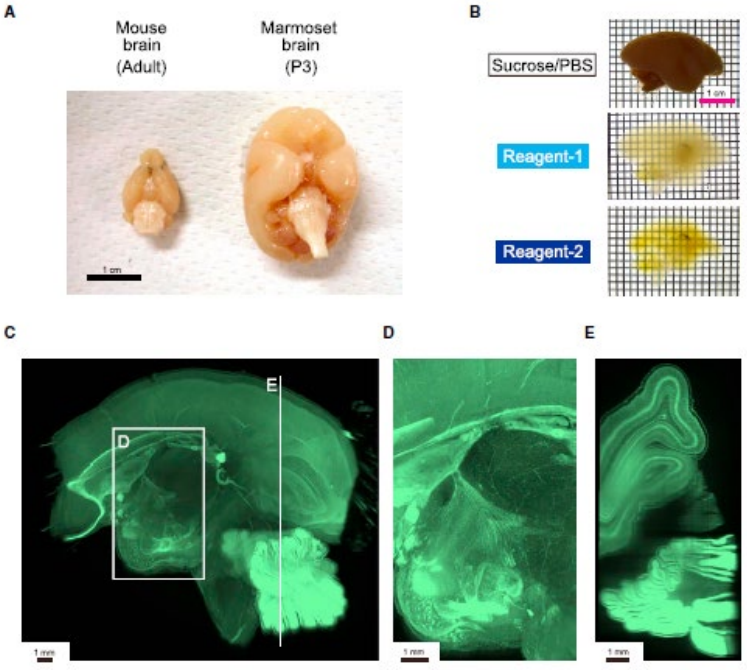

Whole-body and Whole-Organ Clearing and Imaging Techniques with Single-Cell Resolution: Toward Organism-Level Systems Biology in Mammals

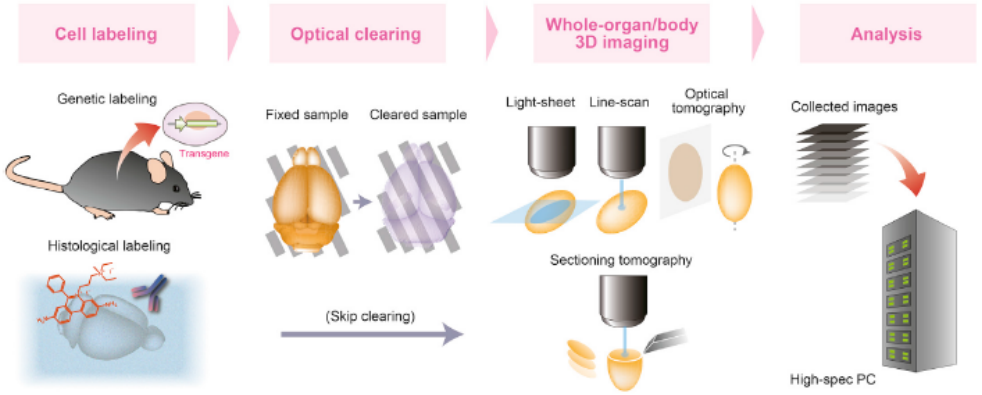

Figure 1. Steps for Organism-Level Systems Biology

Overview of the proposed research scheme, aiming at organism-level systems biology in mammal by comprehensive cell detection and analysis of whole-organ/body. This is achieved by optical tissue clearing and imaging (or alternatively by sectioning tomography without clearing) of properly labeled specimens. Data are analyzed to extract biological information, for which high-spec PC equipment is generally needed.

Whole-Body Imaging with Single-Cell Resolution by Tissue Decolorization

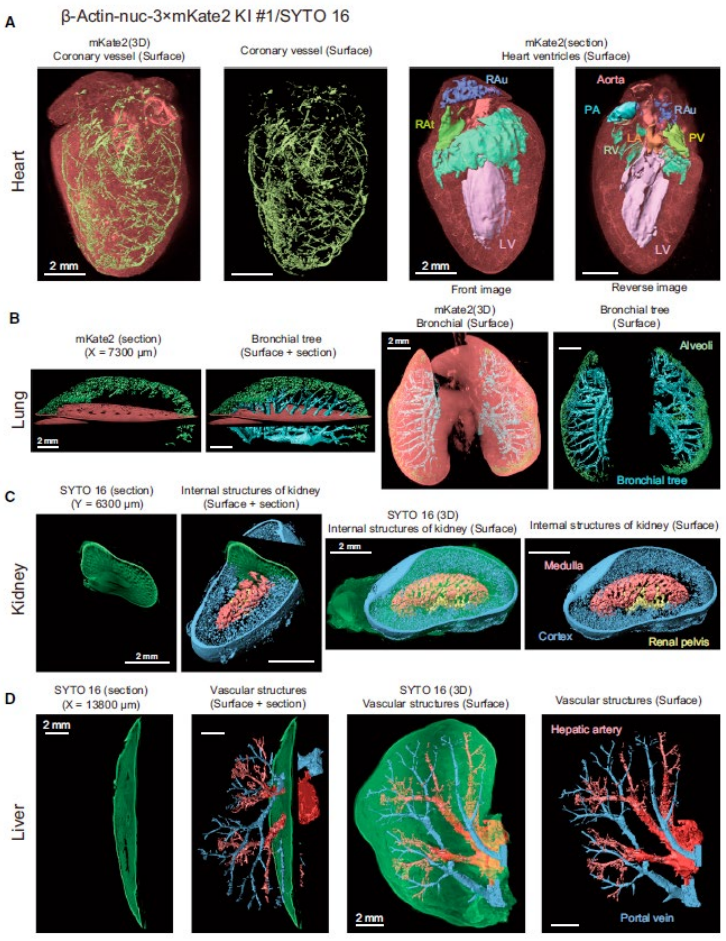

Cell *159*, 911–924, November 6, 2014 ©2014 Elsevier Inc. **911**

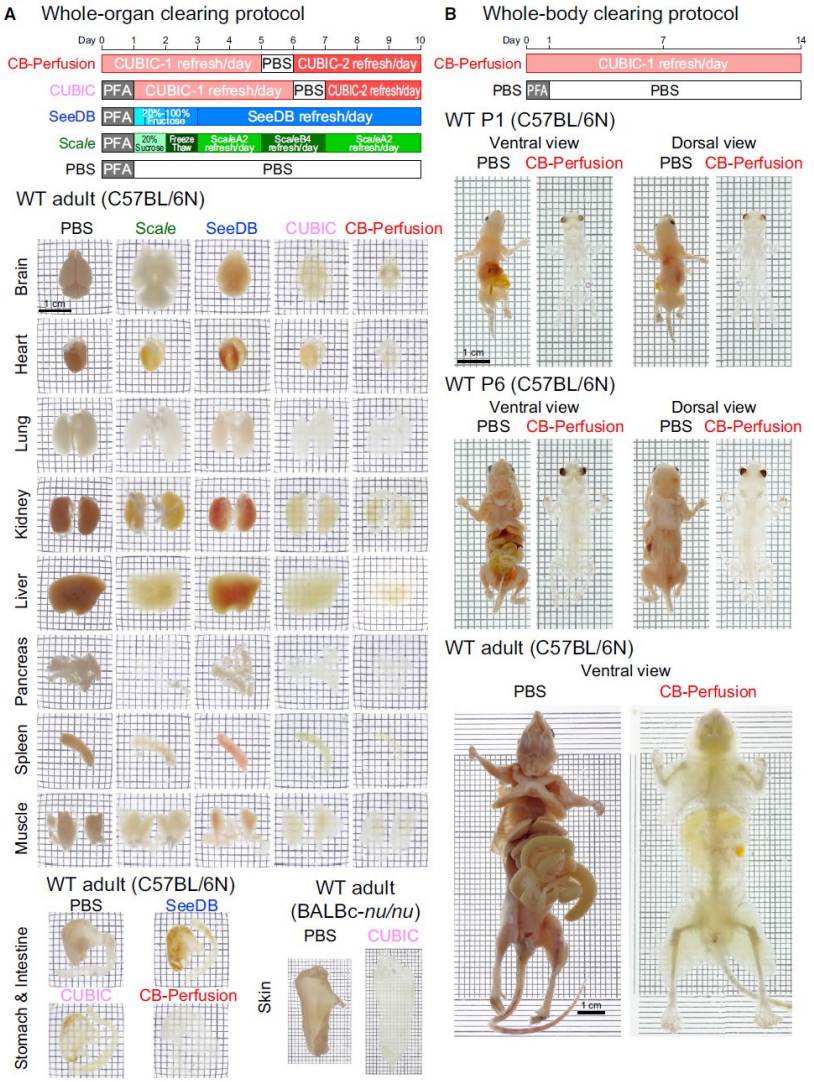

Structural and molecular interrogation of intact biological systems

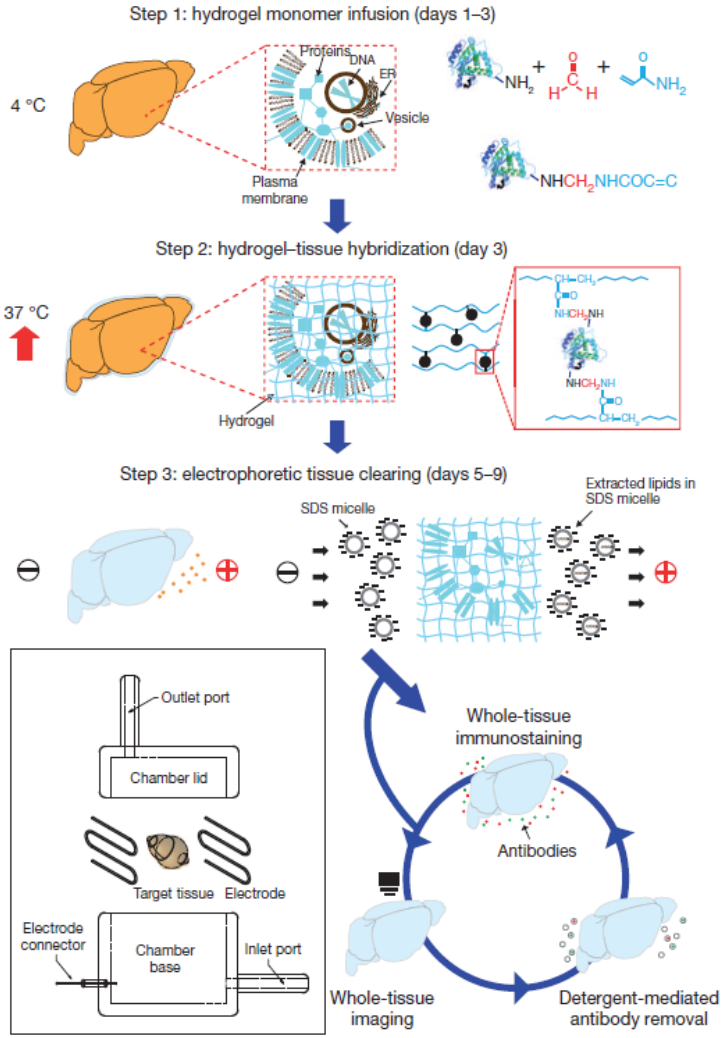

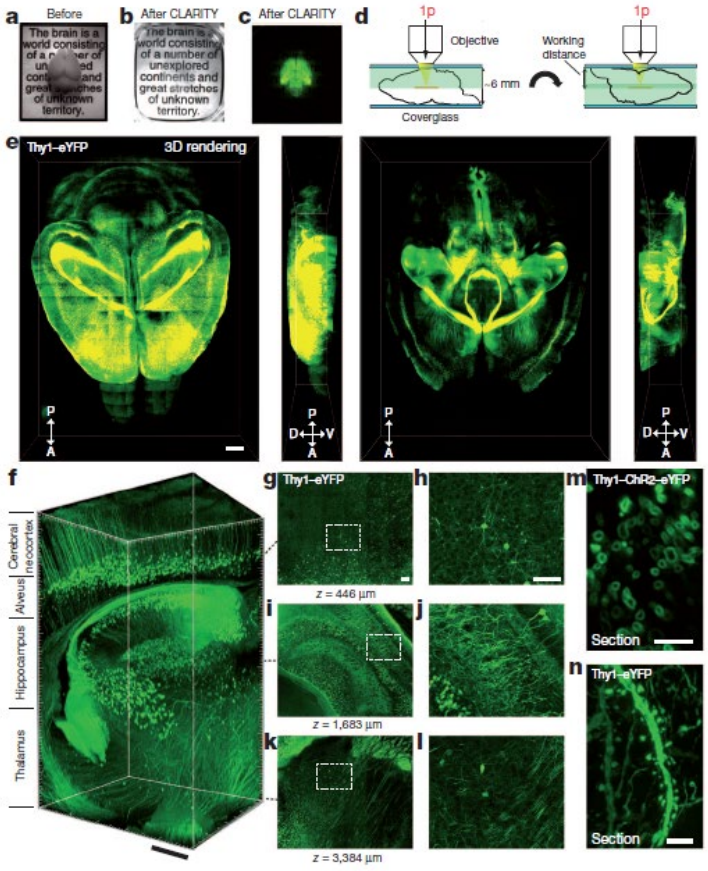

OPTICAL IMAGING

Expansion microscopy

Fei Chen,[1*] Paul W. Tillberg,[2*] Edward S. Boyden[1,3,4,5,6†]

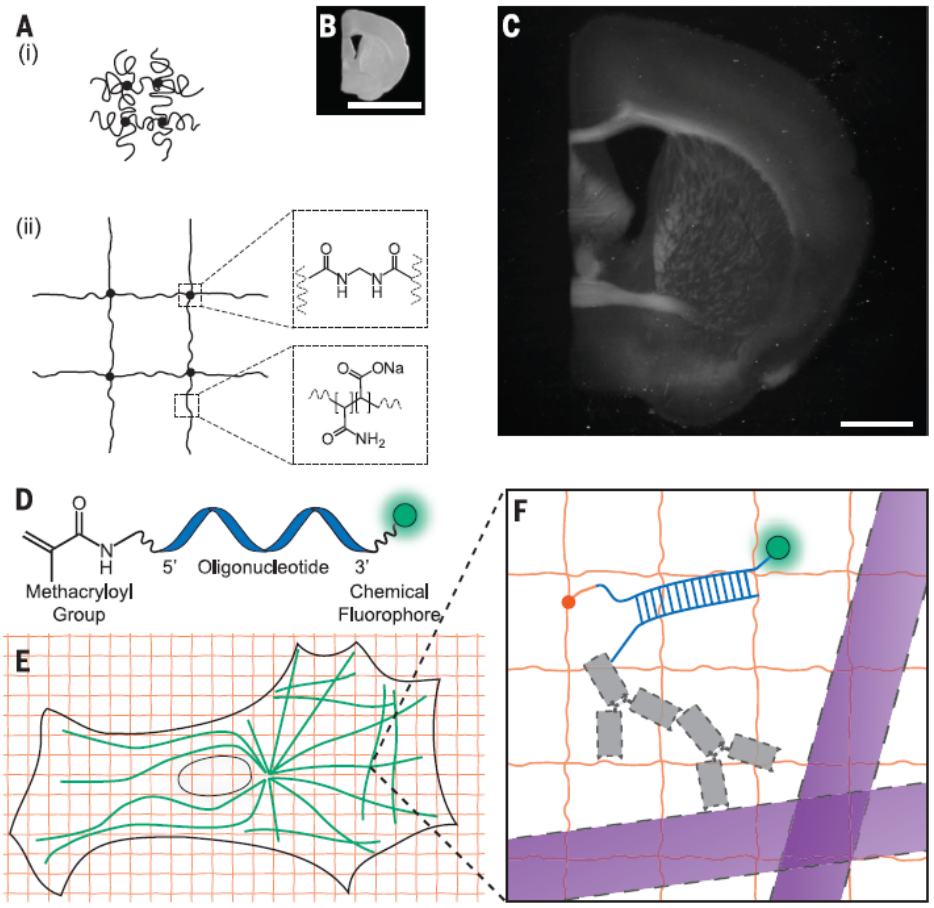

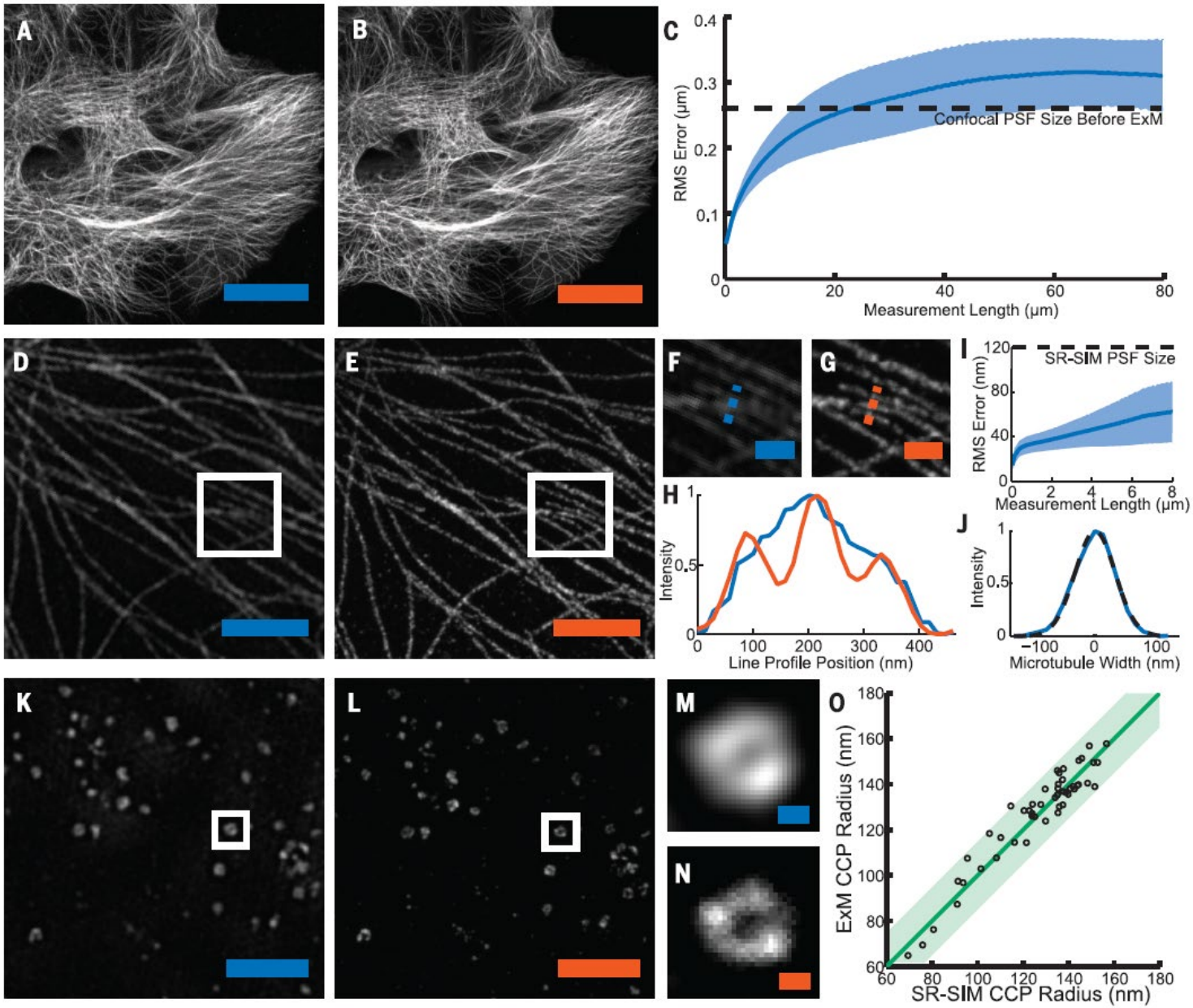
A
B
C
RMS Error (μm)
Measurement Length (μm)
Confocal PSF Size Before ExM
D
E
F
G
H
Intensity
Line Profile Position (nm)
I
SR-SIM PSF Size
RMS Error (nm)
Measurement Length (μm)
J
Intensity
Microtubule Width (nm)
K
L
M
N
O
ExM CCP Radius (nm)
SR-SIM CCP Radius (nm)

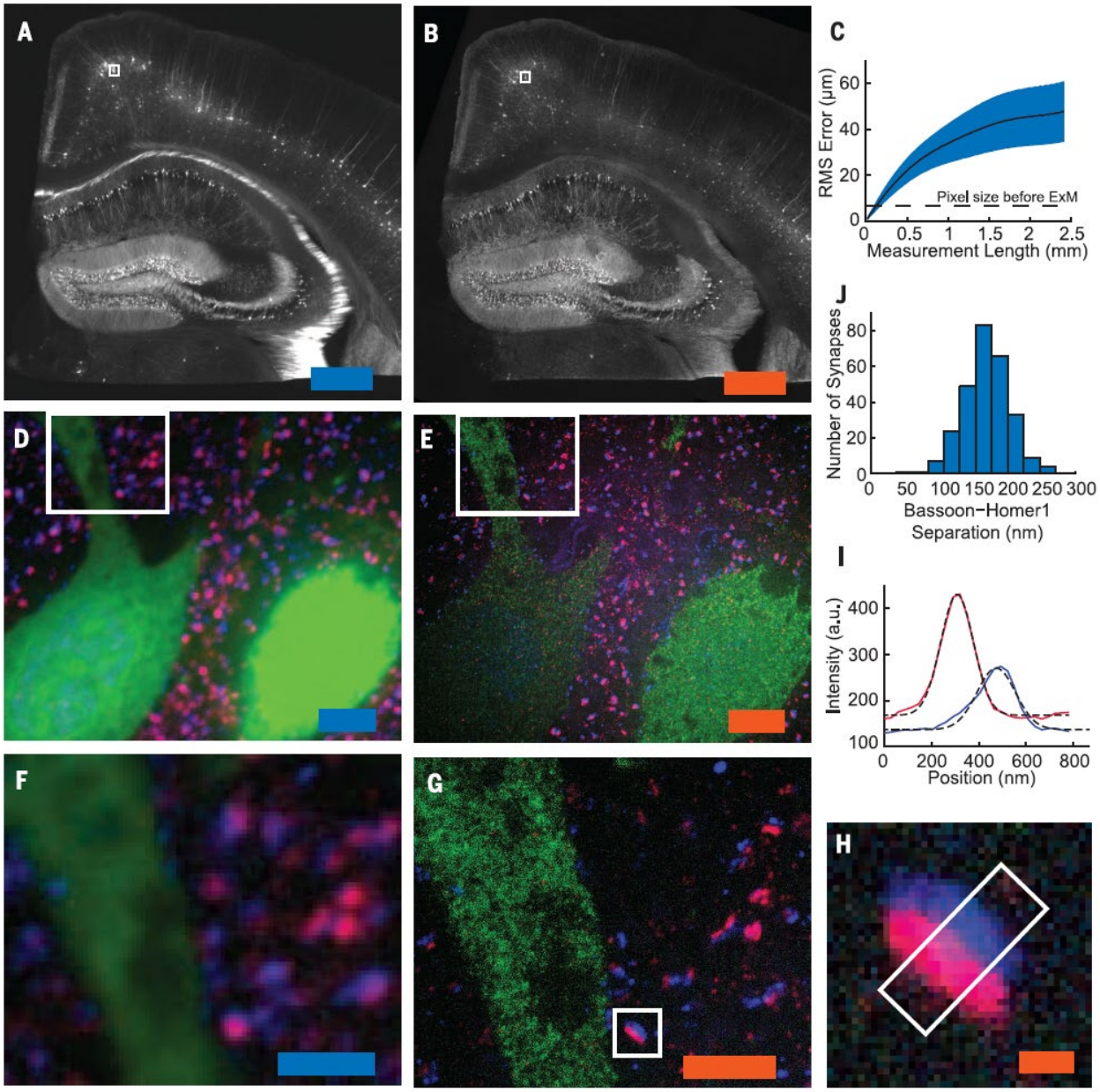
A
B
C
RMS Error (μm)
60
40
20
0
Pixel size before ExM
0
0.5
1
1.5
2
2.5
Measurement Length (mm)
J
Number of Synapses
80
60
40
20
0
0
50
100
150
200
250
300
Bassoon−Homer1
Separation (nm)
D
E
I
Intensity (a.u.)
400
300
200
100
0
200
400
600
800
Position (nm)
F
G
H

RESEARCH ARTICLE SUMMARY

IMAGING TECHNIQUES

Cortical column and whole-brain imaging with molecular contrast and nanoscale resolution

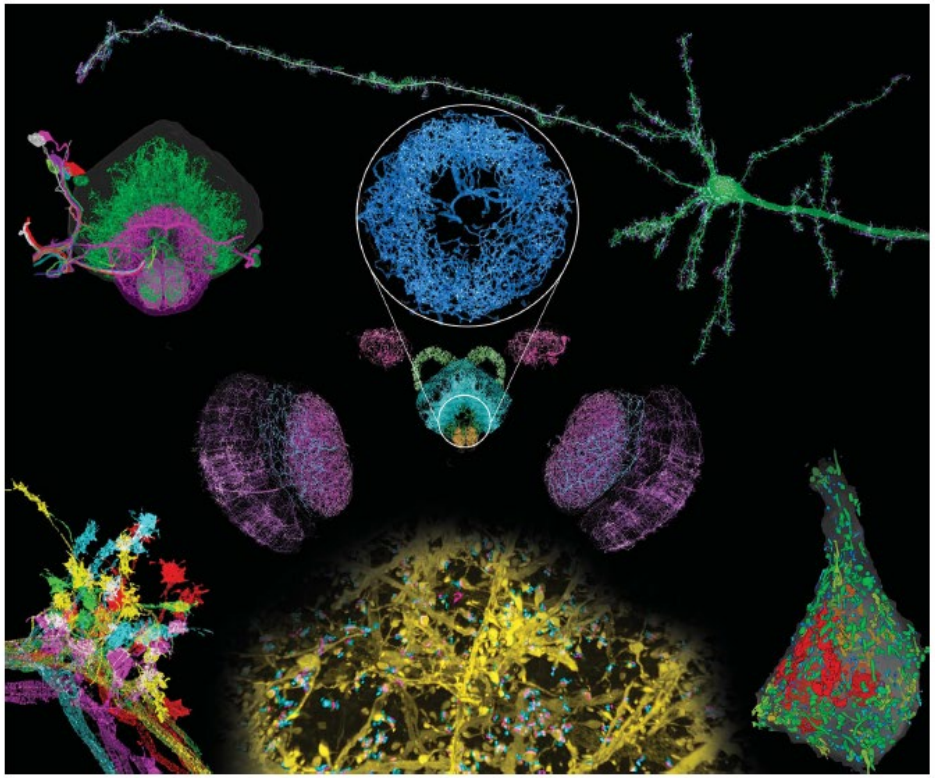

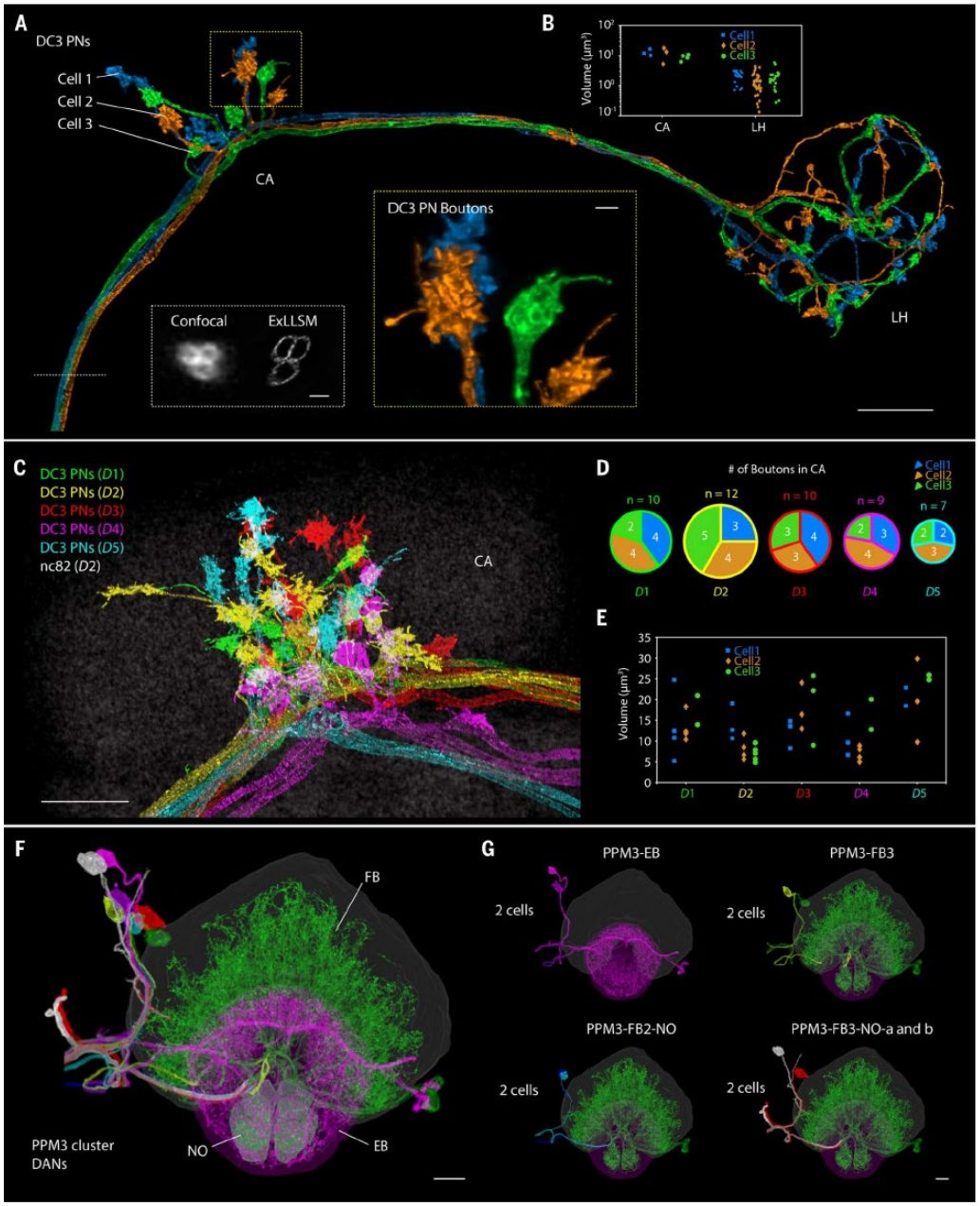
A
DC3 PNs
Cell 1
Cell 2
Cell 3
CA
LH
DC3 PN Boutons
Confocal
ExLLSM
B
Volume (μm³)
Cell1
Cell2
Cell3
CA
LH
C
DC3 PNs (D1)
DC3 PNs (D2)
DC3 PNs (D3)
DC3 PNs (D4)
DC3 PNs (D5)
nc82 (D2)
CA
D
# of Boutons in CA
n = 10
n = 12
n = 10
n = 9
n = 7
D1
D2
D3
D4
D5
E
Volume (μm³)
F
FB
PPM3 cluster DANs
NO
EB
G
PPM3-EB
2 cells
PPM3-FB3
2 cells
PPM3-FB2-NO
2 cells
PPM3-FB3-NO-a and b
2 cells

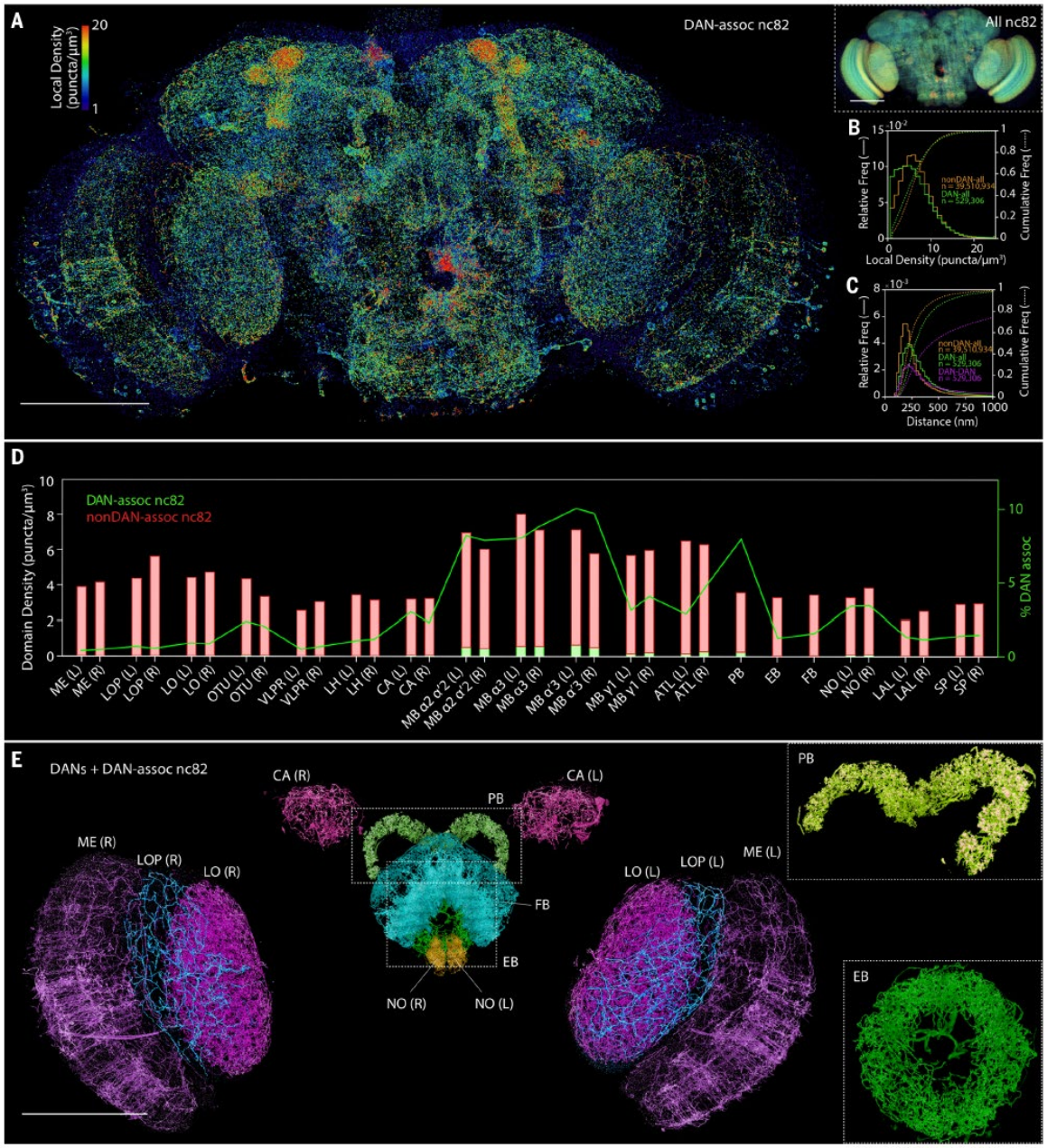
A
Local Density (puncta/µm³)
20
1
DAN-assoc nc82
All nc82
B
Relative Freq (——)
Cumulative Freq (- - -)
Local Density (puncta/µm³)
C
Relative Freq (——)
Cumulative Freq (- - -)
Distance (nm)
D
DAN-assoc nc82
nonDAN-assoc nc82
Domain Density (puncta/µm³)
% DAN assoc
ME (L)
ME (R)
LOP (L)
LOP (R)
LO (L)
LO (R)
OTU (L)
OTU (R)
VLPR (L)
VLPR (R)
LH (L)
LH (R)
CA (L)
CA (R)
MB α2 α'2 (L)
MB α2 α'2 (R)
MB α3 (L)
MB α3 (R)
MB α'3 (L)
MB α'3 (R)
MB γ1 (L)
MB γ1 (R)
ATL (L)
ATL (R)
PB
EB
FB
NO (L)
NO (R)
LAL (L)
LAL (R)
SP (L)
SP (R)
E
DANs + DAN-assoc nc82
CA (R)
CA (L)
PB
ME (R)
LOP (R)
LO (R)
FB
EB
NO (R)
NO (L)
LO (L)
LOP (L)
ME (L)
PB
EB

Spatial Biology

Spatial Biology is an interdisciplinary research field that focuses on the study of biological systems in relation to their spatial organization and distribution at various scales, ranging from molecular to cellular, tissue, and organism levels. This field combines advanced imaging techniques, computational methods, and molecular biology approaches to investigate the spatial arrangement of biomolecules, cells, and tissues, and how these spatial relationships influence biological functions, processes, and interactions.

GPT4-4

Directions of Spatial Biology

Advanced Imaging Techniques: Techniques such as super-resolution microscopy, cryo-electron microscopy, and light-sheet microscopy will be further refined and expanded, allowing for greater resolution, sensitivity, and speed in imaging cellular structures and molecular interactions.

Integration of Omics Data: Combining spatial biology with other omics data types, such as genomics, transcriptomics, proteomics, and metabolomics, will enable a more comprehensive understanding of the spatial organization of biological systems and their functional consequences.

Spatial Analysis and Computational Methods : advanced computational methods and tools for data analysis, visualization, and interpretation. Machine learning and artificial intelligence algorithms will play a crucial role in processing and understanding these complex data sets.

Single-Cell Spatial Analysis

Organoid and 3D Culture Systems

In Vivo Imaging and Therapeutics:

Applications of Spatial Biology

Drug Discovery: Spatial biology can be used to identify drug targets and understand their spatial organization, expression, and function within cells and tissues. This can facilitate the development of drugs that target specific cellular components, pathways, or interactions, leading to more effective and targeted therapies.

Diagnostics: Spatial biology can help identify disease-specific spatial patterns or biomarkers, which can be used for the early detection, diagnosis, and monitoring of diseases such as cancer, neurological disorders, and infectious diseases.

Personalized Medicine: Understanding the spatial organization of cells and tissues in individual patients can lead to the development of personalized treatment strategies tailored to their unique biological context. Spatial biology can inform decisions regarding drug selection, dosage, and administration, as well as the identification of patient subpopulations that may respond differently to specific therapies.

Tissue Engineering and Regenerative Medicine: Spatial biology provides insights into tissue organization, development, and repair, which can be applied to tissue engineering and regenerative medicine. This information can guide the design of artificial tissues and organs, as well as the development of strategies to promote tissue regeneration and repair following injury or disease.

Available online at www.sciencedirect.com

ScienceDirect

Current Opinion in Biotechnology

Spatial transcriptomics: paving the way for tissue-level systems biology

Andreas E Moor and Shalev Itzkovitz

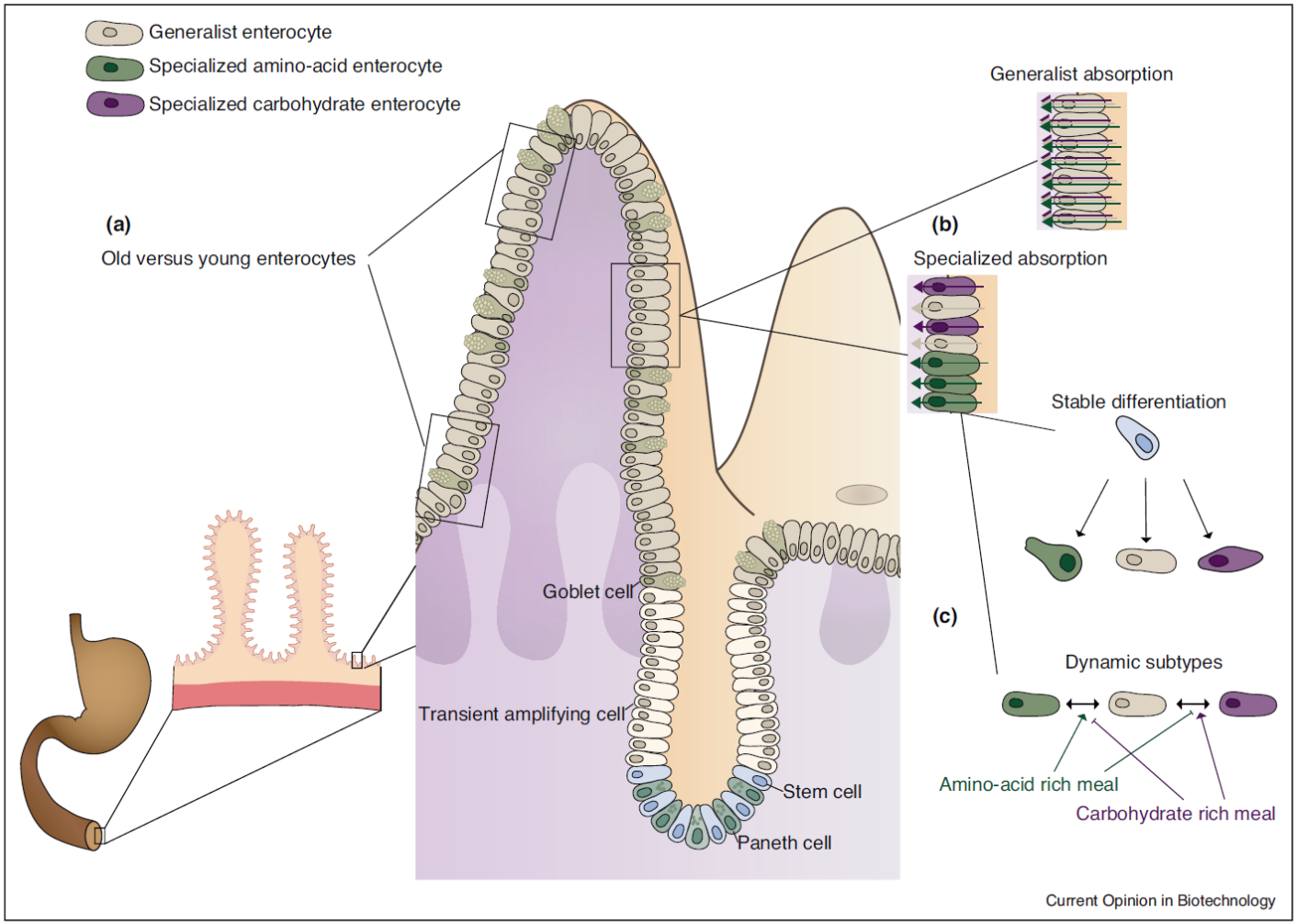

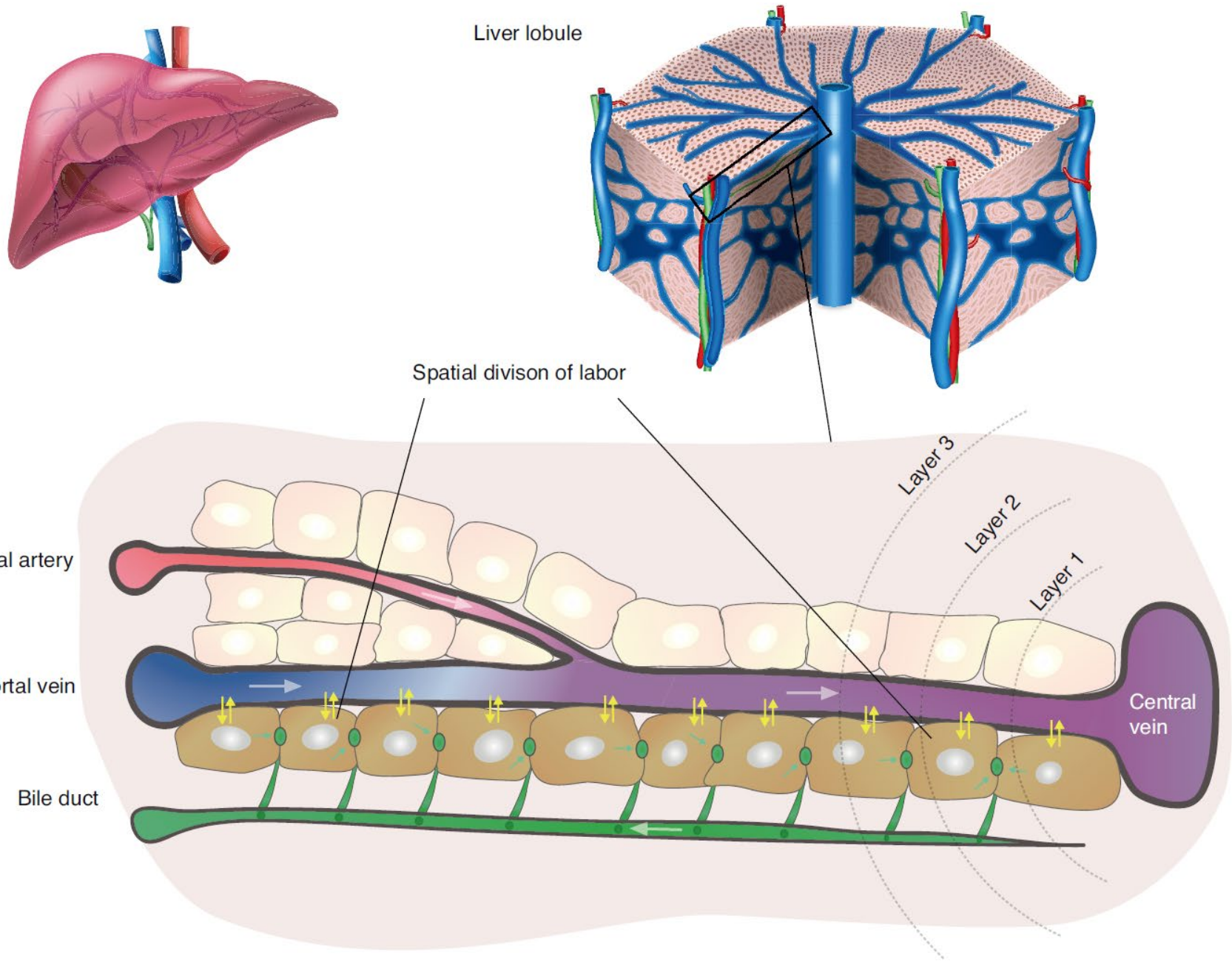
Liver lobule
Spatial divison of labor
Layer 3
Layer 2
Layer 1
Portal artery
Portal vein
Bile duct
Central vein
Current Opinion in Biotechnology

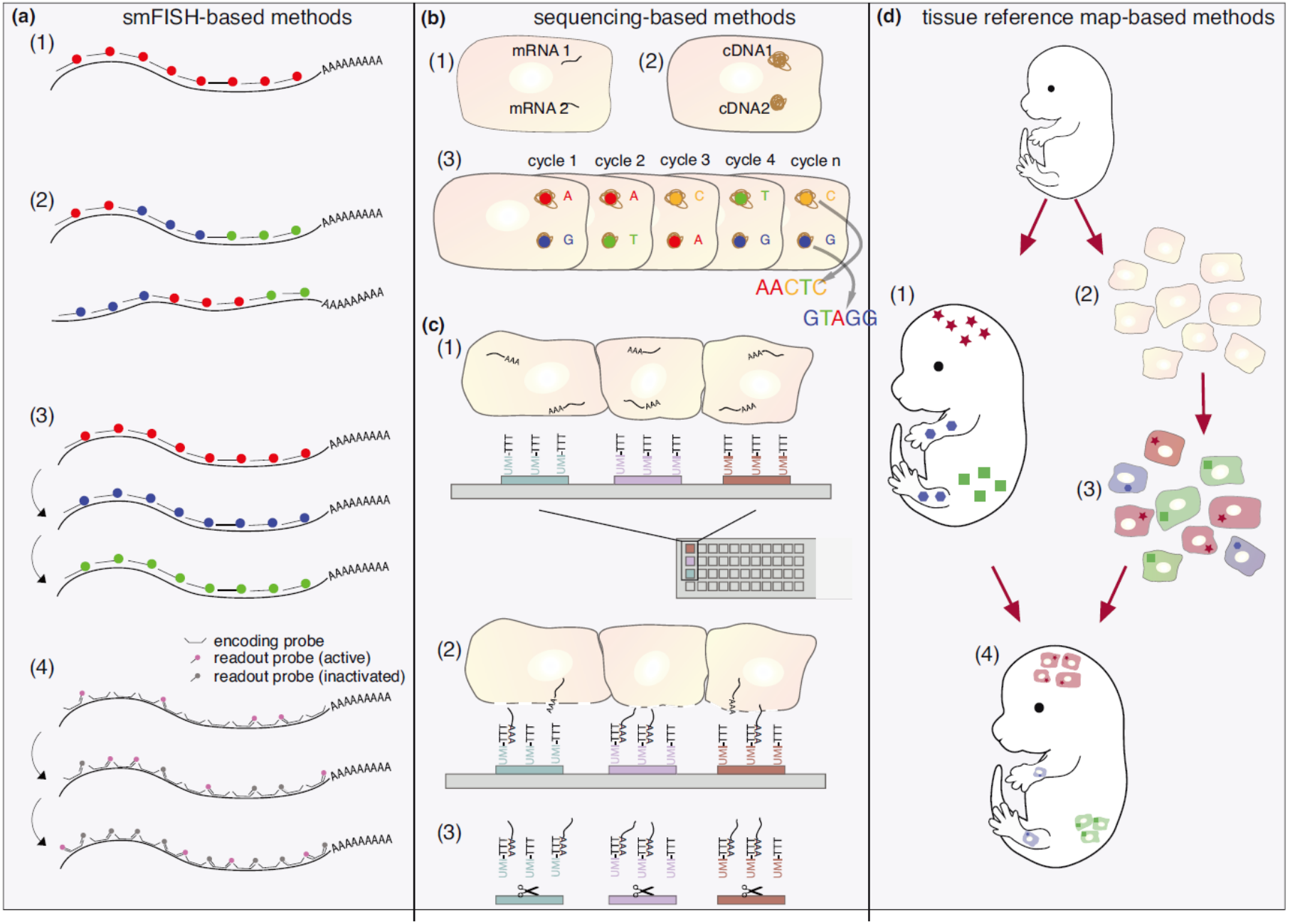

Current Opinion in Biotechnology

mRNA

mRNA exists in a variation of sizes, quantified by their number of nucleotides. For example, the GFP protein has a size between 300 and 1,000 nucleotides. Conversely, mRNA molecules such as the COVID-19 mRNA vaccine and Cas-9 have sizes between 2,000 and 4,000 nucleotides.
Average length 1200-1500 NTs

1 tacacacgaa taaaagataa caaagatgag taaaggagaa gaacttttca ctggagttgt
61 cccaattctt gttgaattag atggcgatgt taatgggcaa aaattctctg tcagtggaga
121 gggtgaaggt gatgcaacat acggaaaact tacccttaaa tttatttgca ctactgggaa
181 gctacctgtt ccatggccaa cacttgtcac tactttctct tatggtgttc aatgcttttc
241 aagataccca gatcatatga aacagcatga ctttttcaag agtgccatgc ccgaaggtta
301 tgtacaggaa agaactatat tttacaaaga tgacgggaac tacaagacac gtgctgaagt
361 caagtttgaa ggtgataccc ttgttaatag aatcgagtta aaaggtattg attttaaaga
421 agatggaaac attcttggac acaaaatgga atacaactat aactcacata atgtatacat
481 catggcagac aaaccaaaga atggaatcaa agttaacttc aaaattagac acaacattaa
541 agatggaagc gttcaattag cagaccatta tcaacaaaat actccaattg gcgatggccc
601 tgtcctttta ccagacaacc attacctgtc cacacaatct gccctttcca aagatcccaa
661 cgaaaagaga gatcacatga tccttcttga gtttgtaaca gctgctggga ttacacatgg
721 catggatgaa ctatacaaat aaatgtccag acttccaatt gacactaaag tgtccgaaca
781 attactaaat tctcagggtt cctggttaaa ttcaggctga gactttattt atatatttat
841 agattcatta aaattttatg aataatttat tgatgttatt aataggggct attttcttat
901 taaataggct actggagtgt at

GFP

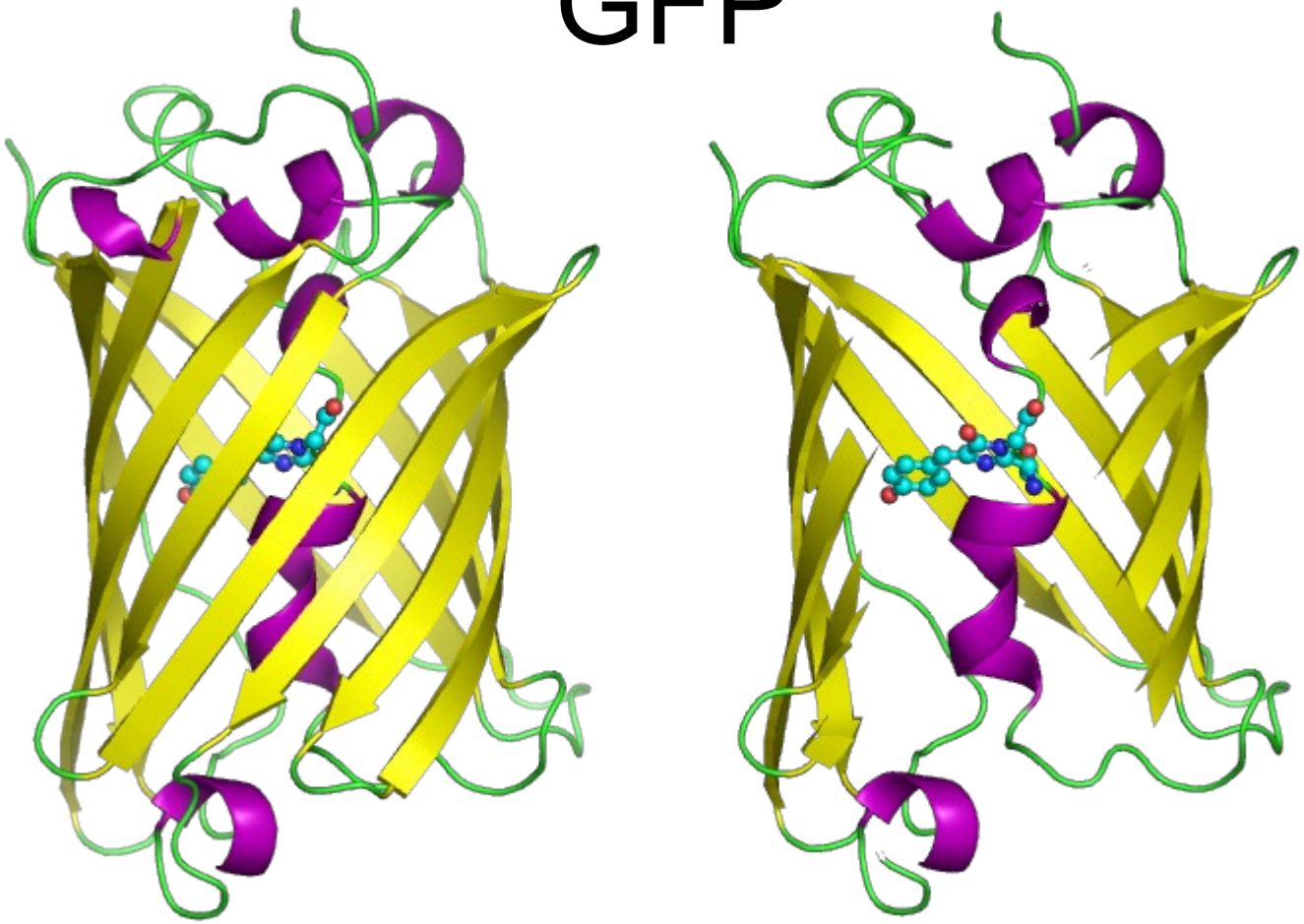

MSKGEELFTGVVPILVELDGDVNGQKFSVSGEGEGDATYGKLTL
KFICTTGKLPVPWPTLVTTFSYGVQCFSRYPDHMKQHDFFKSAMPEGYVQERTIFYKD
DGNYKTRAEVKFEGDTLVNRIELKGIDFKEDGNILGHKMEYNYNSHNVYIMADKPKNG
IKVNFKIRHNIKDGSVQLADHYQQNTPIGDGPVLLPDNHYLSTQSALSKDPNEKRDHM
ILLEFVTAAGITHGMDELYK

FLUORESCENCE IN SITU HYBRIDIZATION (FISH)

Fluorescence in situ hybridization (abbreviated FISH) is a laboratory technique used to detect and locate a specific DNA sequence on a chromosome. In this technique, the full set of chromosomes from an individual is affixed to a glass slide and then exposed to a “probe”—a small piece of purified DNA tagged with a fluorescent dye. The fluorescently labeled probe finds and then binds to its matching sequence within the set of chromosomes. With the use of a special microscope, the chromosome and sub-chromosomal location where the fluorescent probe bound can be seen

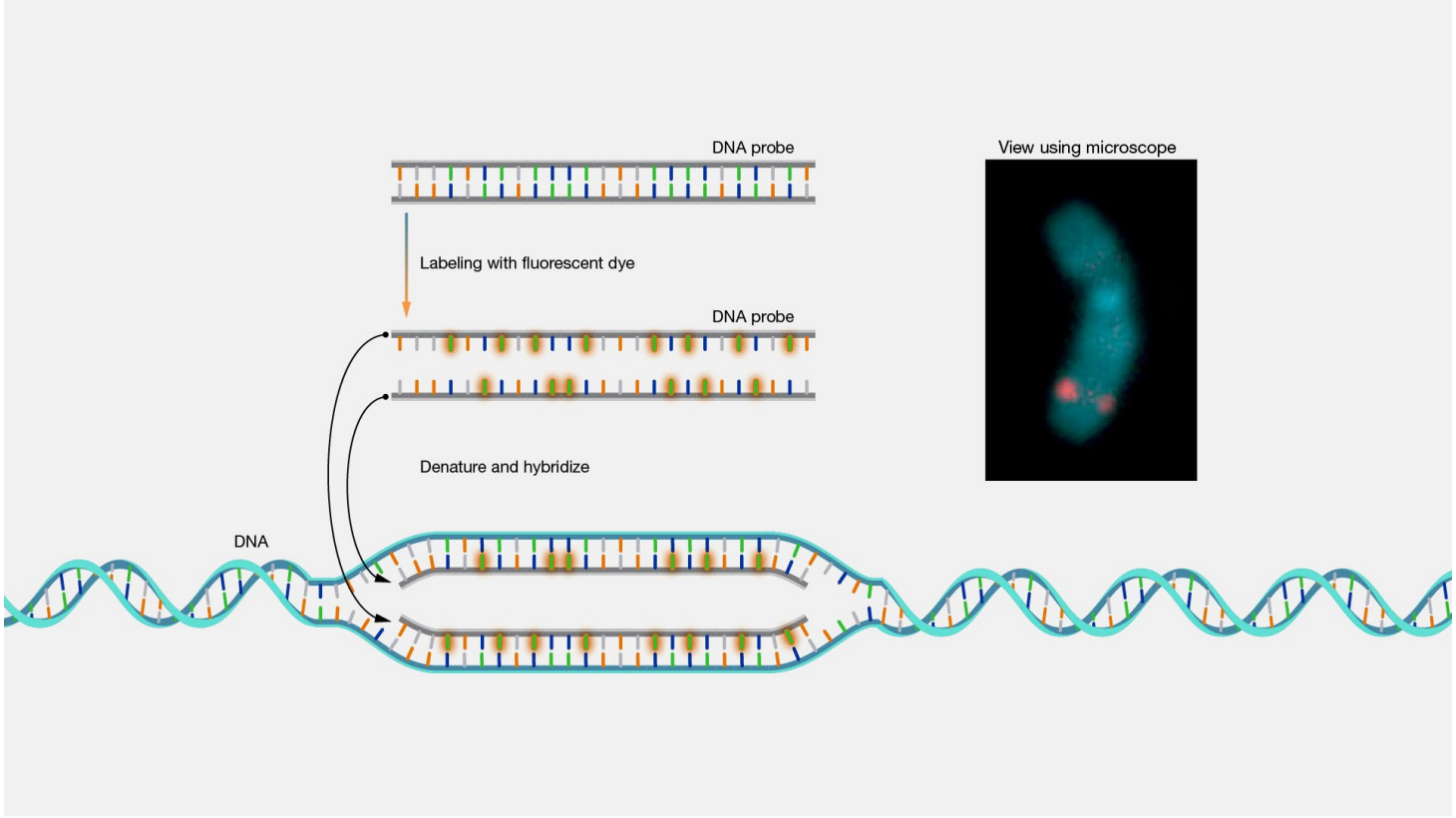

Spatially resolved transcriptomics and beyond

NATURE REVIEWS | GENETICS

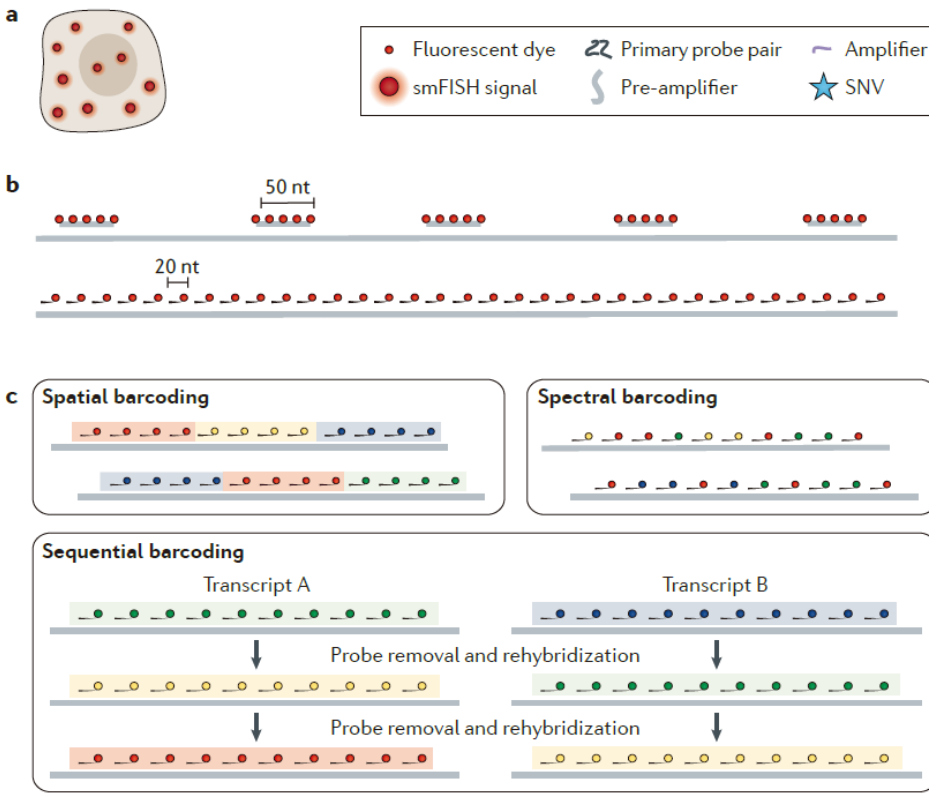

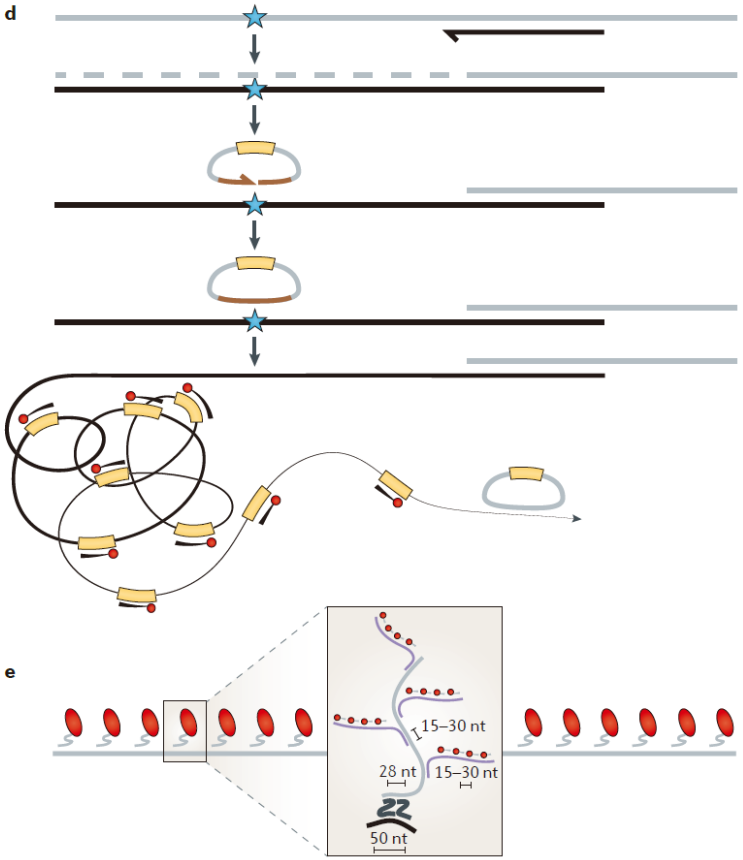

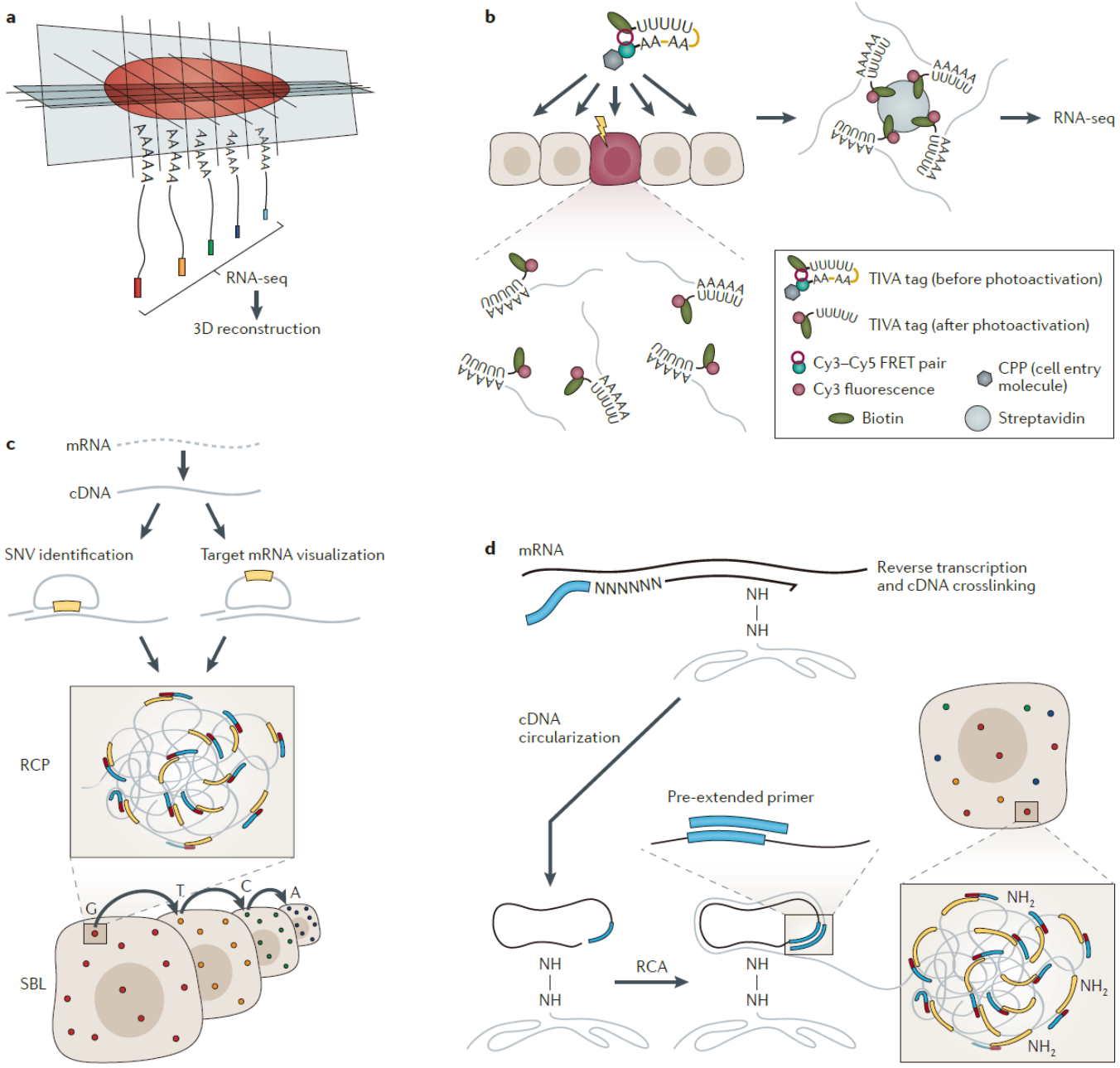
a
RNA-seq
3D reconstruction
b
RNA-seq
TIVA tag (before photoactivation)
TIVA tag (after photoactivation)
Cy3–Cy5 FRET pair
Cy3 fluorescence
CPP (cell entry molecule)
Biotin
Streptavidin
c
mRNA
cDNA
SNV identification
Target mRNA visualization
RCP
SBL
G
T
C
A
d
mRNA
NNNNNN
Reverse transcription and cDNA crosslinking
cDNA circularization
Pre-extended primer
RCA
NH
NH2

	smFISH	Padlock probes and RCA	Branched FISH	LCM	Microtomy sequencing	TIVA	ISS	FISSEQ	Imaging mass cytometry
Sample	Fixed cells and tissues; purified RNA	Fixed cells and tissues; purified DNA or RNA	Fixed cells and tissues; possibly purified DNA or RNA	Fixed tissues	Fixed and fresh tissues	Live cells	Fixed cells and tissues	Fixed cells and tissues	Fixed tissues
Target	RNA	DNA; RNA	RNA	RNA; DNA; proteins	RNA; possibly DNA and proteins	RNA	RNA	RNA	Proteins
Type	Targeted	Targeted	Targeted	Targeted or non-targeted	Non-targeted	Non-targeted	Targeted	Non-targeted	Targeted
Variable measured	Abundance; SNVs; fusion transcripts; splice variants; subcellular localization	Abundance; SNVs; fusion transcripts; splice variants; subcellular localization	Abundance; subcellular localization	Abundance; possibly SNVs, fusion transcripts and splice variants	Abundance; possibly SNVs, fusion transcripts and splice variants	Abundance; possibly SNVs, fusion transcripts and splice variants	Abundance; possibly SNVs, fusion transcripts and splice variants	Abundance; possibly SNVs, fusion transcripts and splice variants	Abundance; protein modifications
Single-cell?	Yes	Yes	Yes	Yes	No	Yes	Yes	Yes	Yes
Spatial resolution	Subcellular	Subcellular	Subcellular (except the nucleus)	Anatomical or cellular	Anatomical	Cellular	Cellular	Cellular	Subcellular
Morphology assessment	Yes	Yes	Yes	Yes	No	Yes	Yes	Yes	Yes
Throughput (number of cells)	Low to medium	Low to medium	Low to medium	Medium	High	Low	Low to medium	Low to medium	Very high
Throughput (number of genes or proteins)	Low to medium	Low to medium	Medium	High	High	High	Low	High	Low
Estimated efficiency	~90%	~30%	NA	NA	~5–10%	NA	NA	NA	NA
Readout	Microscopy; flow cytometry	Microscopy; flow cytometry	Microscopy; flow cytometry	Microarray; RNA-seq; MS	RNA-seq; possibly MS	RNA-seq	Microscopy	Microscopy	MS
Technical difficulty	Easy	Easy	Easy	Moderately easy	Moderately easy	Moderately difficult	Difficult	Difficult	Difficult

Spatially resolved, highly multiplexed RNA profiling in single cells

Kok Hao Chen,[1]* Alistair N. Boettiger,[1]* Jeffrey R. Moffitt,[1]*
Siyuan Wang,[1] Xiaowei Zhuang[1,2]†

412 24 APRIL 2015 • VOL 348 ISSUE 6233 sciencemag.org SCIENCE

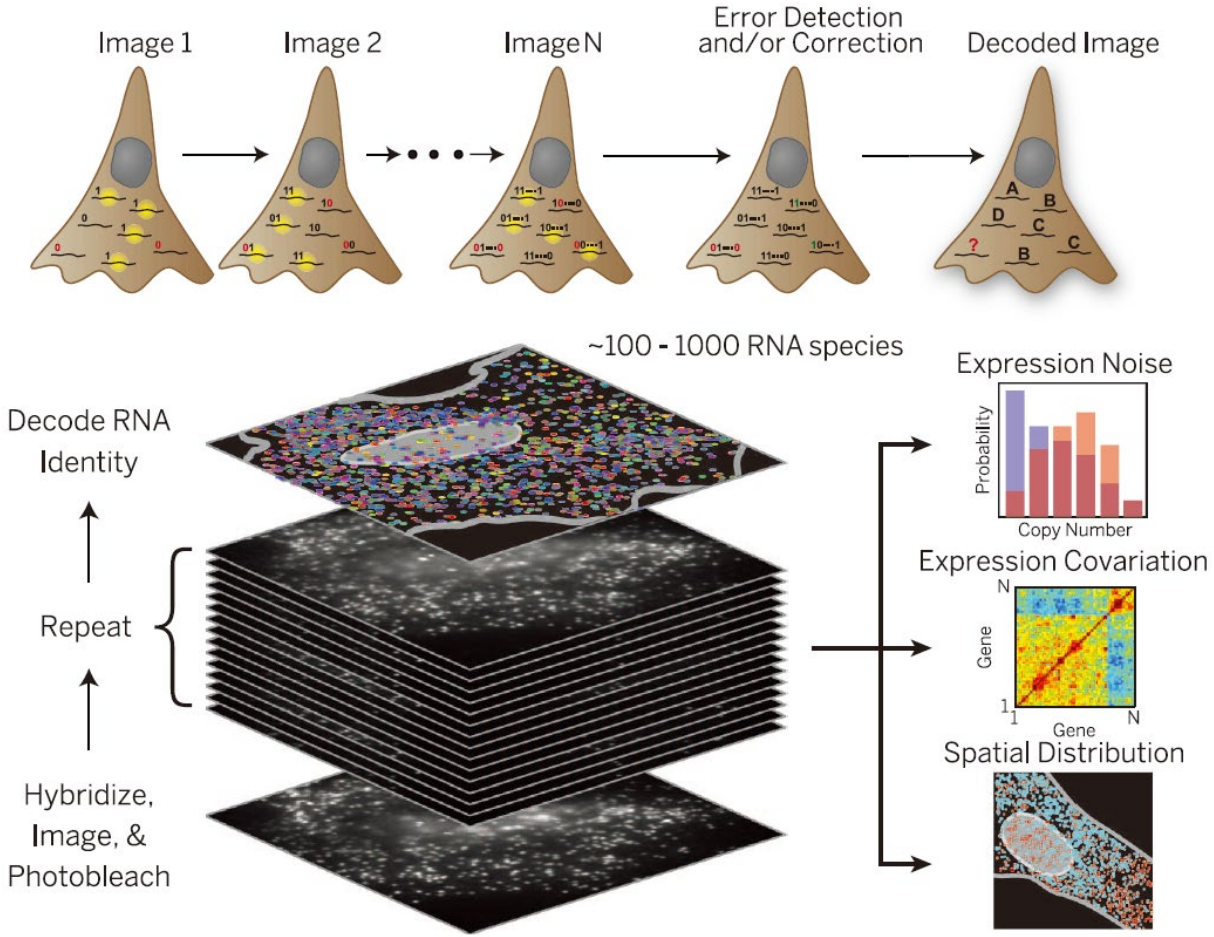

30 nucleotides long, which includes a 20-nucleotide sequence complementary to the target RNA, a 6- to 10-nucleotide readout sequence for the fluorescent readout probe, and a spacer region.

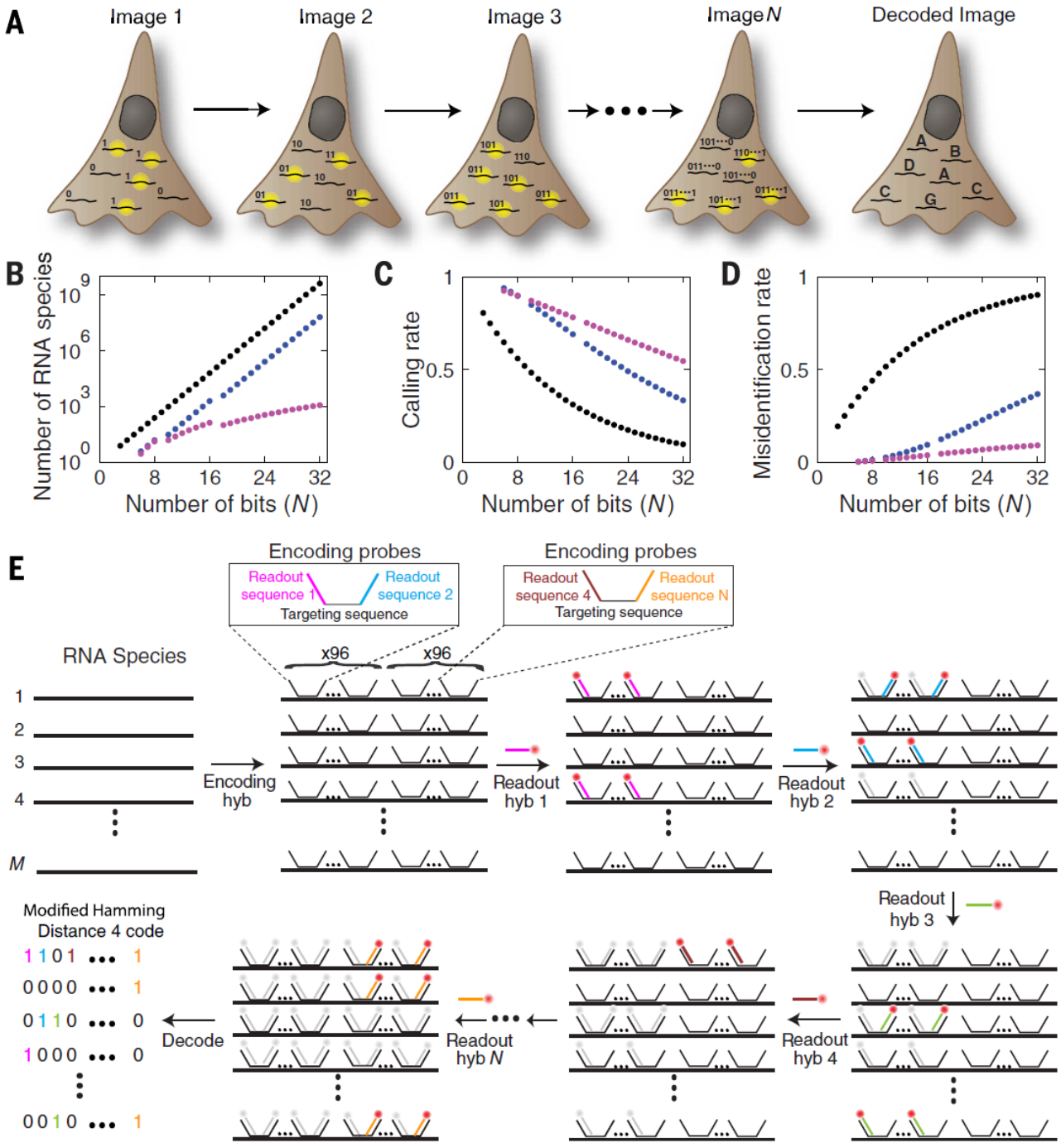
A
Image 1
Image 2
Image 3
Image N
Decoded Image
B
Number of RNA species
Number of bits (N)
C
Calling rate
Number of bits (N)
D
Misidentification rate
Number of bits (N)
E
Encoding probes
Readout sequence 1
Readout sequence 2
Targeting sequence
Encoding probes
Readout sequence 4
Readout sequence N
Targeting sequence
RNA Species
x96
x96
Encoding hyb
Readout hyb 1
Readout hyb 2
Readout hyb 3
Readout hyb 4
Readout hyb N
Decode
Modified Hamming Distance 4 code

around 16-48 probes were used per mRNA molecule, depending on the length and sequence of the mRNA. The study used a set of 130 probes targeting 130 different mRNAs in single cells.

In the original MERFISH paper, the authors used a pool of 130 probes, each targeting one of 130 different mRNAs in single cells. For each mRNA species, they designed a set of 16-48 oligonucleotide probes. The exact number of probes for each mRNA varied depending on the length and sequence of the mRNA.

Thus, the total number of probes used in the experiment is the sum of all the individual probe sets for the 130 mRNAs. While the exact total number of probes is not provided in the paper, considering an average of 32 probes per mRNA (midpoint of the 16-48 range), the total number of probes would be approximately:

32 probes/mRNA * 130 mRNA species ≈ 4,160 probes

In the original MERFISH paper, the authors used 16 distinct readout sequences and two spectrally distinct dyes. The 16 readout sequences corresponded to 16 different binary bits in the error-robust barcodes assigned to each mRNA species. Each of these readout sequences was conjugated to a fluorophore in one of two colors.

The authors performed eight sequential imaging rounds, hybridizing and imaging a combination of eight readout probes per round (one for each bit position in the binary barcode). In each imaging round, a subset of the 16 readout sequences was labeled with one of the two colors, resulting in 2^16 or 65,536 potential binary barcodes.

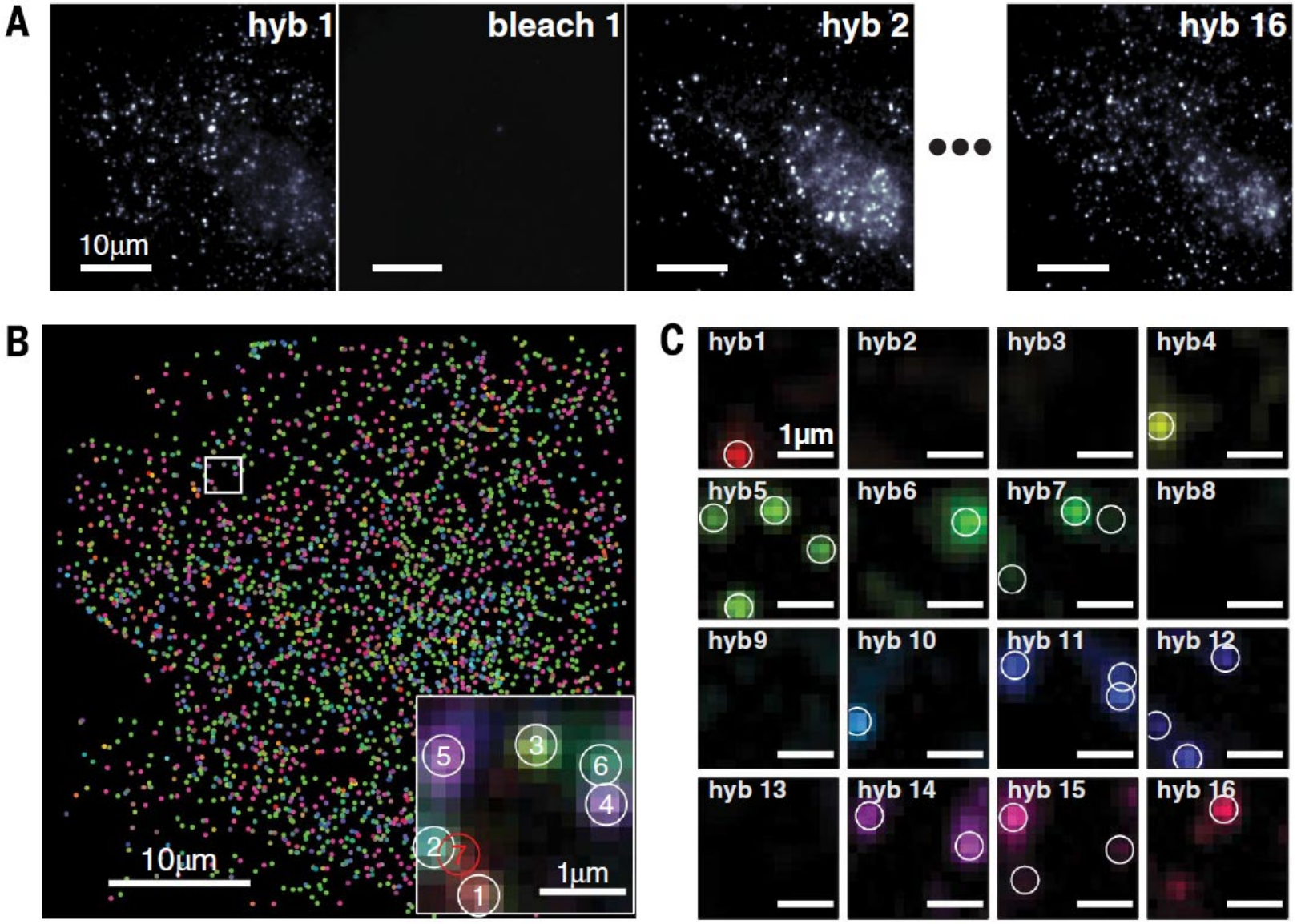
A
hyb 1
bleach 1
hyb 2
hyb 16
10μm
B
10μm
1μm
1
2
3
4
5
6
7
C
hyb1
hyb2
hyb3
hyb4
1μm
hyb5
hyb6
hyb7
hyb8
hyb9
hyb 10
hyb 11
hyb 12
hyb 13
hyb 14
hyb 15
hyb 16

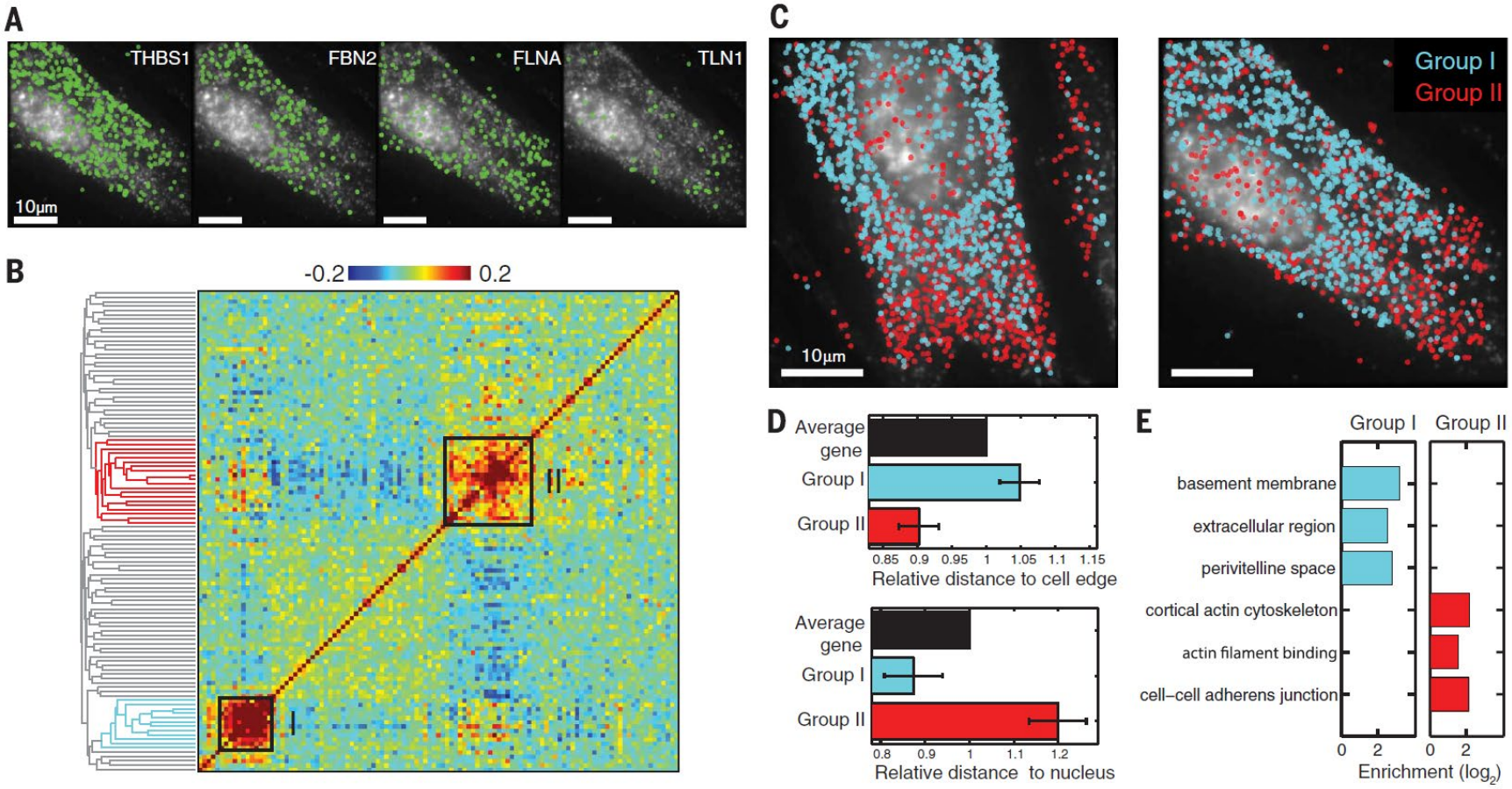
A
THBS1
FBN2
FLNA
TLN1
10μm
B
-0.2
0.2
I
II
C
10μm
Group I
Group II
D
Average gene
Group I
Group II
0.85 0.9 0.95 1 1.05 1.1 1.15
Relative distance to cell edge
Average gene
Group I
Group II
0.8 0.9 1 1.1 1.2
Relative distance to nucleus
E
Group I
Group II
basement membrane
extracellular region
perivitelline space
cortical actin cytoskeleton
actin filament binding
cell–cell adherens junction
0 2
0 2
Enrichment (log2)

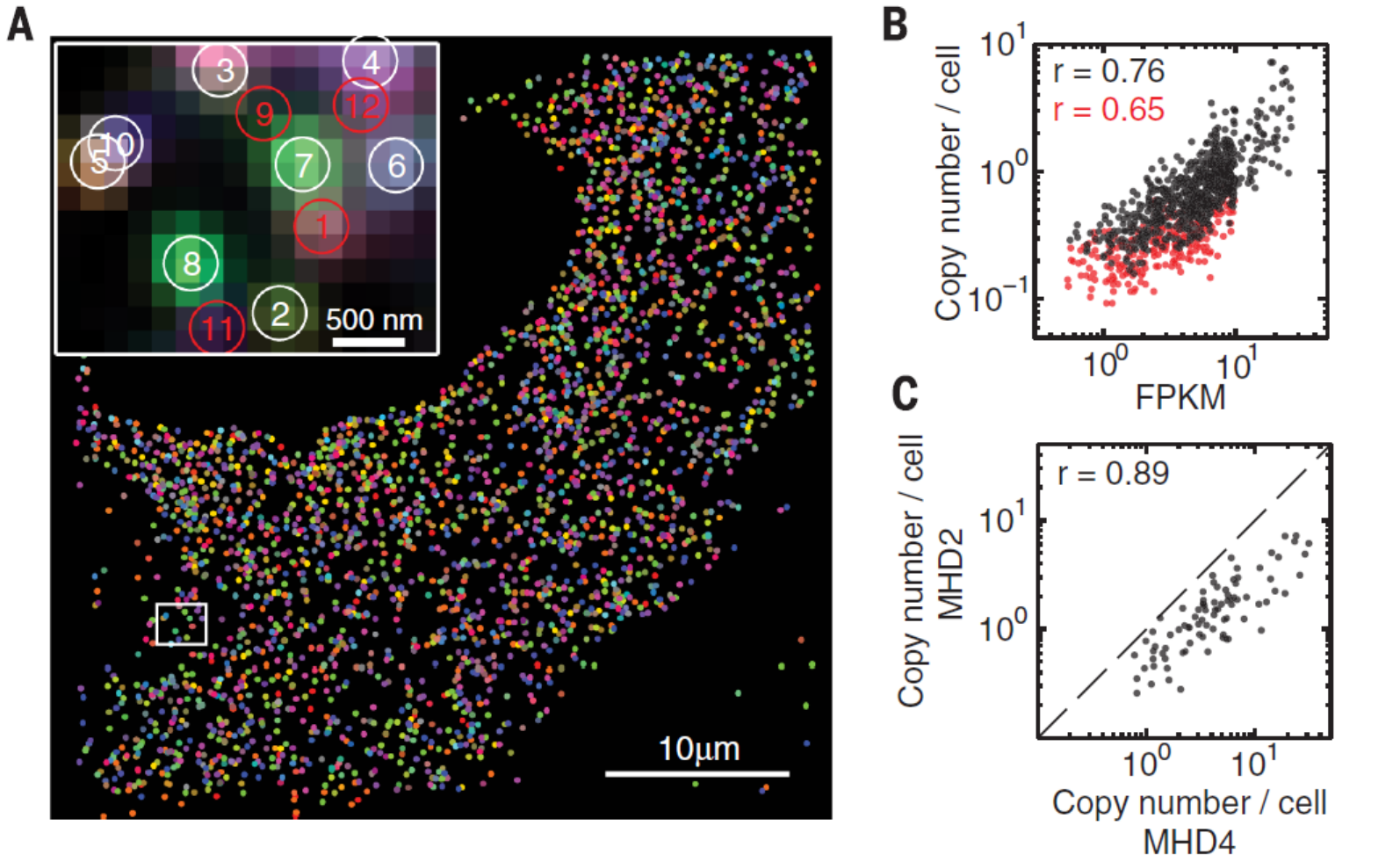

Fig. 5. Simultaneous measurements of 1001 RNA species in single cells by using MERFISH with a 14-bit MHD2 code. (**A**) The localizations of all detected single molecules in a cell colored based on their measured binary words. (Inset) The composite, false-colored fluorescent image of the 14 hybridization

Molecular, spatial, and functional single-cell profiling of the hypothalamic preoptic region

Moffitt *et al.*, *Science* **362**, 792 (2018)

Jeffrey R. Moffitt*, Dhananjay Bambah-Mukku*, Stephen W. Eichhorn†, Eric Vaughn†, Karthik Shekhar, Julio D. Perez, Nimrod D. Rubinstein, Junjie Hao, Aviv Regev, Catherine Dulac‡§, Xiaowei Zhuang‡§

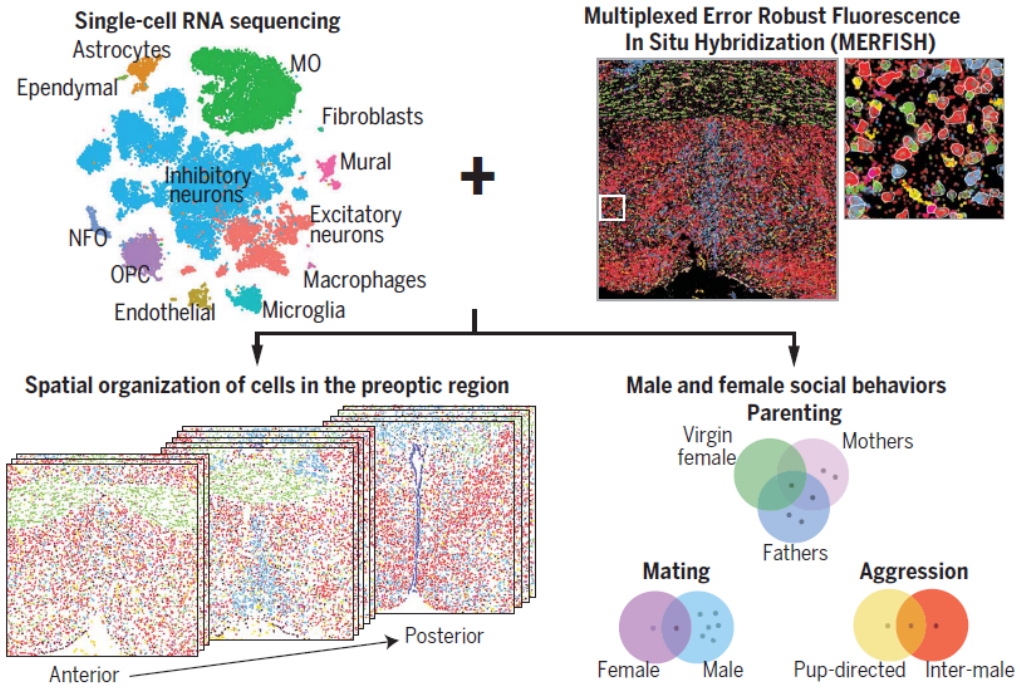

In situ single-cell profiling reveals the molecular and cellular organization of the hypothalamic preoptic region. The combination of MERFISH with scRNA-seq to profile the gene expression of 1 million cells in situ revealed ~70 neuronal populations in the preoptic region, each with distinct molecular signatures and spatial organizations, providing insights into neuromodulatory signaling pathways. Further combination with activity marker imaging led to the identification of discrete neuronal types activated by key social behaviors, including parenting, aggression, and mating.

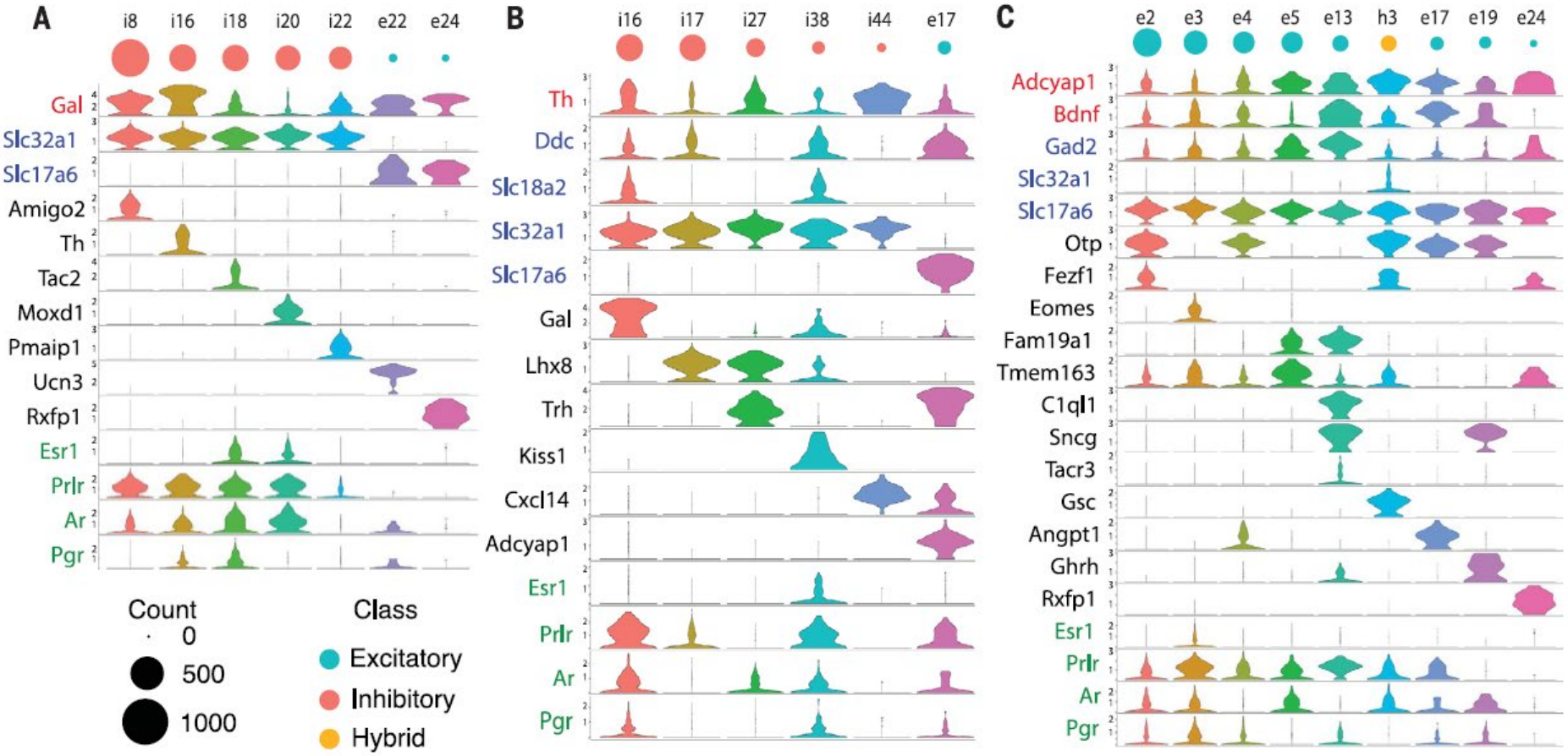
A
i8
i16
i18
i20
i22
e22
e24
Gal
Slc32a1
Slc17a6
Amigo2
Th
Tac2
Moxd1
Pmaip1
Ucn3
Rxfp1
Esr1
Prlr
Ar
Pgr
Count
0
500
1000
Class
Excitatory
Inhibitory
Hybrid
B
i16
i17
i27
i38
i44
e17
Th
Ddc
Slc18a2
Slc32a1
Slc17a6
Gal
Lhx8
Trh
Kiss1
Cxcl14
Adcyap1
Esr1
Prlr
Ar
Pgr
C
e2
e3
e4
e5
e13
h3
e17
e19
e24
Adcyap1
Bdnf
Gad2
Slc32a1
Slc17a6
Otp
Fezf1
Eomes
Fam19a1
Tmem163
C1ql1
Sncg
Tacr3
Gsc
Angpt1
Ghrh
Rxfp1
Esr1
Prlr
Ar
Pgr

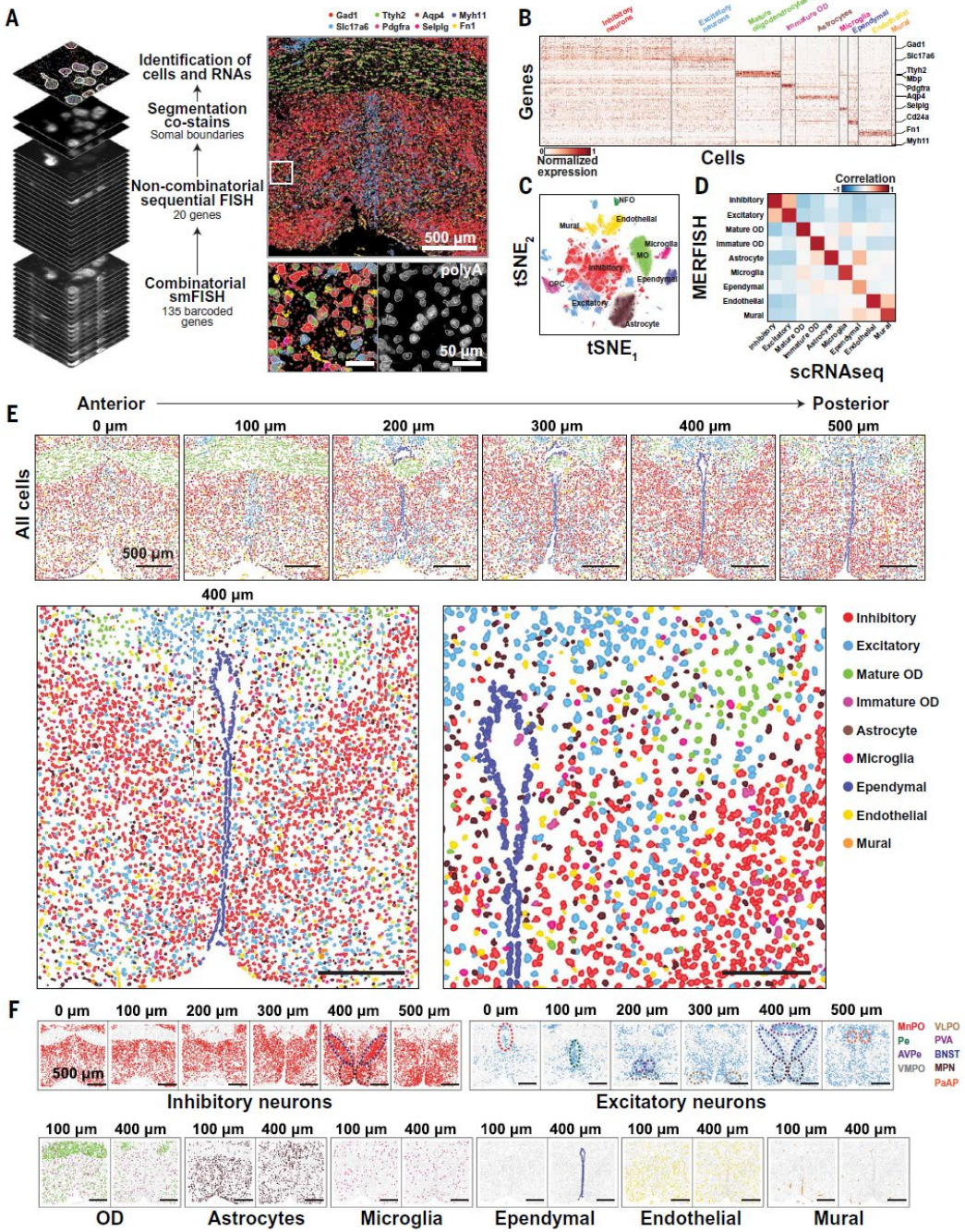
A
Identification of cells and RNAs
Segmentation co-stains
Somal boundaries
Non-combinatorial sequential FISH
20 genes
Combinatorial smFISH
135 barcoded genes
Gad1 Slc17a6 Ttyh2 Pdgfra Aqp4 Selplg Myh11 Fn1
500 μm
polyA
50 μm
B
Genes
Cells
Normalized expression
Gad1
Slc17a6
Ttyh2
Mbp
Pdgfra
Aqp4
Selplg
Cd24a
Fn1
Myh11
C
tSNE2
tSNE1
NFO
Endothelial
Mural
Microglia
MO
Inhibitory
Ependymal
OPC
Excitatory
Astrocyte
D
MERFISH
scRNAseq
Correlation
Inhibitory
Excitatory
Mature OD
Immature OD
Astrocyte
Microglia
Ependymal
Endothelial
Mural
E
Anterior
Posterior
0 μm
100 μm
200 μm
300 μm
400 μm
500 μm
All cells
500 μm
400 μm
Inhibitory
Excitatory
Mature OD
Immature OD
Astrocyte
Microglia
Ependymal
Endothelial
Mural
F
0 μm
100 μm
200 μm
300 μm
400 μm
500 μm
500 μm
Inhibitory neurons
Excitatory neurons
MnPO
Pe
AVPe
VMPO
VLPO
PVA
BNST
MPN
PaAP
100 μm
400 μm
OD
Astrocytes
Microglia
Ependymal
Endothelial
Mural

Spatial transcriptome profiling by MERFISH reveals subcellular RNA compartmentalization and cell cycle-dependent gene expression

Chenglong Xia[a,b,c,1], Jean Fan[a,b,c,1], George Emanuel[a,b,c,1], Junjie Hao[a,b,c], and Xiaowei Zhuang[a,b,c,2]

[a]Howard Hughes Medical Institute, Harvard University, Cambridge, MA 02138; [b]Department of Chemistry and Chemical Biology, Harvard Universi
Cambridge, MA 02138; and [c]Department of Physics, Harvard University, Cambridge, MA 02138

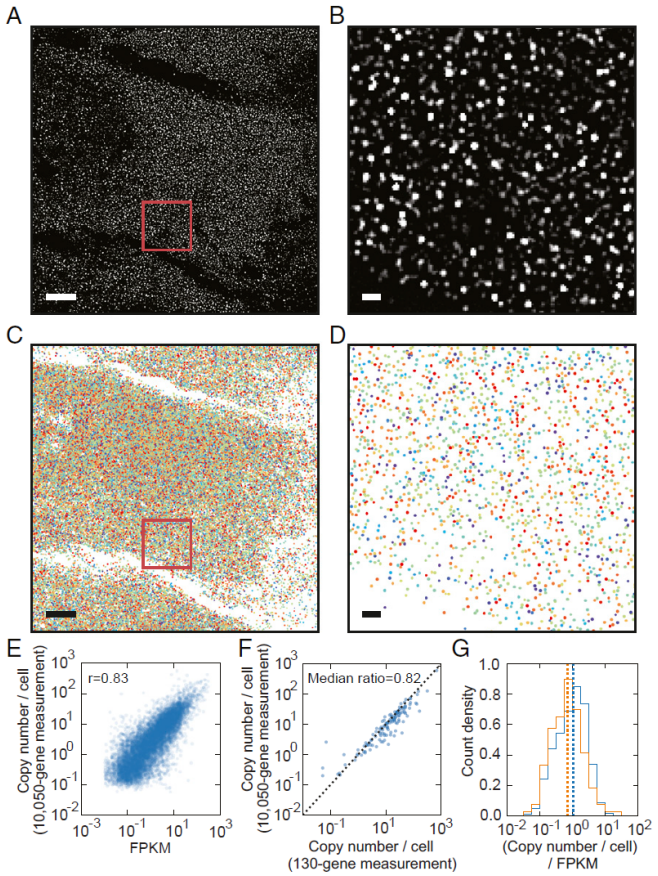

Fig. 1. MERFISH imaging of 10,050 genes in individual U-2 OS cells. (*A*) A high-pass-filtered, single-*z* slice, single-bit image of a U-2 OS sample stained with

Multiplexed imaging of high-density libraries of RNAs with MERFISH and expansion microscopy

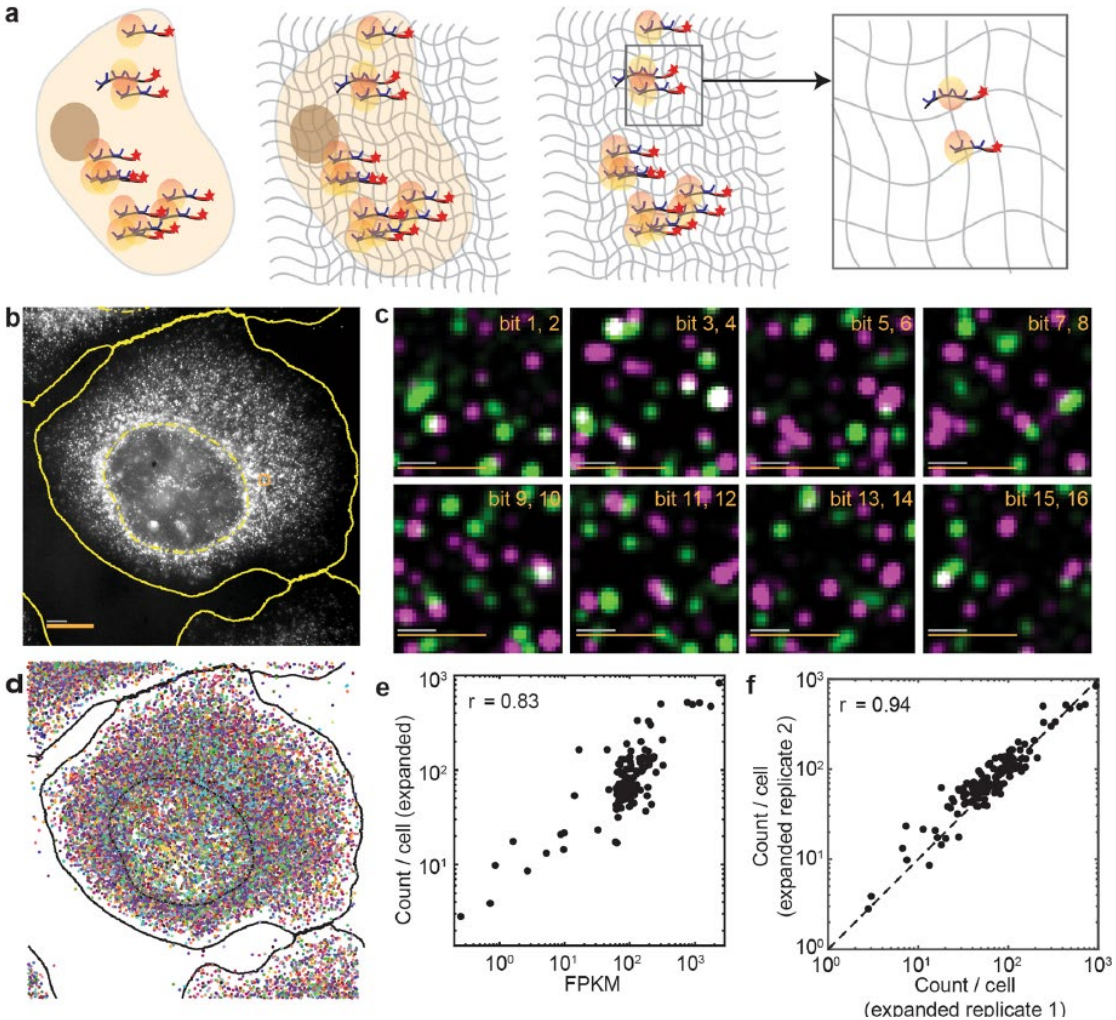

Transcriptome-scale super-resolved imaging in tissues by RNA seqFISH+

Chee-Huat Linus Eng[1], Michael Lawson[2], Qian Zhu[3], Ruben Dries[3], Noushin Koulena[2], Yodai Takei[2], Jina Yun[2], Christopher Cronin[2], Christoph Karp[2], Guo-Cheng Yuan[3] & Long Cai[2]*

11 APRIL 2019 | VOL 568 | NATURE | 235

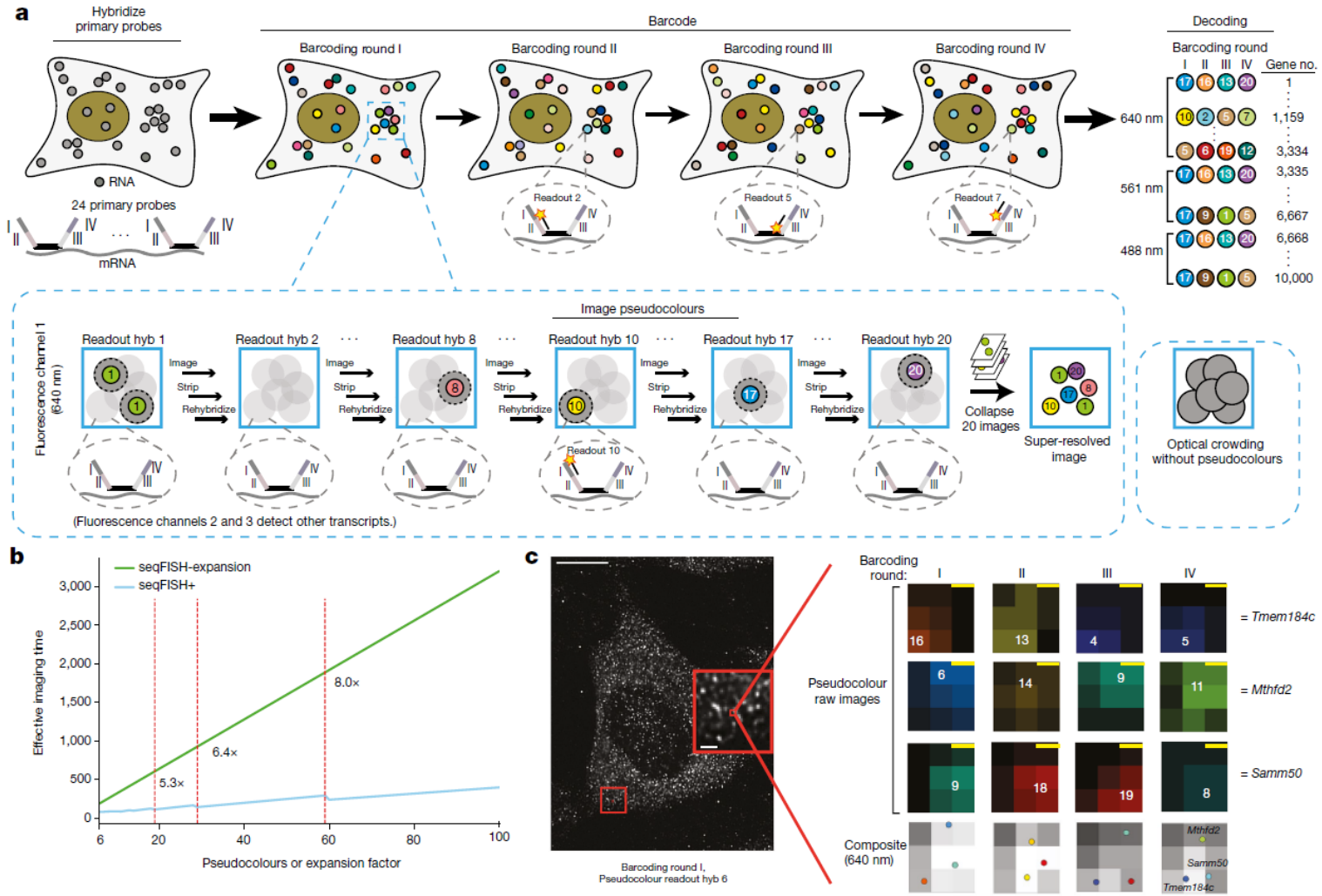

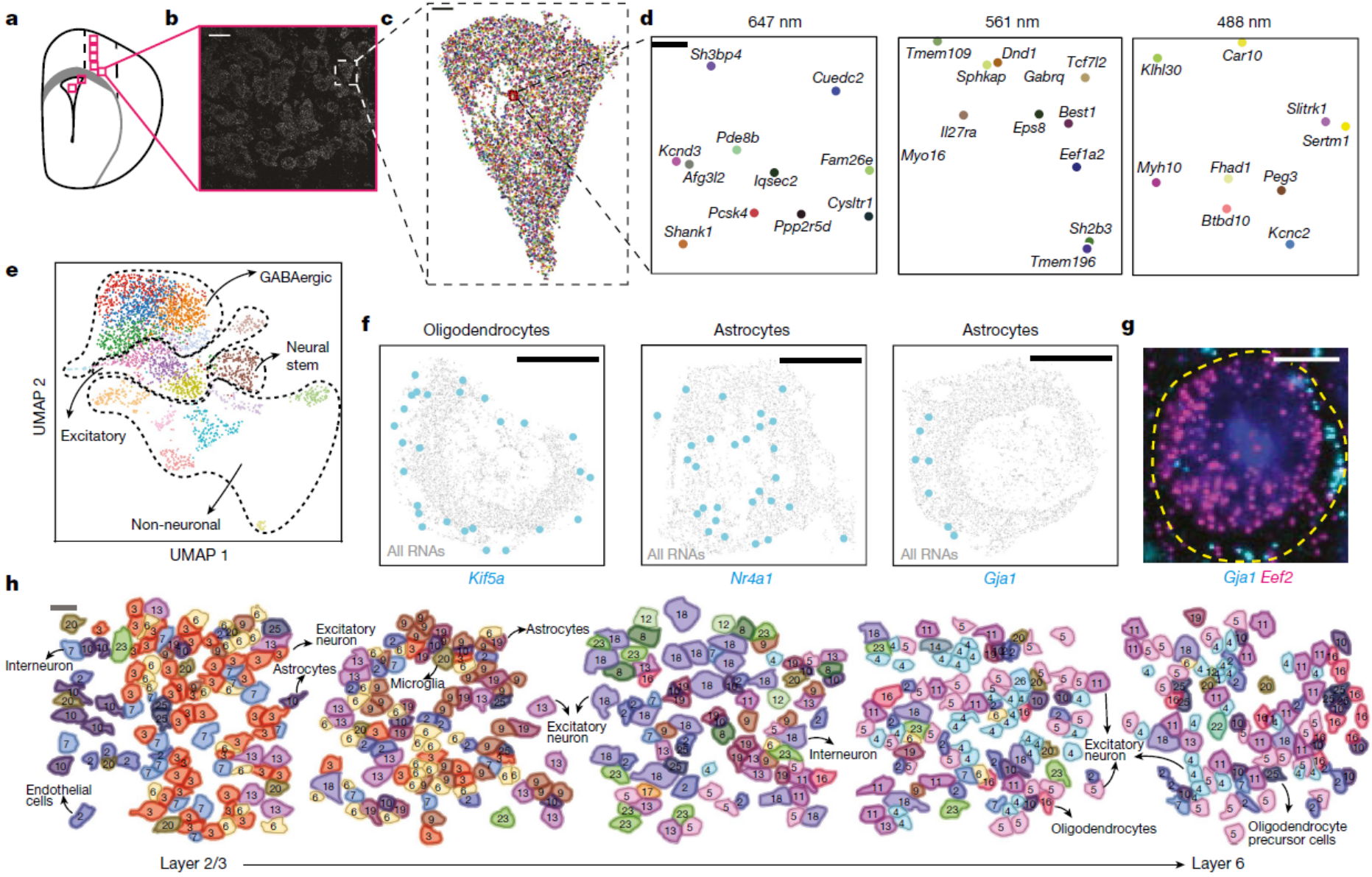
a
b
c
d
647 nm
561 nm
488 nm
Sh3bp4
Cuedc2
Pde8b
Kcnd3
Afg3l2
Iqsec2
Fam26e
Cysltr1
Pcsk4
Ppp2r5d
Shank1
Tmem109
Dnd1
Tcf7l2
Sphkap
Gabrq
Best1
Il27ra
Eps8
Myo16
Eef1a2
Sh2b3
Tmem196
Klhl30
Car10
Slitrk1
Sertm1
Myh10
Fhad1
Peg3
Btbd10
Kcnc2
e
GABAergic
Neural stem
Excitatory
Non-neuronal
UMAP 2
UMAP 1
f
Oligodendrocytes
Astrocytes
Astrocytes
All RNAs
Kif5a
Nr4a1
Gja1
g
Gja1 Eef2
h
Interneuron
Excitatory neuron
Astrocytes
Microglia
Endothelial cells
Layer 2/3
Layer 6
Oligodendrocytes
Oligodendrocyte precursor cells

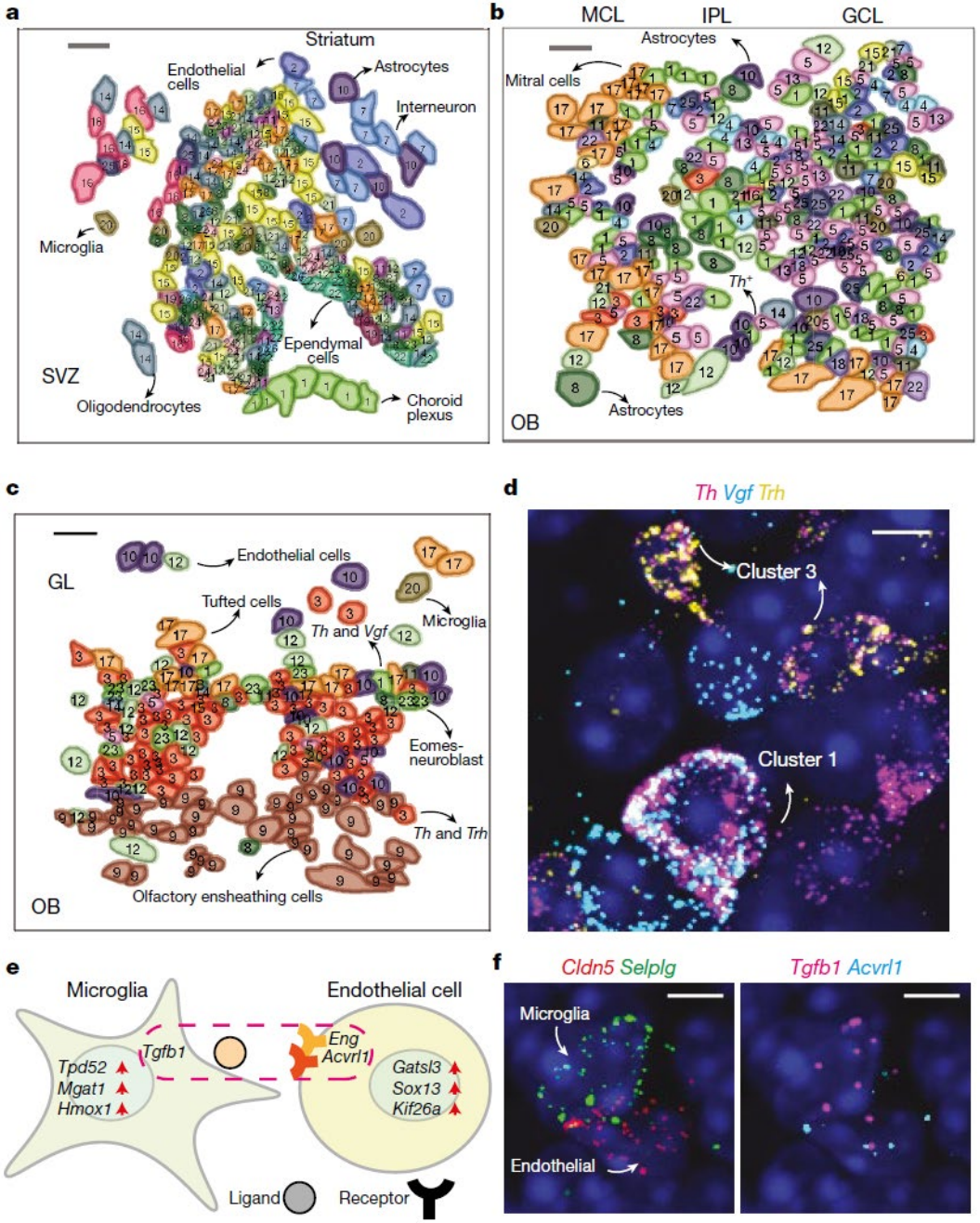
a
Striatum
Endothelial cells
Astrocytes
Interneuron
Microglia
Ependymal cells
SVZ
Oligodendrocytes
Choroid plexus
b
MCL
IPL
GCL
Astrocytes
Mitral cells
Th+
Astrocytes
OB
c
GL
Endothelial cells
Tufted cells
Microglia
Th and Vgf
Eomes-neuroblast
Th and Trh
Olfactory ensheathing cells
OB
d
Th Vgf Trh
Cluster 3
Cluster 1
e
Microglia
Endothelial cell
Tgfb1
Eng
Acvrl1
Tpd52
Mgat1
Hmox1
Gatsl3
Sox13
Kif26a
Ligand
Receptor
f
Cldn5 Selplg
Tgfb1 Acvrl1
Microglia
Endothelial

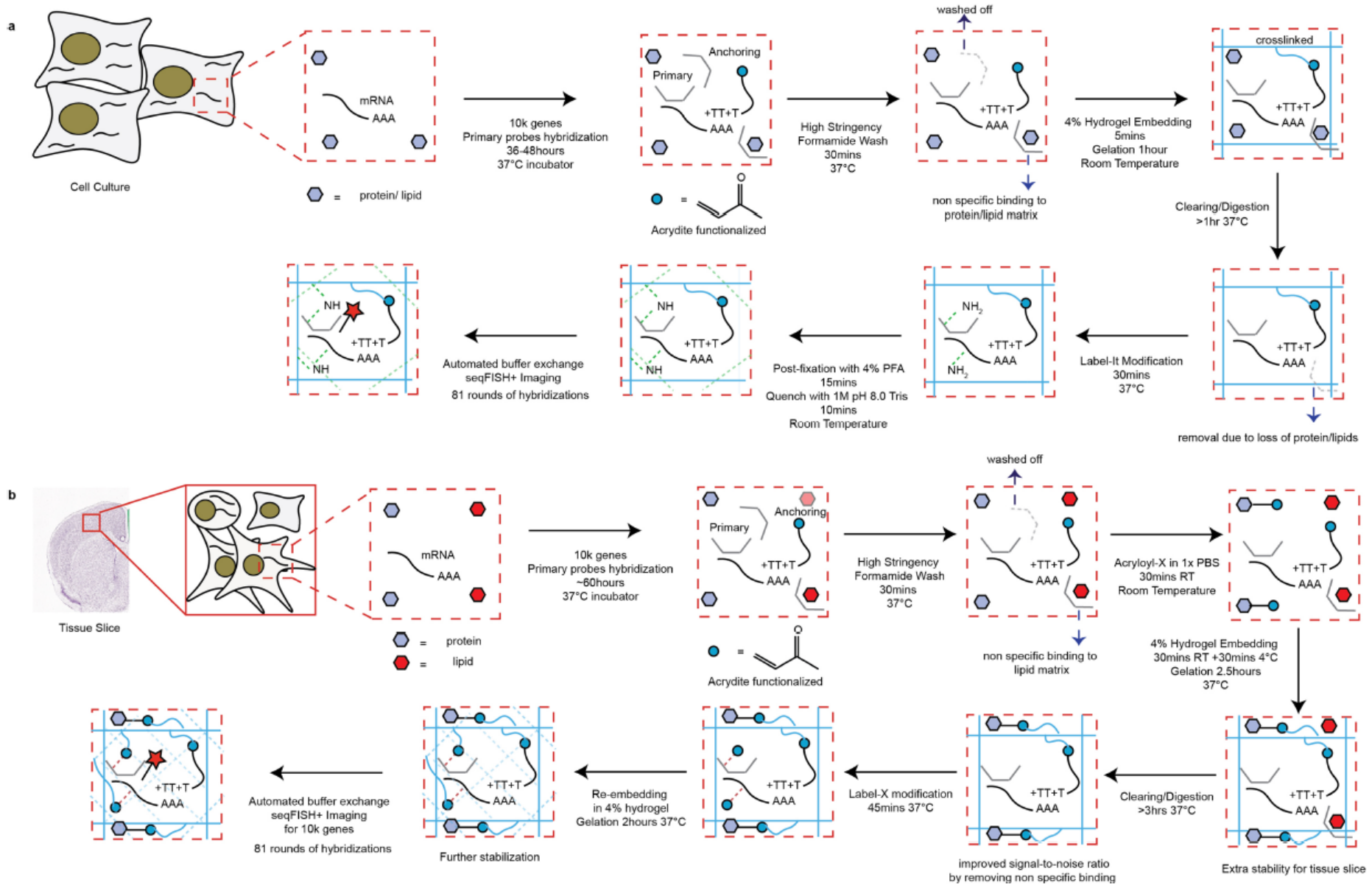

Extended Data Fig. 1 | Clearing and probe-anchoring protocols. a, b, seqFISH+ experiments in NIH/3T3 cells (**a**) and the mouse brain slices (**b**).

Visualization and analysis of gene expression in tissue sections by spatial transcriptomics

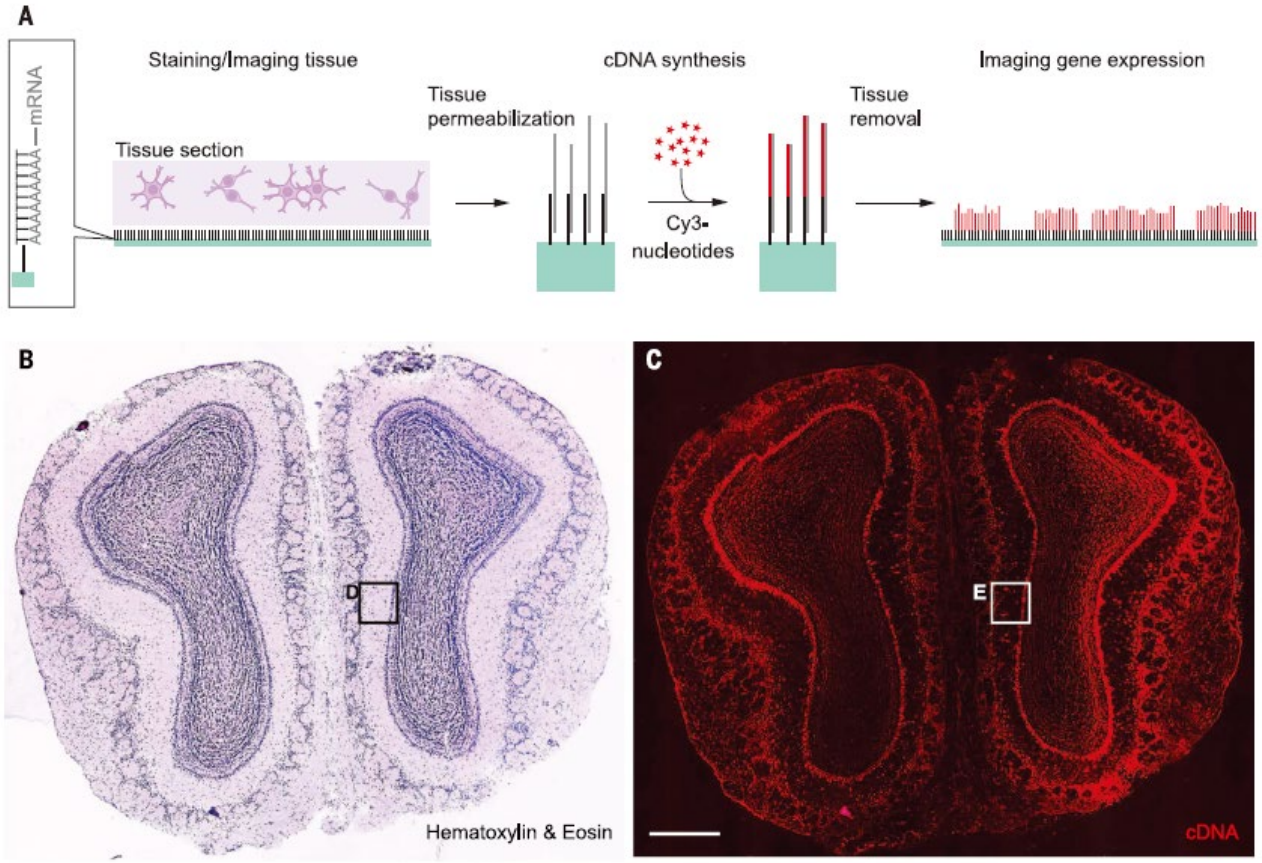

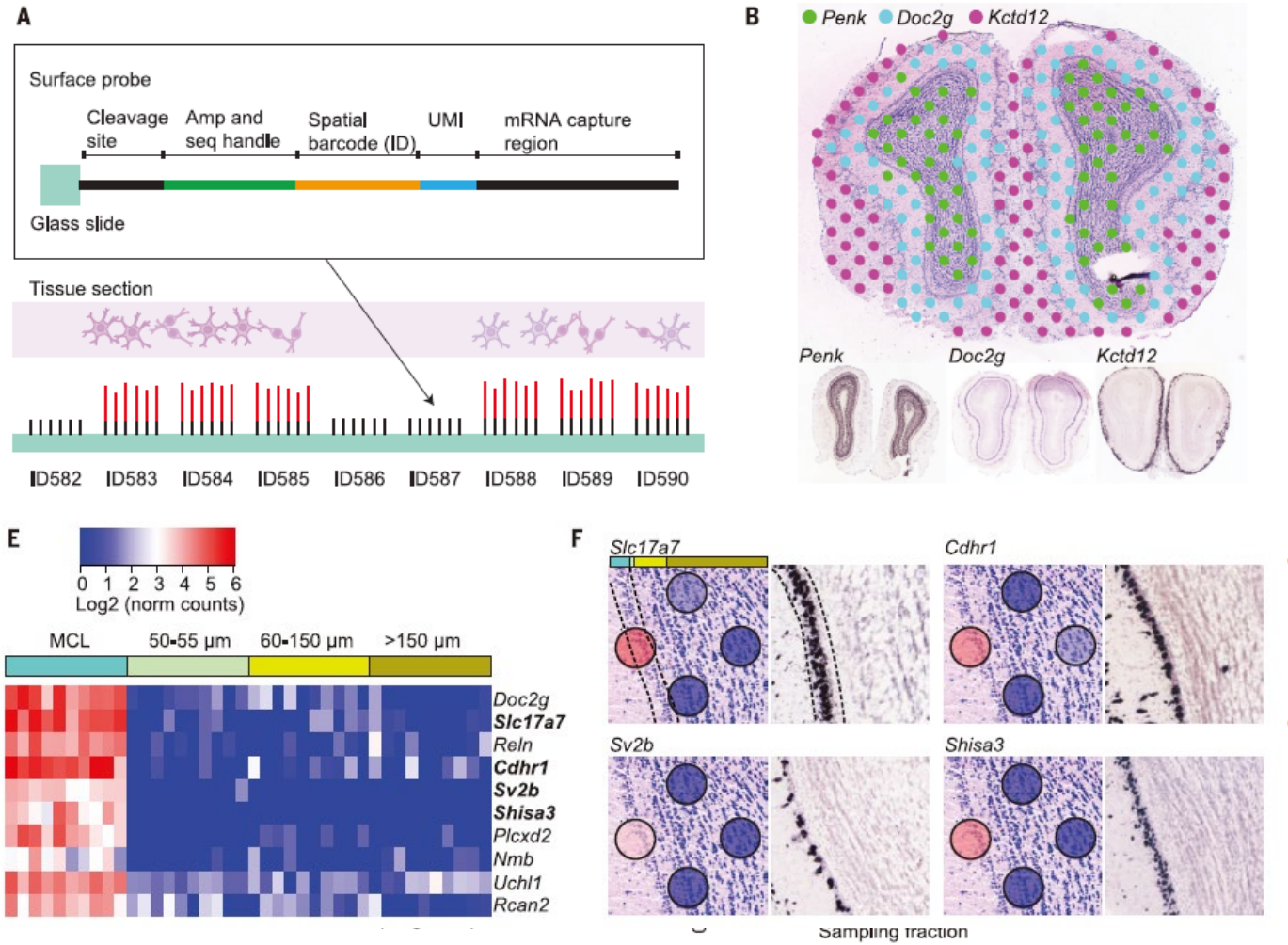
A
Surface probe
Cleavage site
Amp and seq handle
Spatial barcode (ID)
UMI
mRNA capture region
Glass slide
Tissue section
ID582 ID583 ID584 ID585 ID586 ID587 ID588 ID589 ID590
B
Penk Doc2g Kctd12
Penk
Doc2g
Kctd12
E
0 1 2 3 4 5 6
Log2 (norm counts)
MCL
50-55 µm
60-150 µm
>150 µm
Doc2g
Slc17a7
Reln
Cdhr1
Sv2b
Shisa3
Plcxd2
Nmb
Uchl1
Rcan2
F
Slc17a7
Cdhr1
Sv2b
Shisa3
Sampling fraction

UMI and Barcode

Unique Molecular Identifier (UMI): A UMI is a short, random sequence of nucleotides that is attached to individual mRNA molecules during library preparation for sequencing experiments. The primary purpose of a UMI is to label each original mRNA molecule uniquely, allowing for accurate quantification of gene expression by distinguishing between PCR duplicates and independent molecules originating from the same gene. This helps to correct for PCR bias and improves the overall quality and reliability of the gene expression data.

Barcode: In spatially resolved transcriptomics, a barcode typically refers to a short, known sequence of nucleotides that is used to label transcripts based on their spatial origin within a tissue. Barcodes can be introduced during library preparation or directly on the capture probes or primers used for in situ sequencing or hybridization-based techniques. The primary purpose of a barcode is to enable the assignment of sequenced transcripts back to their original spatial location within the tissue, allowing for the reconstruction of spatial gene expression patterns.

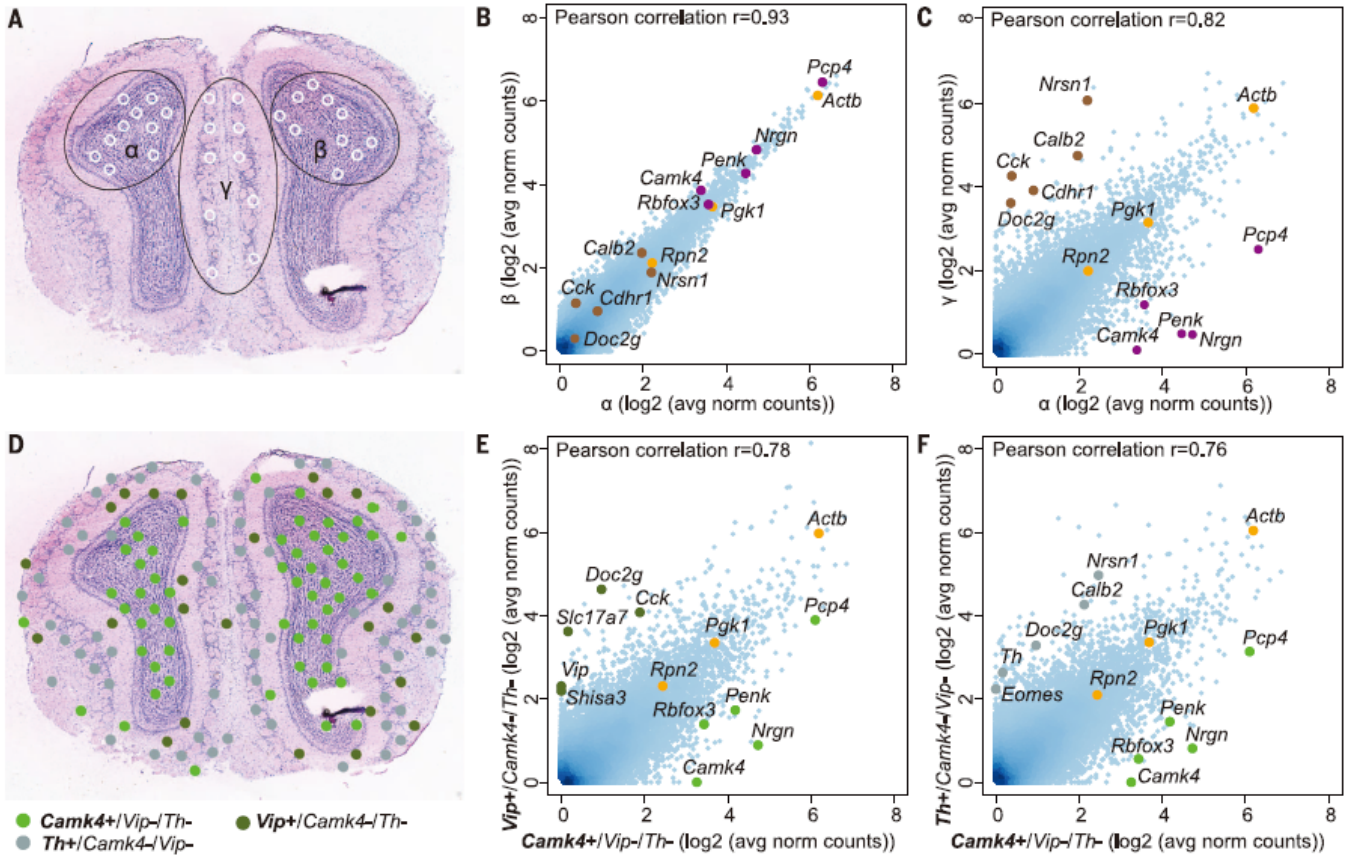
A
α
γ
β
B
Pearson correlation r=0.93
β (log2 (avg norm counts))
α (log2 (avg norm counts))
Pcp4
Actb
Nrgn
Penk
Camk4
Rbfox3
Pgk1
Calb2
Rpn2
Nrsn1
Cck
Cdhr1
Doc2g
C
Pearson correlation r=0.82
γ (log2 (avg norm counts))
α (log2 (avg norm counts))
Nrsn1
Actb
Calb2
Cck
Cdhr1
Doc2g
Pgk1
Pcp4
Rpn2
Rbfox3
Penk
Camk4
Nrgn
D
Camk4+/Vip-/Th-
Vip+/Camk4-/Th-
Th+/Camk4-/Vip-
E
Pearson correlation r=0.78
Vip+/Camk4-/Th- (log2 (avg norm counts))
Camk4+/Vip-/Th- (log2 (avg norm counts))
Actb
Doc2g
Cck
Slc17a7
Pcp4
Pgk1
Vip
Rpn2
Shisa3
Penk
Rbfox3
Nrgn
Camk4
F
Pearson correlation r=0.76
Th+/Camk4-/Vip- (log2 (avg norm counts))
Camk4+/Vip-/Th- (log2 (avg norm counts))
Actb
Nrsn1
Calb2
Doc2g
Pgk1
Pcp4
Th
Rpn2
Eomes
Penk
Nrgn
Rbfox3
Camk4

Rodriques *et al.*, *Science* **363**, 1463–1467 (2019)

Slide-seq: A scalable technology for measuring genome-wide expression at high spatial resolution

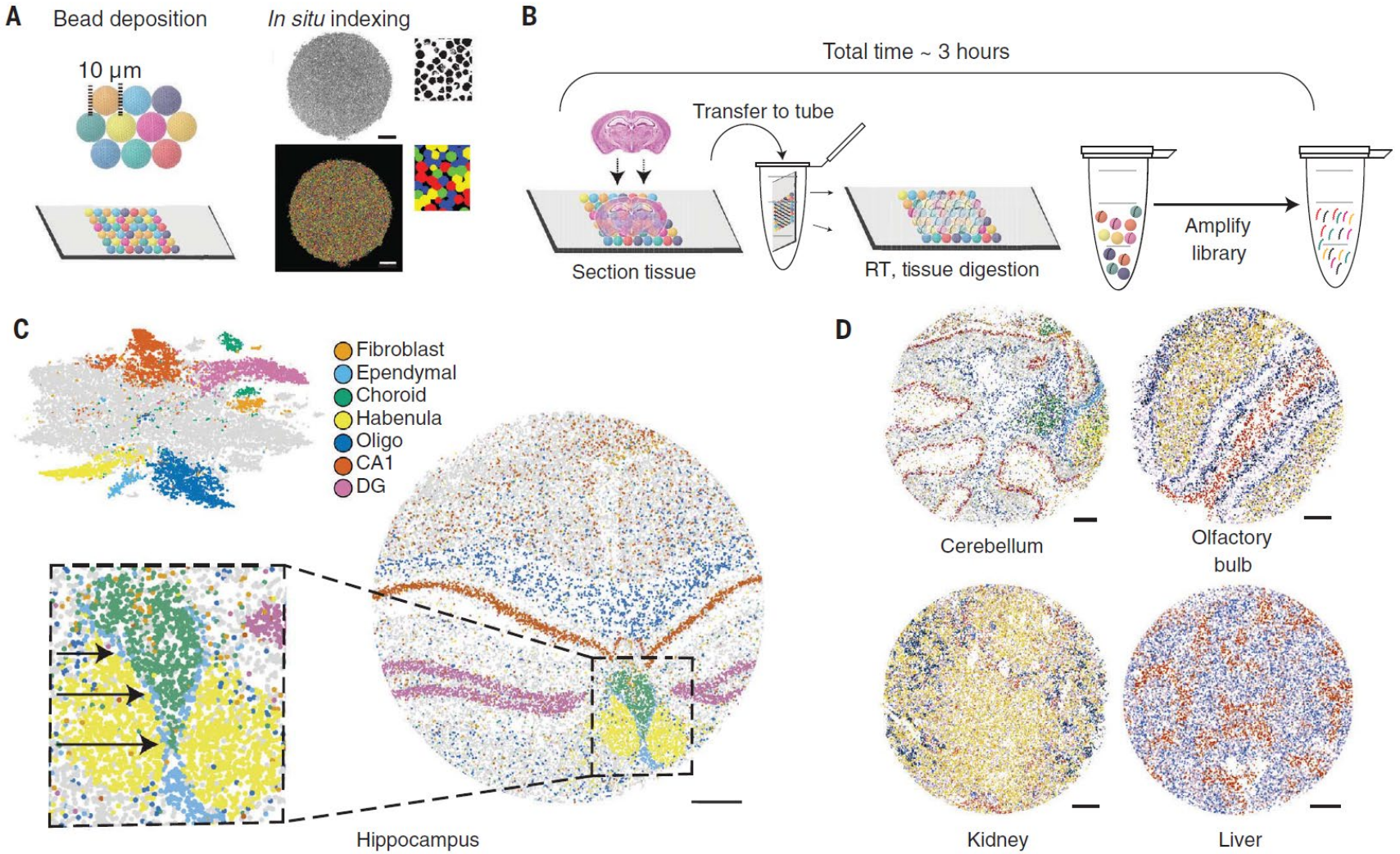

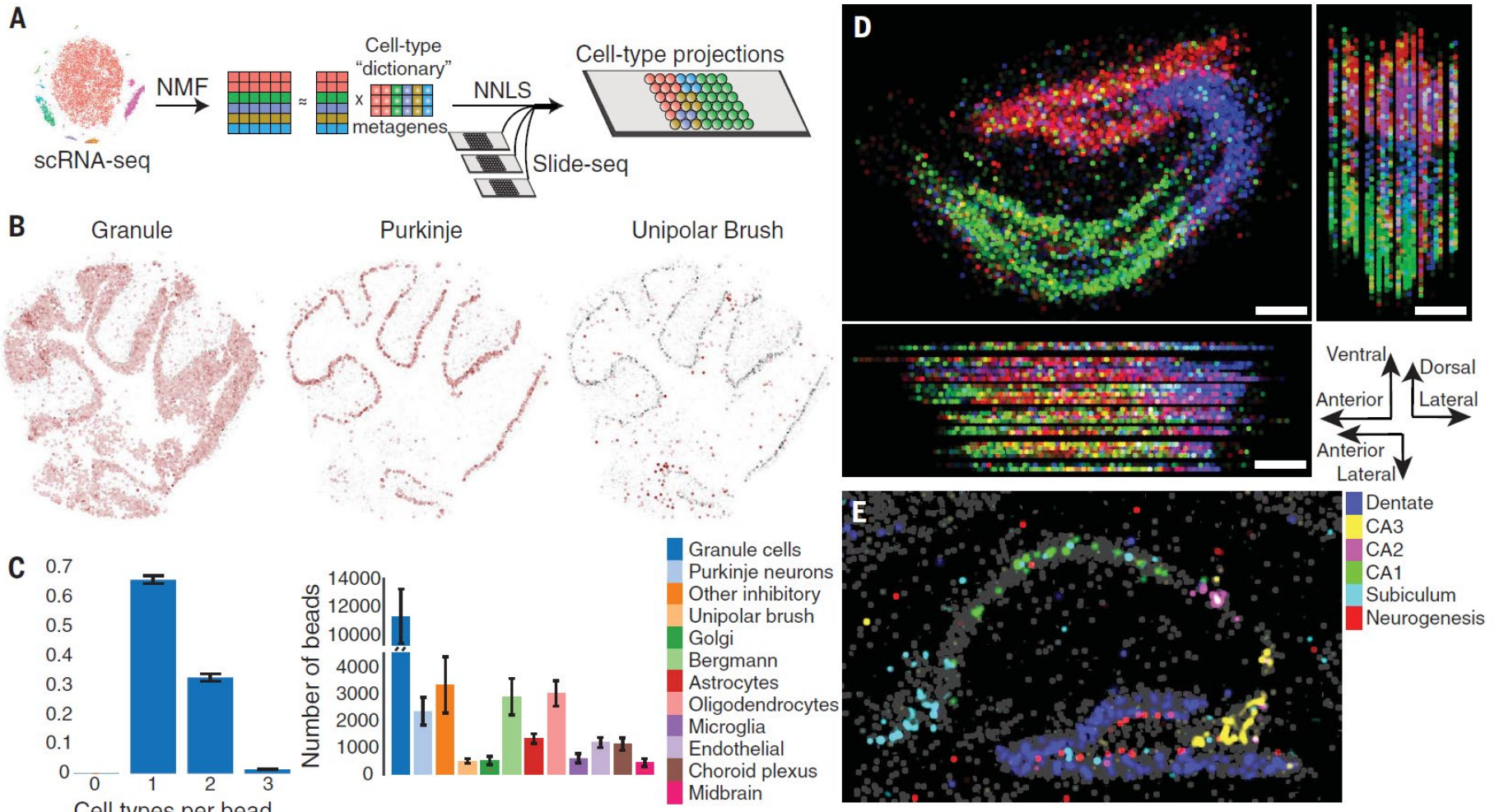
A
scRNA-seq
NMF
≈
x
Cell-type "dictionary"
metagenes
NNLS
Slide-seq
Cell-type projections
B
Granule
Purkinje
Unipolar Brush
C
Cell types per bead
Number of beads
Granule cells
Purkinje neurons
Other inhibitory
Unipolar brush
Golgi
Bergmann
Astrocytes
Oligodendrocytes
Microglia
Endothelial
Choroid plexus
Midbrain
D
Ventral
Dorsal
Anterior
Lateral
Anterior
Lateral
E
Dentate
CA3
CA2
CA1
Subiculum
Neurogenesis

Wrapp *et al.*, *Science* **367**, 1260–1263 (2020)

Cryo-EM structure of the 2019-nCoV spike in the prefusion conformation

Daniel Wrapp[1]*, Nianshuang Wang[1]*, Kizzmekia S. Corbett[2], Jory A. Goldsmith[1], Ching-Lin Hsieh[1], Olubukola Abiona[2], Barney S. Graham[2], Jason S. McLellan[1]†

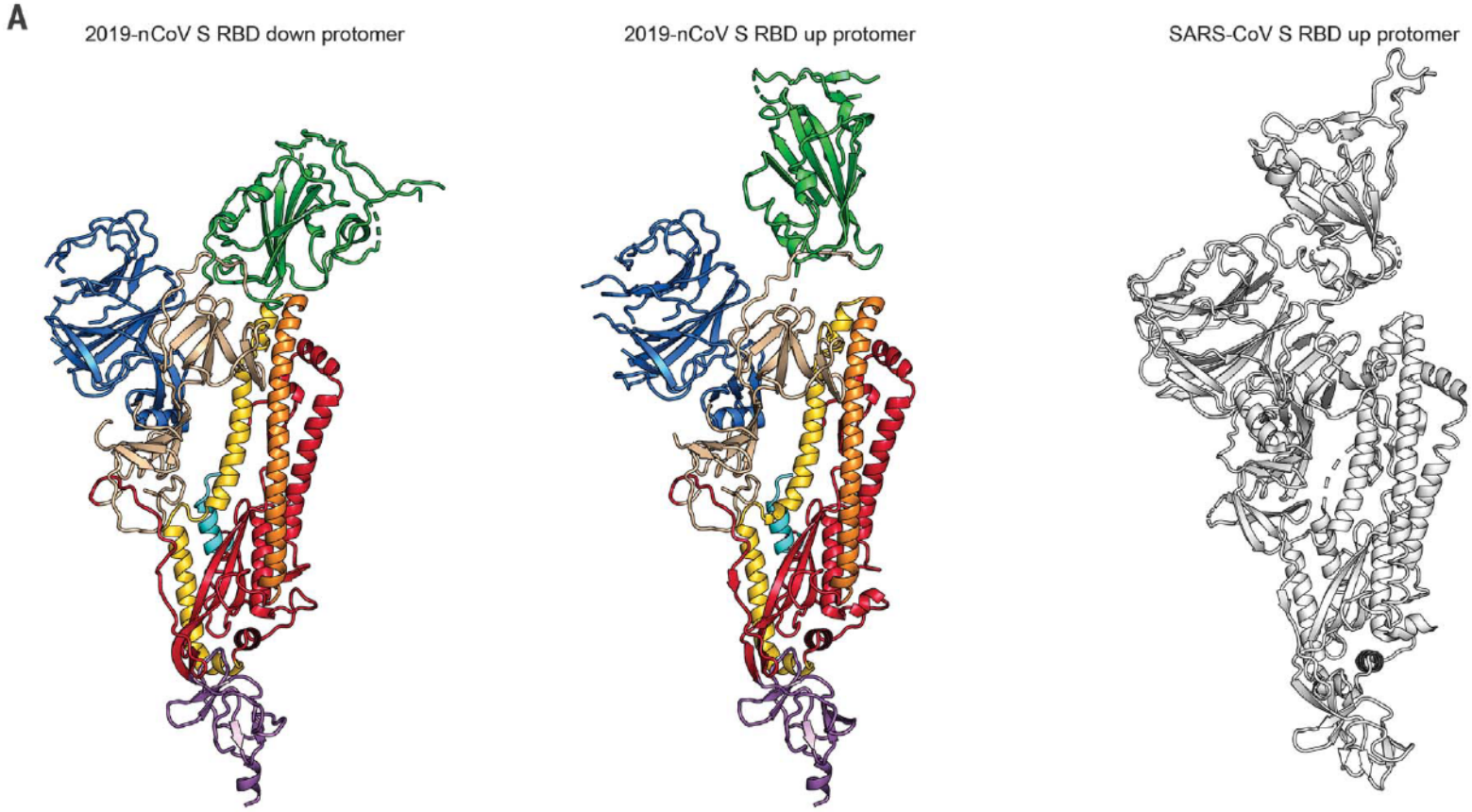

Molecular architecture of the inner ring scaffold of the human nuclear pore complex

15 APRIL 2016 • VOL 352 ISSUE 6283

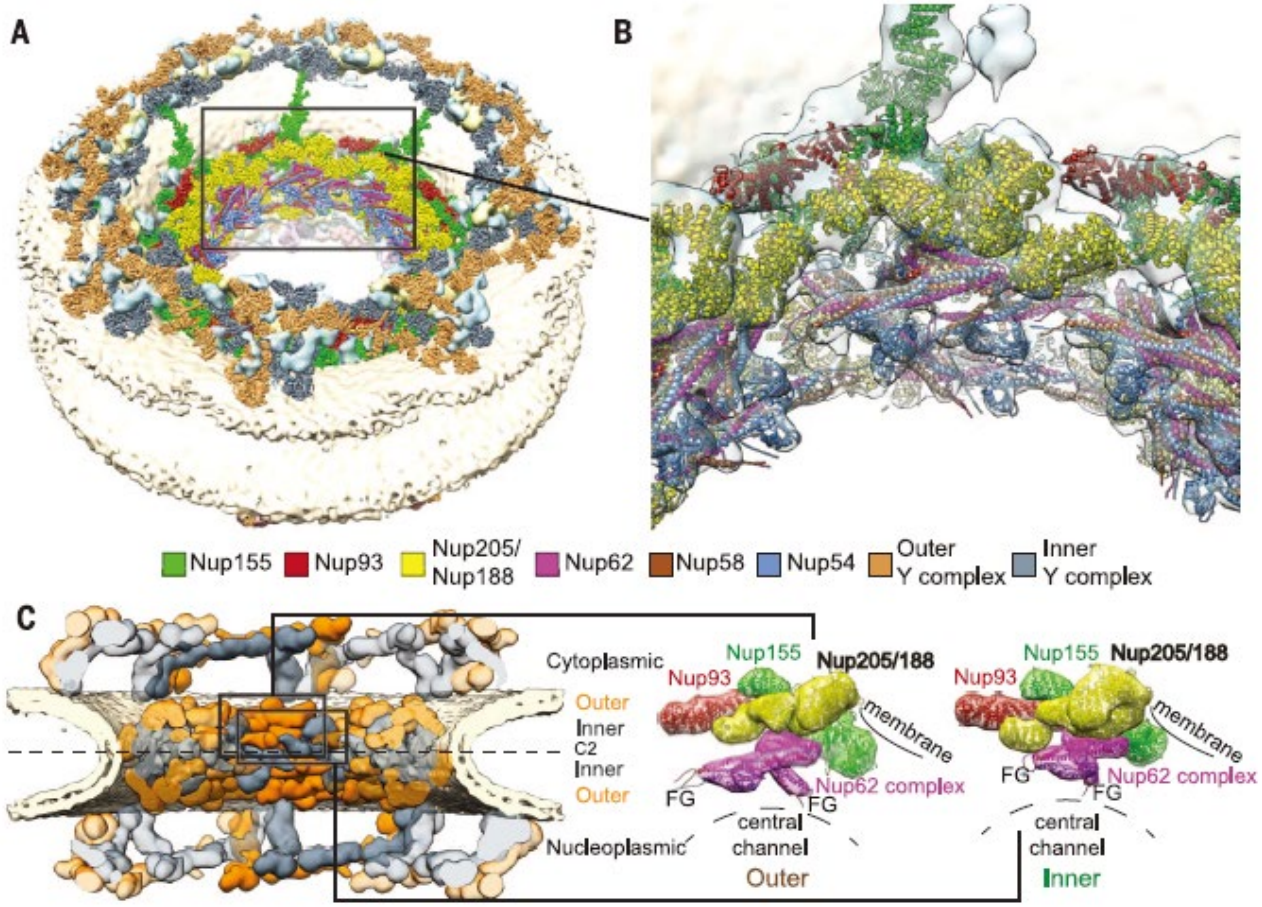

Fig. 1. Composite structure of the human NPC. (**A**) Overview of the composite structure of the entire NPC, in which previous structural assignments in the outer rings (*9*, *13*) are represented together with the assignments in the IR that were undertaken in this study (details are shown in fig. S2). Unassigned density is shown in cyan; the nuclear ring is facing up. (**B**) Zoomed-in view of the IR region framed in (A). High-resolution structures (colored ribbons) are shown in the context of the tomographic map (transparent isosurface). (**C**) Conceptual outline of the NPC architecture. Inner (gray) and outer (orange) copies of the Y complex (top and bottom) and the IR core module (middle) are shown in comparison. The configurations of the outer and inner copies of the IR core module are shown enlarged on the right. FG repeat domains can readily reach out into the central channel (F, phenylalanine; G, glycine).

Cryo-electron tomography: The challenge of doing structural biology in situ

Vladan Lučić, Alexander Rigort, and Wolfgang Baumeister

Max-Planck-Institute of Biochemistry, Am Klopferspitz 18, 82152 Martinsried, Germany

The Rockefeller University Press
J. Cell Biol. Vol. 202 No. 3 407–419
www.jcb.org/cgi/doi/10.1083/jcb.201304193

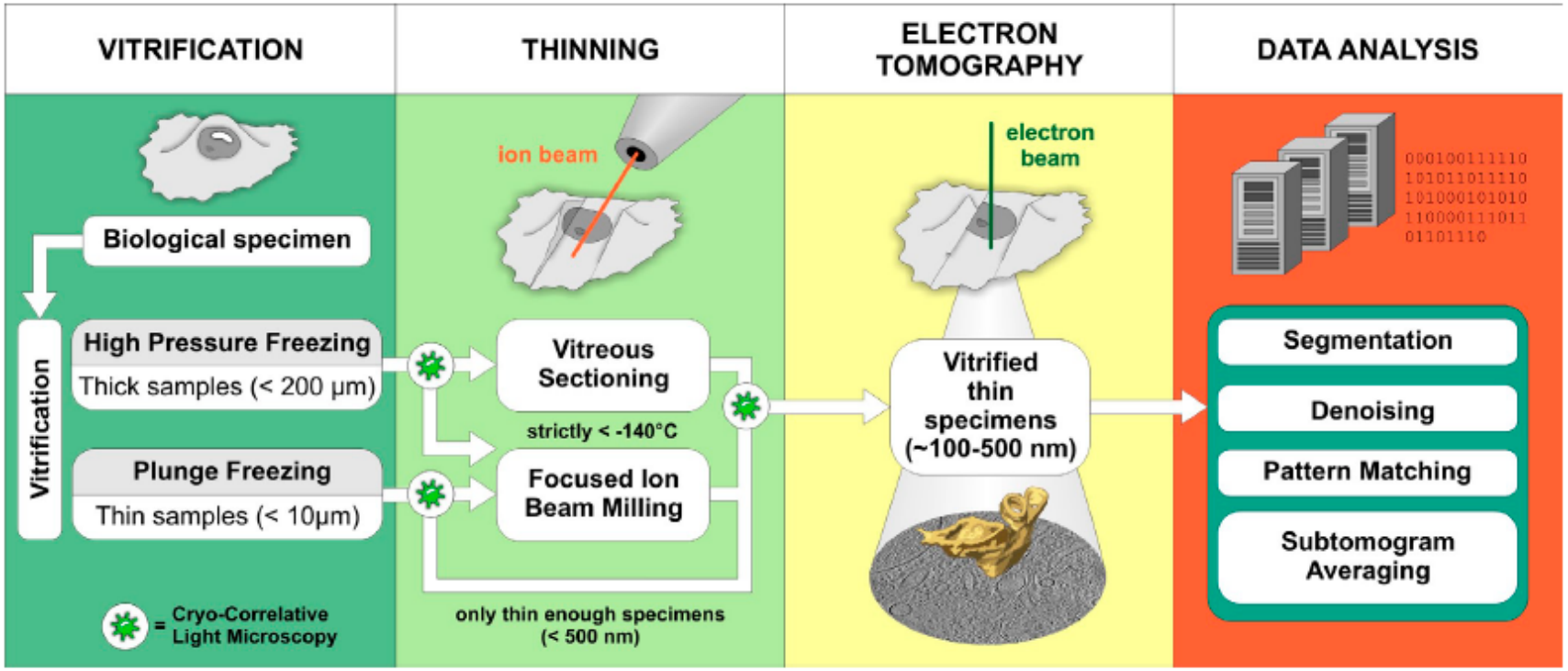

Box 1. Principles of electron tomography

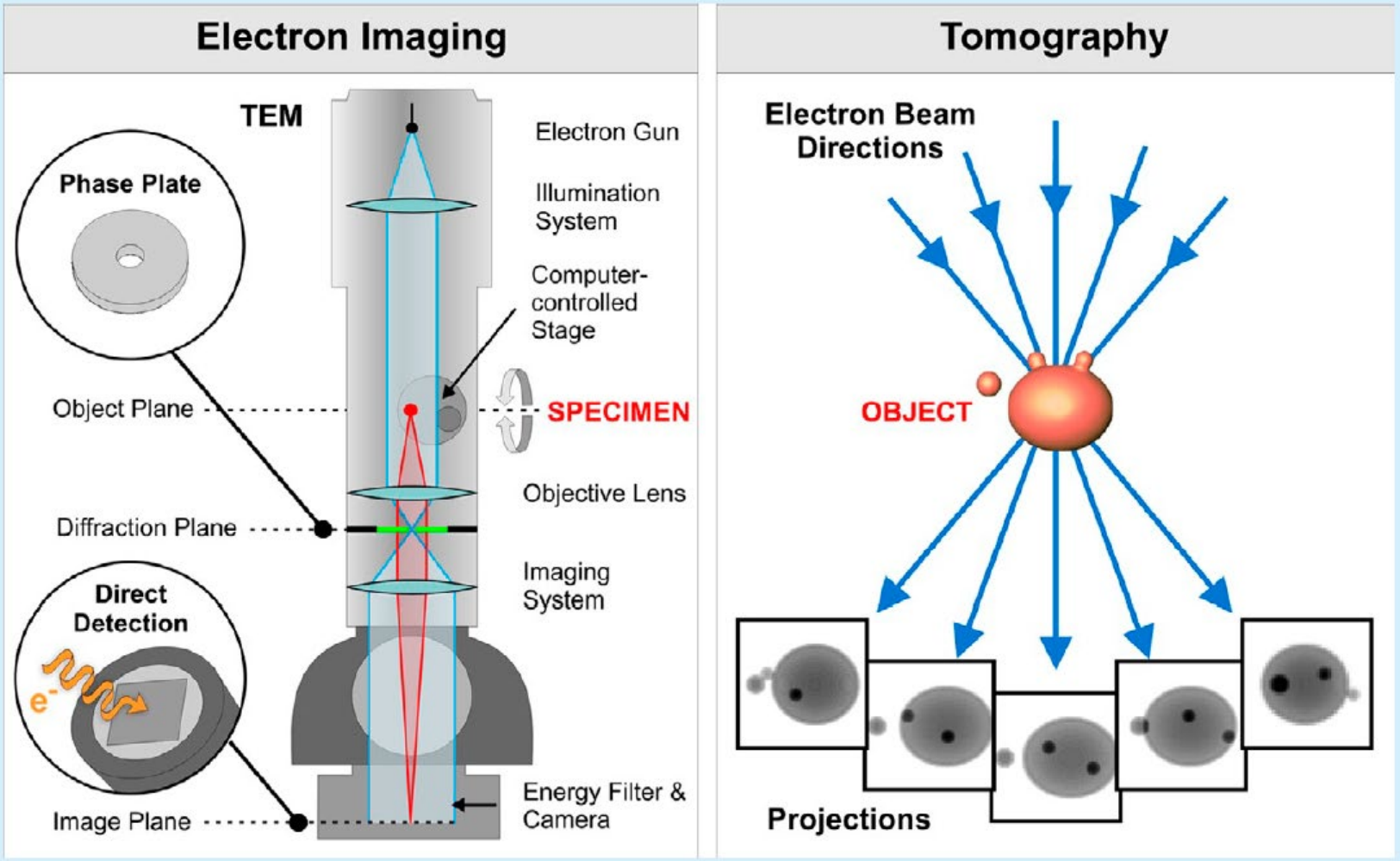

Box 2. Current technical developments

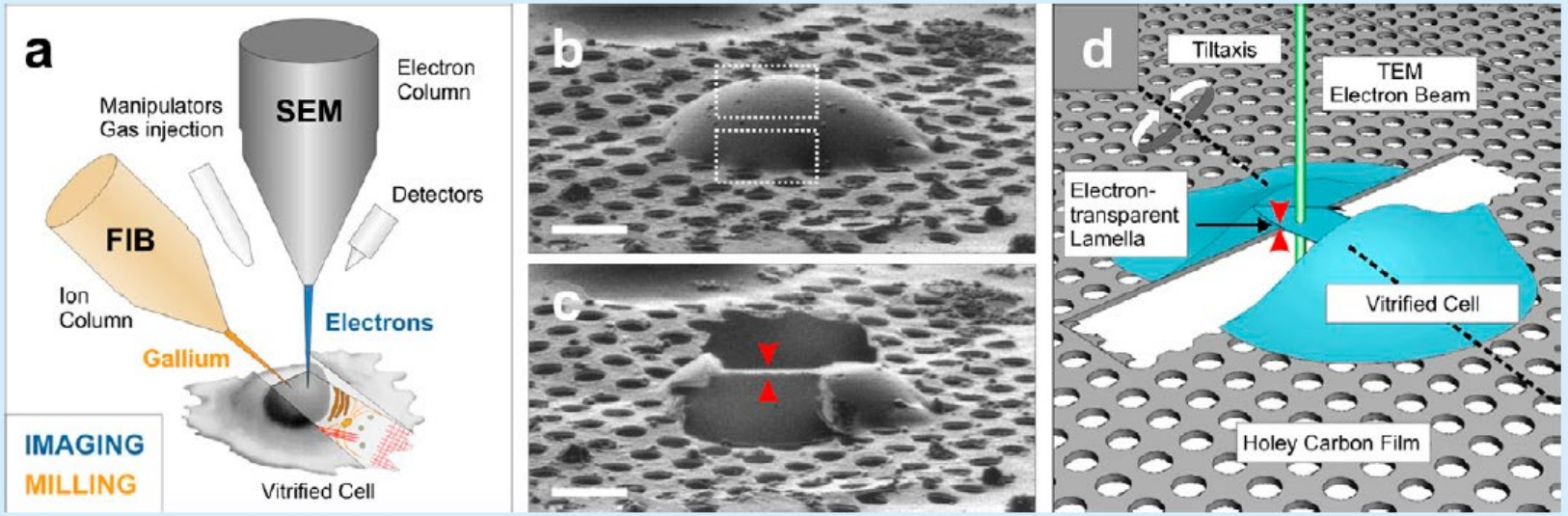

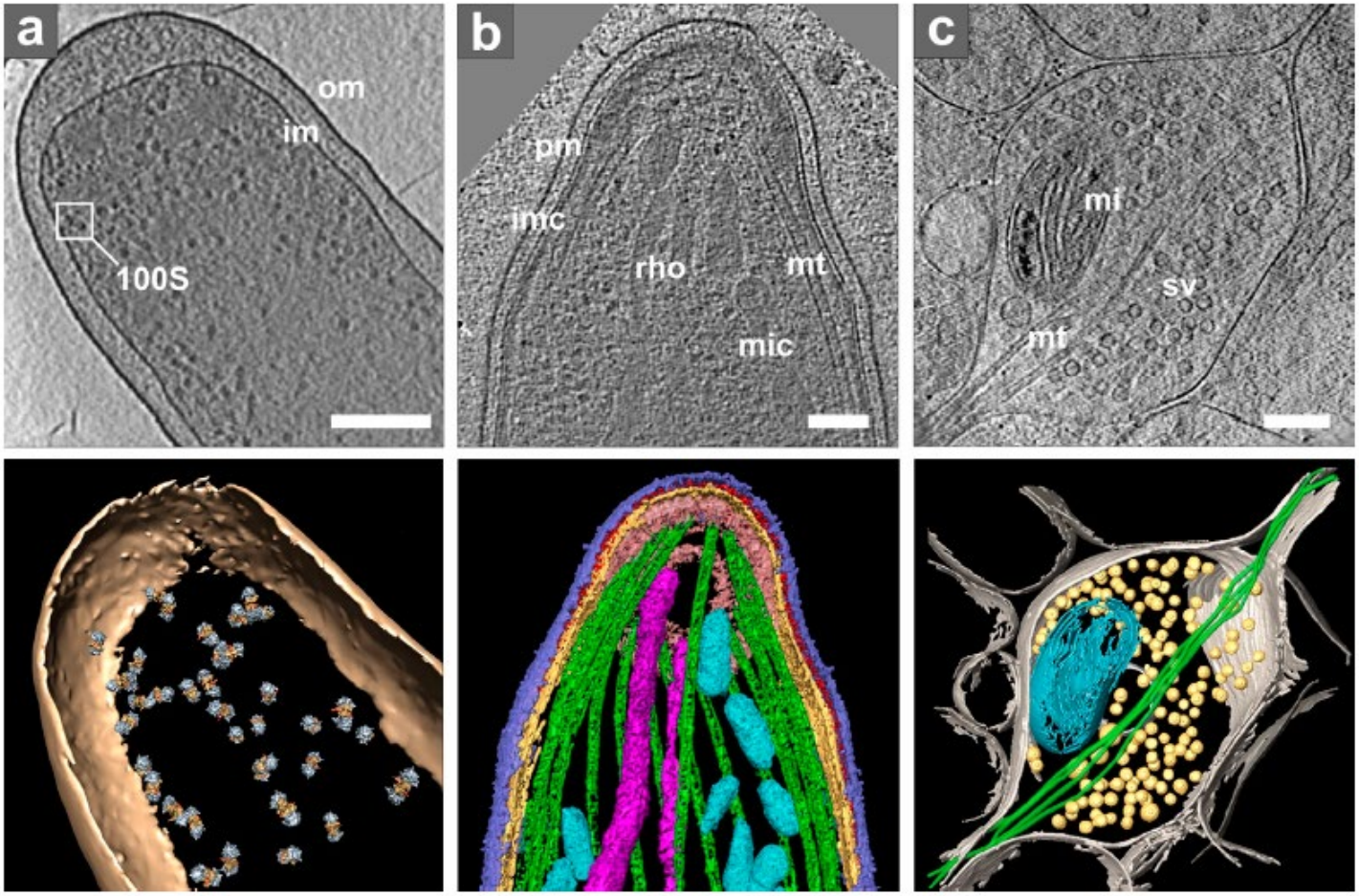

Figure 2. **Cryo-ET of intact cells.** (a) Intact *E. coli*. Top: tomographic slice. Bottom: isosurface representation with positions of template-matched ribosome pairs: om, outer membrane; im, inner membrane; inset shows one ribosome pair (100S). Bar, 200 nm. Modified from Ortiz et al. (2010). (b) *Plasmodium* organelles and the associated cytoskeleton. Top: tomographic slice. Bottom: surface rendering showing plasma membrane (pm, blue), inner membrane complex (imc, yellow), density between pm and imc (red), microtubules (mt, green), apical polar ring (pink), rhoptries (rho, violet), and micronemes (mic, cyan). Bar, 100 nm. Reproduced from Kudryashev et al. (2010b). (c) Presynaptic terminal visualized in vitrified dissociated neuronal culture at 15 days in vitro and thinned by FIB milling. Top: tomographic slice (courtesy of Y. Fukuda). Bottom: 3D visualization: plasma membrane (gray), microtubules (mt, green), mitochondrion (mi, cyan), and synaptic vesicles (sv, yellow). Bar, 200 nm.

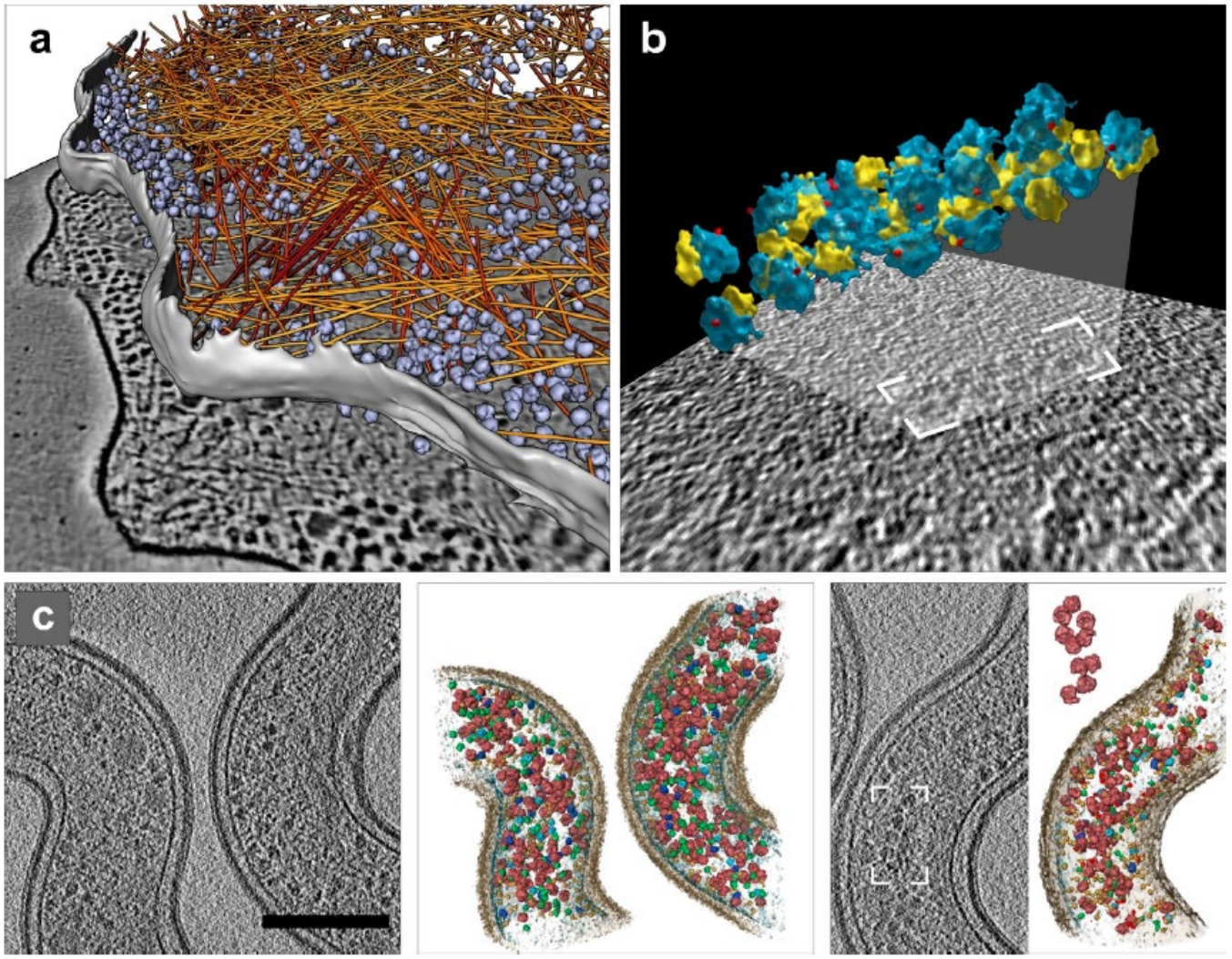

Figure 4. **Image processing: segmentation and template matching.** (a) Automated segmentation of actin filaments in *Dictyostelium discoideum*: actin filaments (yellow to red); ribosomes (blue). Reproduced with permission from Rigort et al. (2012b); copyright Elsevier, Inc. (b) Polyribosomes from intact human glioma cells identified by template matching. Modified with permission from Brandt et al. (2010); copyright Elsevier, Inc. (c) Protein identification using multiple template matching in intact *Leptospira interrogans*. Tomographic slices and 3D visualization of identified proteins of nonstimulated (left) and antibiotics-treated cells (right), ribosomes (red), GroEL (light blue), GroEL/ES (dark blue), and RNA polymerase II (green). Bar, 200 nm. Reprinted by permission from Macmillan Publishers Ltd: *Nature Methods* (Beck et al., 2009); copyright 2009.

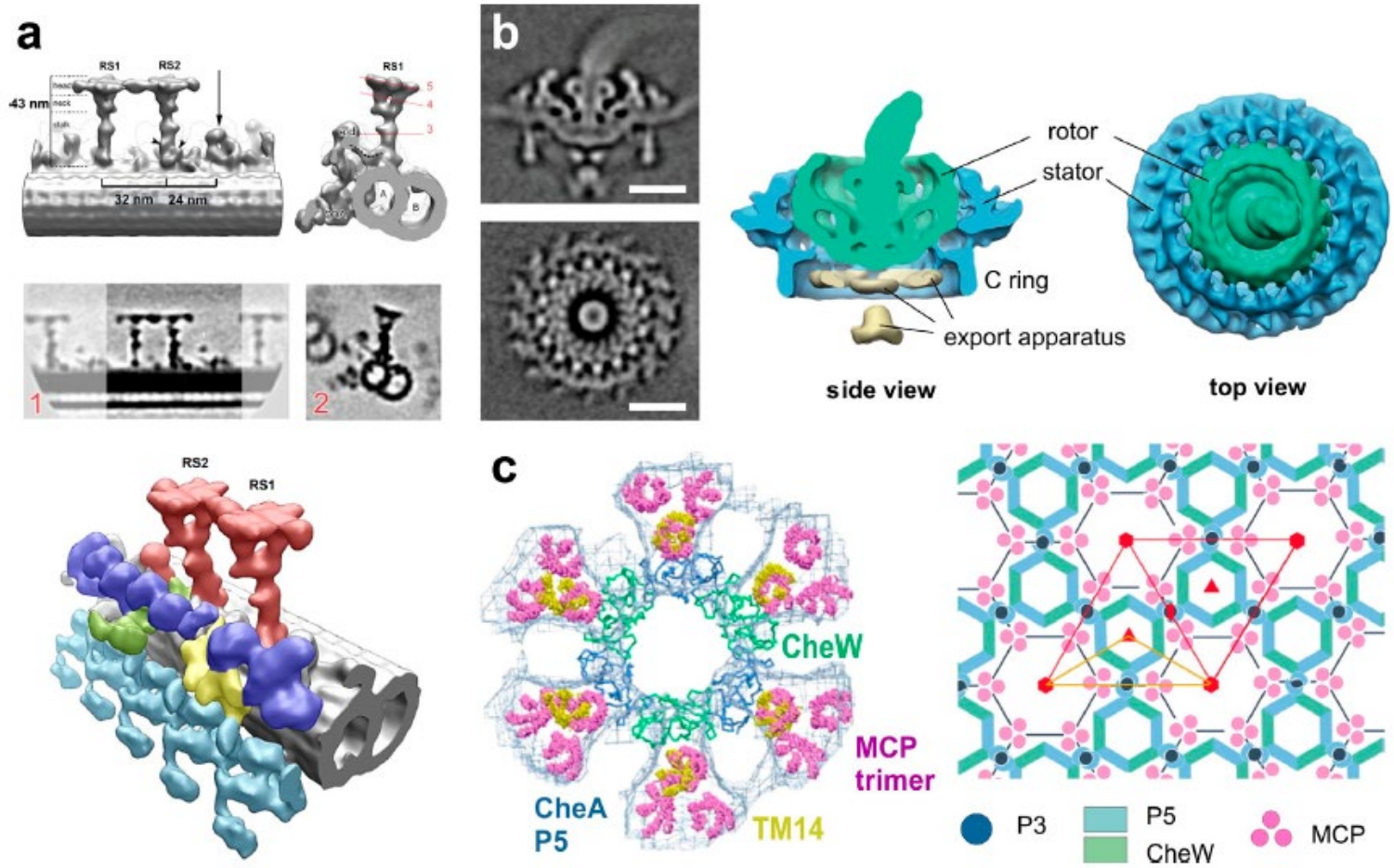

Figure 5. **Image processing: subtomogram averaging.** (a) Isolated *C. reinhardtii* axoneme. Top row: surface renderings of the density map obtained by averaging radial spokes (RS). Middle row: tomographic slices of the above density map. Bottom: surface renderings of the overall 3D structure: microtubule doublet (gray), outer dynein arms (turquoise), inner dynein arms (IDA, blue), the intermediate and light chains of IDAs (yellow), the dynein regulatory complex (green), and the radial spokes (red). RS1, radial spoke 1; RS2, radial spoke 2. Image copyright Pigino et al. (2011). (b) Flagellar motor of intact *Borrelia*. Left: tomographic slices of the averaged density map. Right: 3D isosurface views of the motor. Bars, 25 nm. Reproduced from Liu et al. (2009) with permission from the American Society for Microbiology. (c) Bacterial chemosensory receptors. Left: superposition of one ring of the crystal structure (P5 blue, CheW green) with its six receptor dimers (TM14, yellow) on the EM map (blue mesh) with its previously fit 18 receptor dimers (pink). Right: the arrangement of the receptor array produces P6 point symmetry (red; the asymmetric unit yellow). Image copyright Briegel et al. (2012).

Composition of isolated synaptic boutons reveals the amounts of vesicle trafficking proteins

30 MAY 2014 • VOL 344 ISSUE 6187

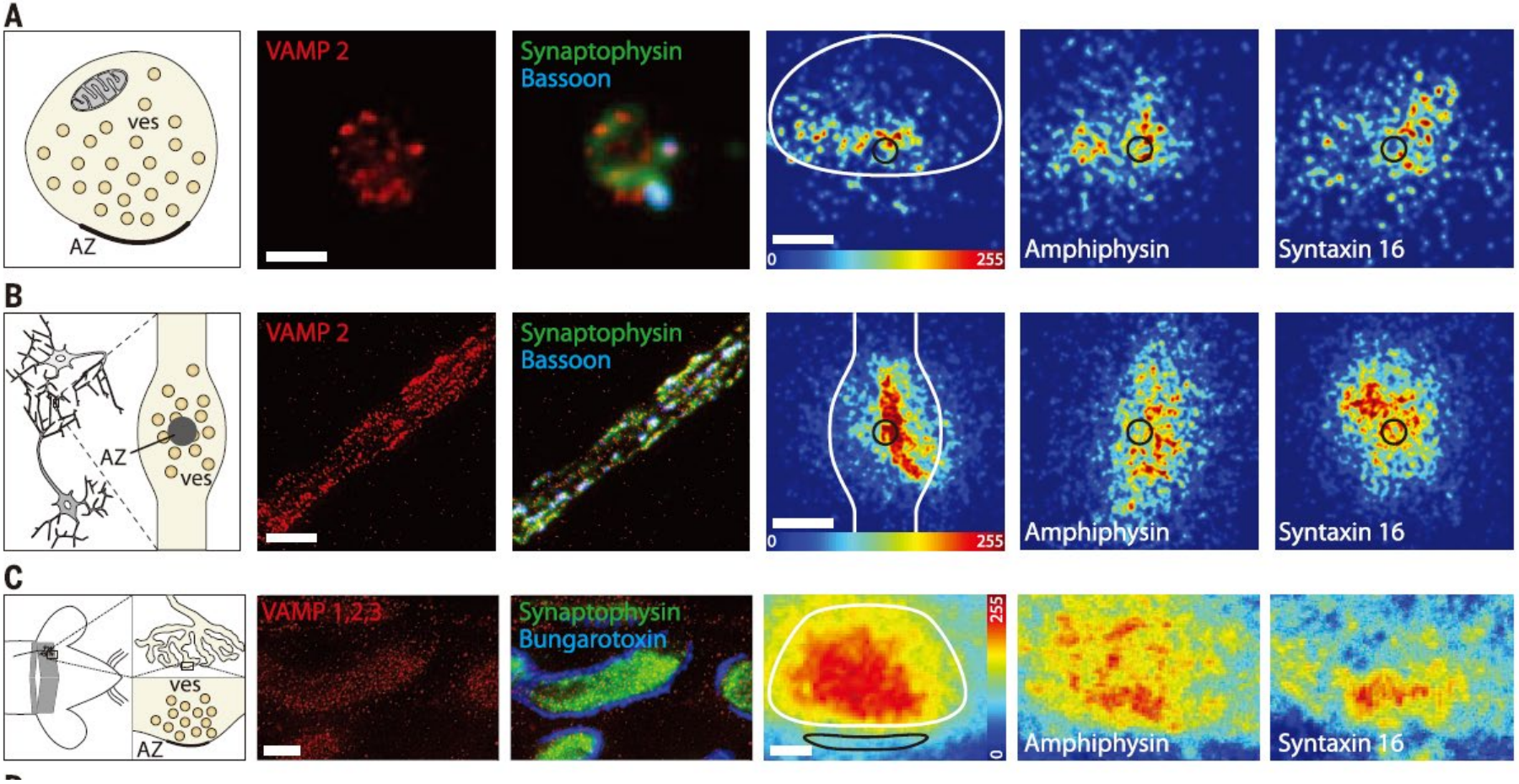

Synaptic vesicle recycling has long served as a model for the general mechanisms of cellular trafficking. We used an integrative approach, combining quantitative immunoblotting and mass spectrometry to determine protein numbers; electron microscopy to measure organelle numbers, sizes, and positions; and super-resolution fluorescence microscopy to localize the proteins. Using these data, we generated a three-dimensional model of an "average" synapse, displaying 300,000 proteins in atomic detail. The copy numbers of proteins involved in the same step of synaptic vesicle recycling correlated closely. In contrast, copy numbers varied over more than three orders of magnitude between steps, from about 150 copies for the endosomal fusion proteins to more than 20,000 for the exocytotic ones.

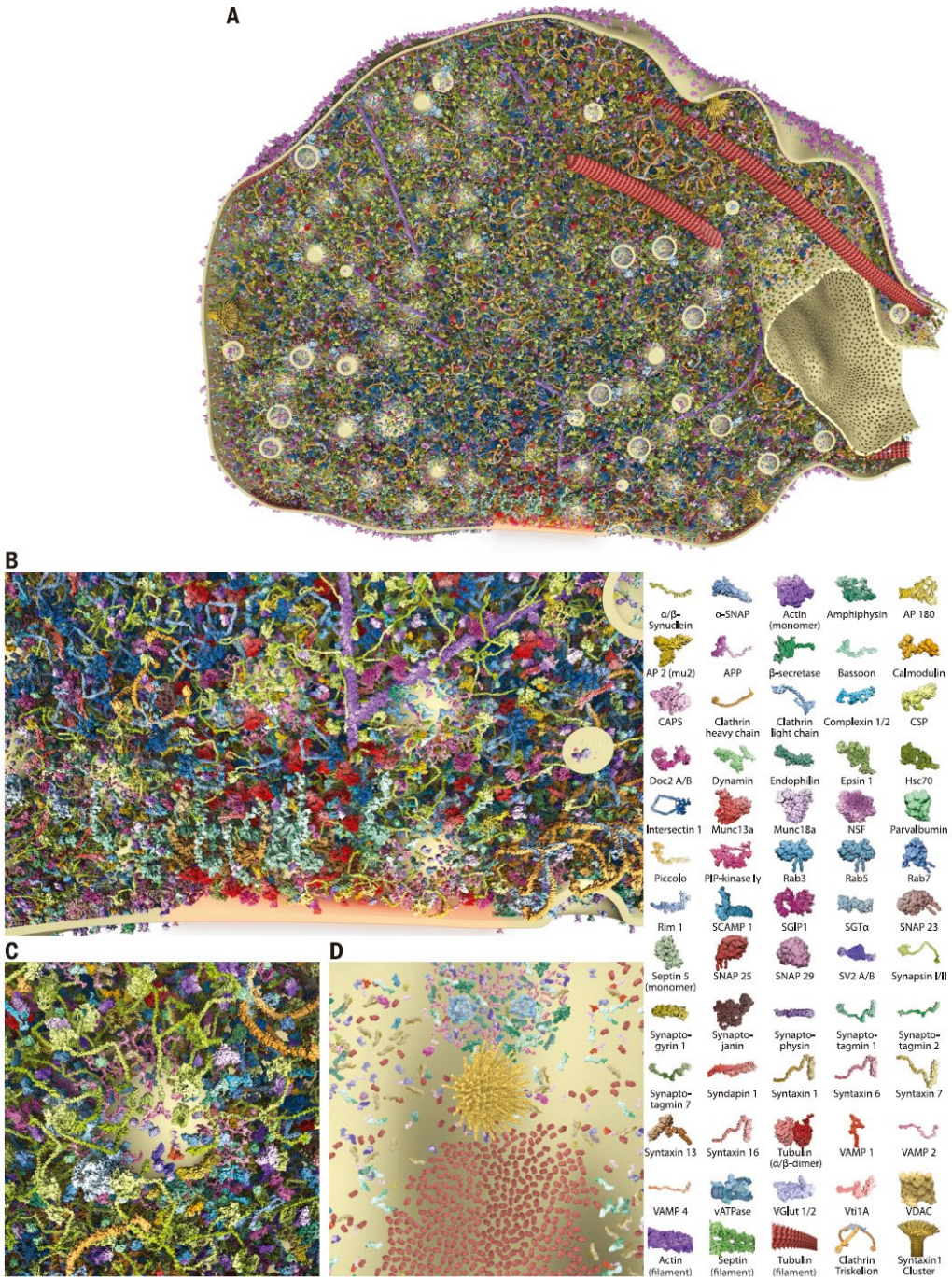
A
B
C
D
α/β-Synuclein
α-SNAP
Actin (monomer)
Amphiphysin
AP 180
AP 2 (mu2)
APP
β-secretase
Bassoon
Calmodulin
CAPS
Clathrin heavy chain
Clathrin light chain
Complexin 1/2
CSP
Doc2 A/B
Dynamin
Endophilin
Epsin 1
Hsc70
Intersectin 1
Munc13a
Munc18a
NSF
Parvalbumin
Piccolo
PIP-kinase Iγ
Rab3
Rab5
Rab7
Rim 1
SCAMP 1
SGIP1
SGTα
SNAP 23
Septin 5 (monomer)
SNAP 25
SNAP 29
SV2 A/B
Synapsin I/II
Synapto-gyrin 1
Synapto-janin
Synapto-physin
Synapto-tagmin 1
Synapto-tagmin 2
Synapto-tagmin 7
Syndapin 1
Syntaxin 1
Syntaxin 6
Syntaxin 7
Syntaxin 13
Syntaxin 16
Tubulin (α/β-dimer)
VAMP 1
VAMP 2
VAMP 4
vATPase
VGlut 1/2
Vti1A
VDAC
Actin (filament)
Septin (filament)
Tubulin (filament)
Clathrin Triskelion
Syntaxin1 Cluster

SCIENTIFIC REPORTS

OPEN

Received: 8 August 2017
Accepted: 18 October 2017
Published online: 02 November 2017

3D MALDI Mass Spectrometry Imaging of a Single Cell: Spatial Mapping of Lipids in the Embryonic Development of Zebrafish

Maria Emilia Dueñas[1], Jeffrey J. Essner[3] & Young Jin Lee[1,2]

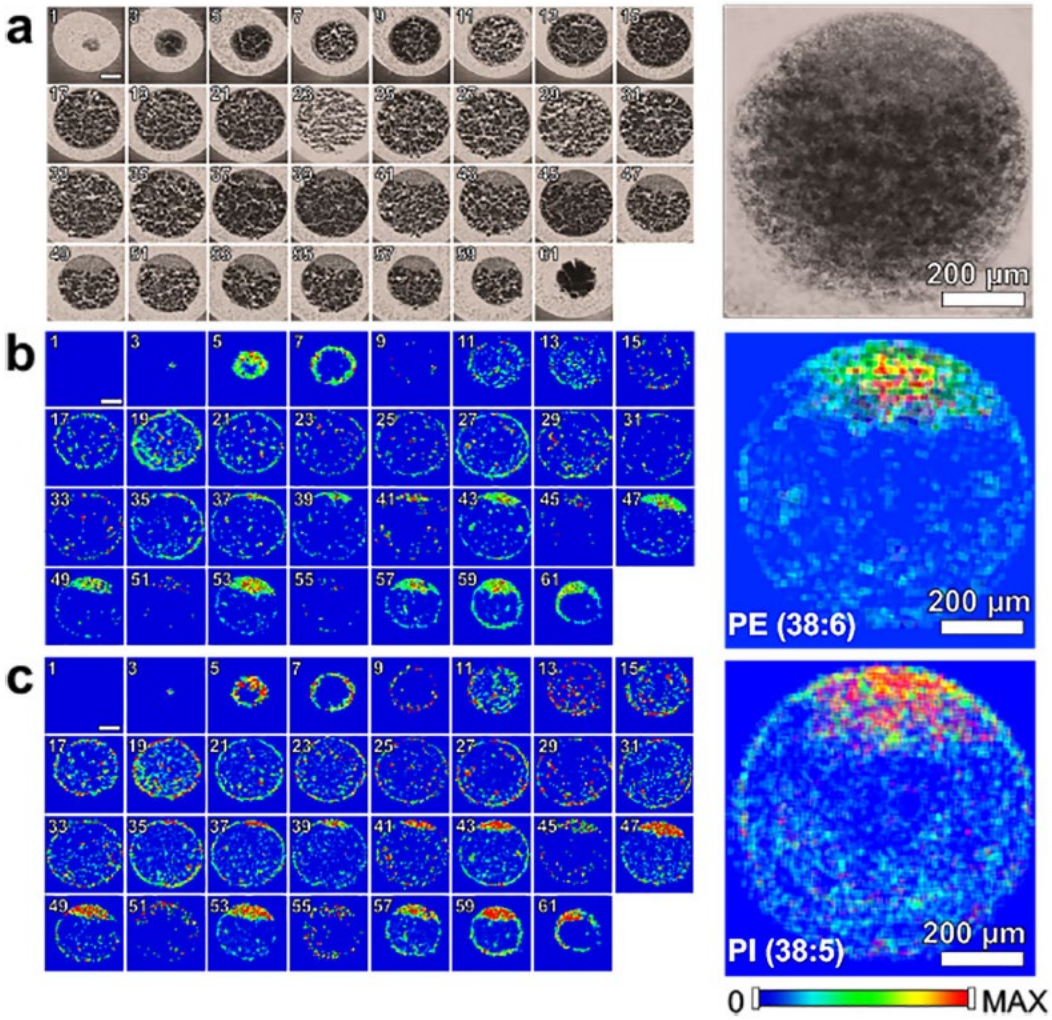

Organoids and Tumor Spheroids

An organoid is a 3D cellular structure that mimics the organization and function of an organ or specific tissue type in the body. Organoids are typically derived from pluripotent stem cells (such as embryonic stem cells or induced pluripotent stem cells) or organ-specific adult stem cells. These cells are grown in a 3D culture environment that provides the necessary extracellular matrix components, signaling molecules, and growth factors to promote cellular differentiation, self-organization, and tissue development. Organoids can recapitulate many of the key aspects of organ architecture, cellular composition, and function.

A tumor spheroid is a three-dimensional (3D) multicellular structure composed of cancer cells that closely mimic the organization and microenvironment of a tumor in the body. Tumor spheroids are formed by culturing cancer cells in a 3D culture system, allowing the cells to aggregate, proliferate, and form complex, spherical structures. These spheroids can recapitulate key features of solid tumors, such as cell-cell and cell-matrix interactions, nutrient and oxygen gradients, and the development of a necrotic core.

Tumor spheroids are distinct from organoids in several ways:

Cellular composition: Tumor spheroids are primarily composed of cancer cells, while organoids are derived from stem cells and contain multiple differentiated cell types that resemble a specific organ or tissue.

Structural organization: Tumor spheroids typically form relatively simple, spherical structures, whereas organoids often display more complex, organ-like architecture, including the formation of distinct tissue layers, compartments, and functional units.

Functionality: Organoids aim to recapitulate the function and organization of a specific organ or tissue, while tumor spheroids focus on modeling the characteristics of solid tumors, such as tumor growth, invasion, and drug resistance.

Research applications: Tumor spheroids are primarily used to study cancer biology, tumor microenvironment, and drug response, while organoids have broader applications, including disease modeling, drug discovery, developmental biology, personalized medicine, and regenerative medicine.

Organogenesis in a dish: Modeling development and disease using organoid technologies

Madeline A. Lancaster *and* J

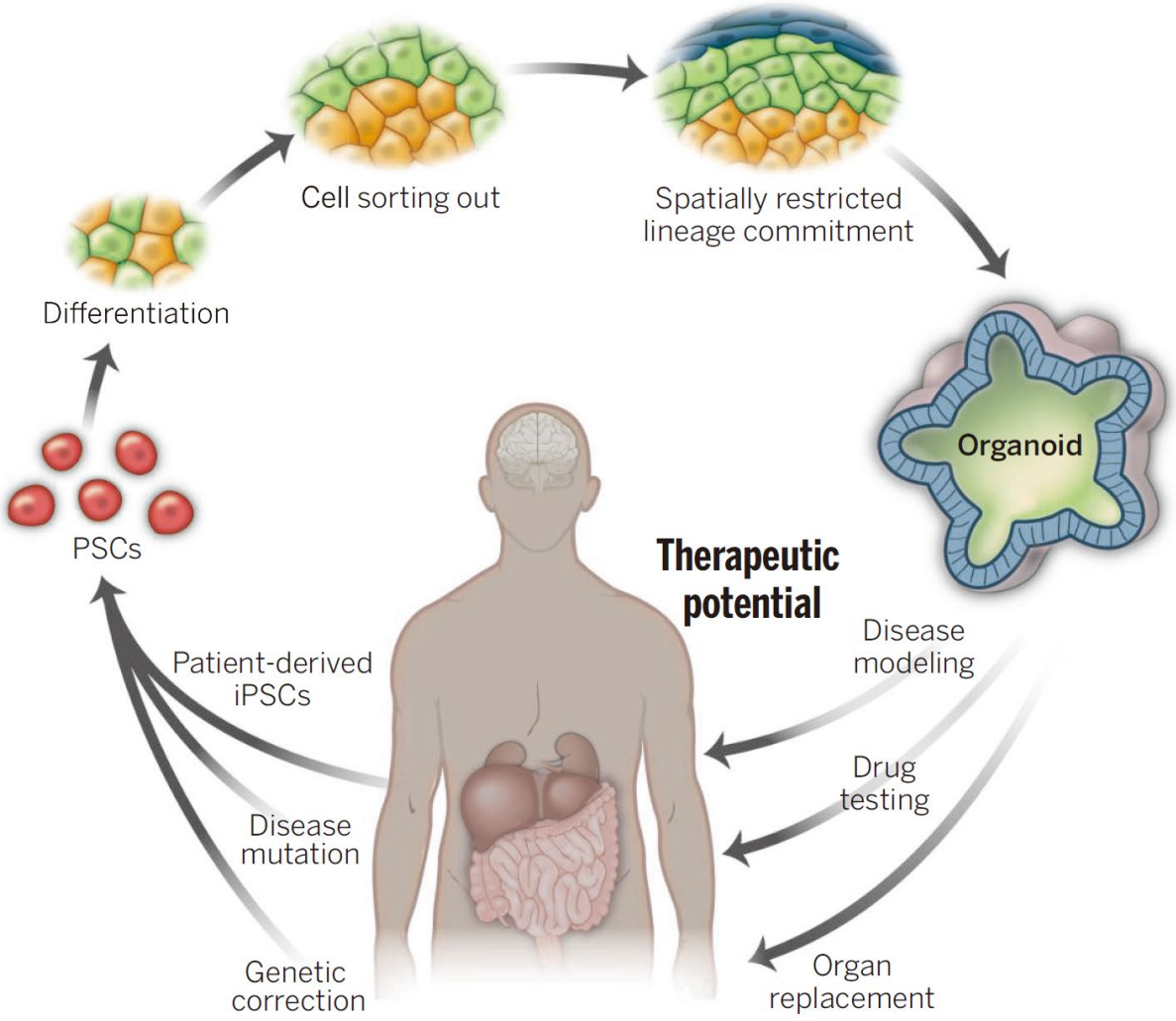

Organoid generation and therapeutic potential. Organoids can be derived for a number of organs from human pluripotent stem cells (PSCs). Like organogenesis in vivo, organoids

SUTLIFF/SCIENCE

Box 1. Defining organoids.

Organoid *n.* Resembling an organ.

This implies:

1. Multiple organ-specific cell types
2. Capable of recapitulating some specific function of the organ (eg. excretion, filtration, neural activity, contraction)
3. Grouped together and spatially organized similar to an organ

Organoid formation recapitulates both major processes of self-organization during development: cell sorting out and spatially restricted lineage commitment

Definition:
A collection of organ-specific cell types that develops from stem cells or organ progenitors and self-organizes through cell sorting and spatially restricted lineage commitment in a manner similar to *in vivo.*

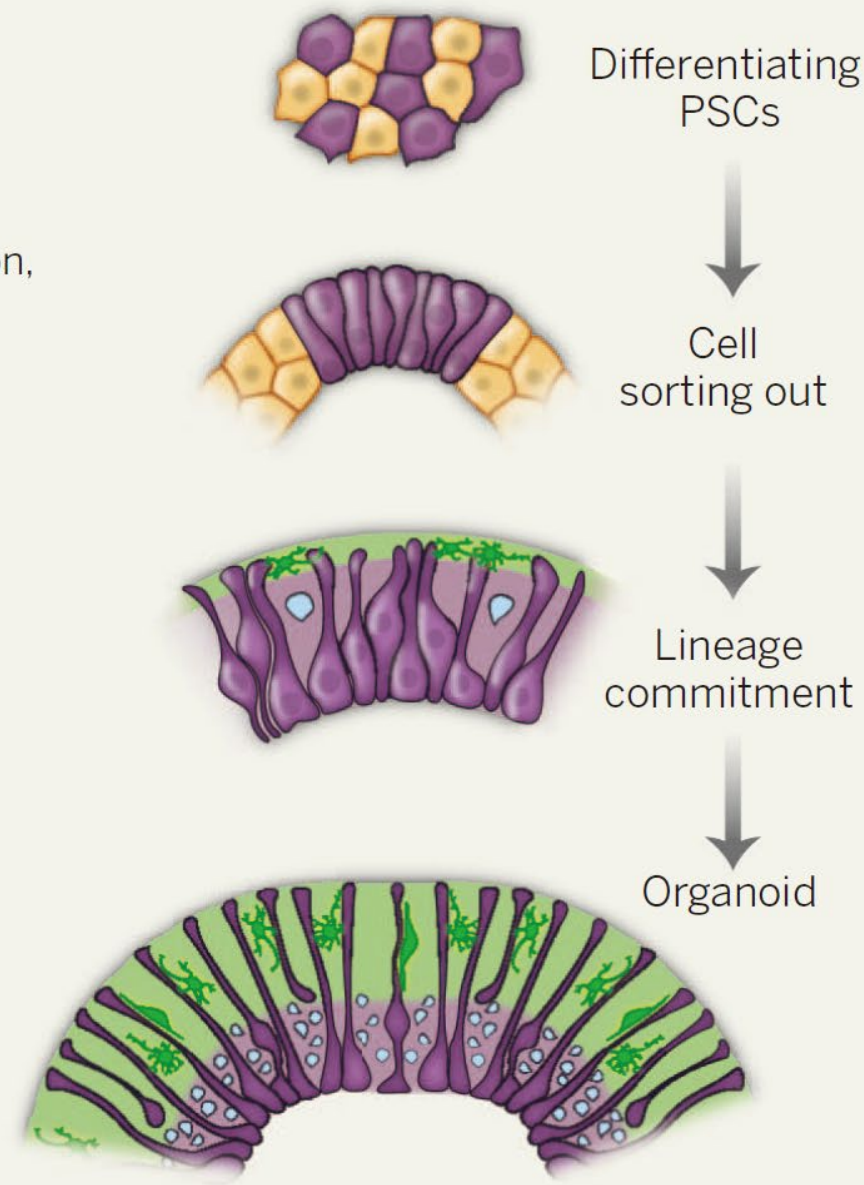

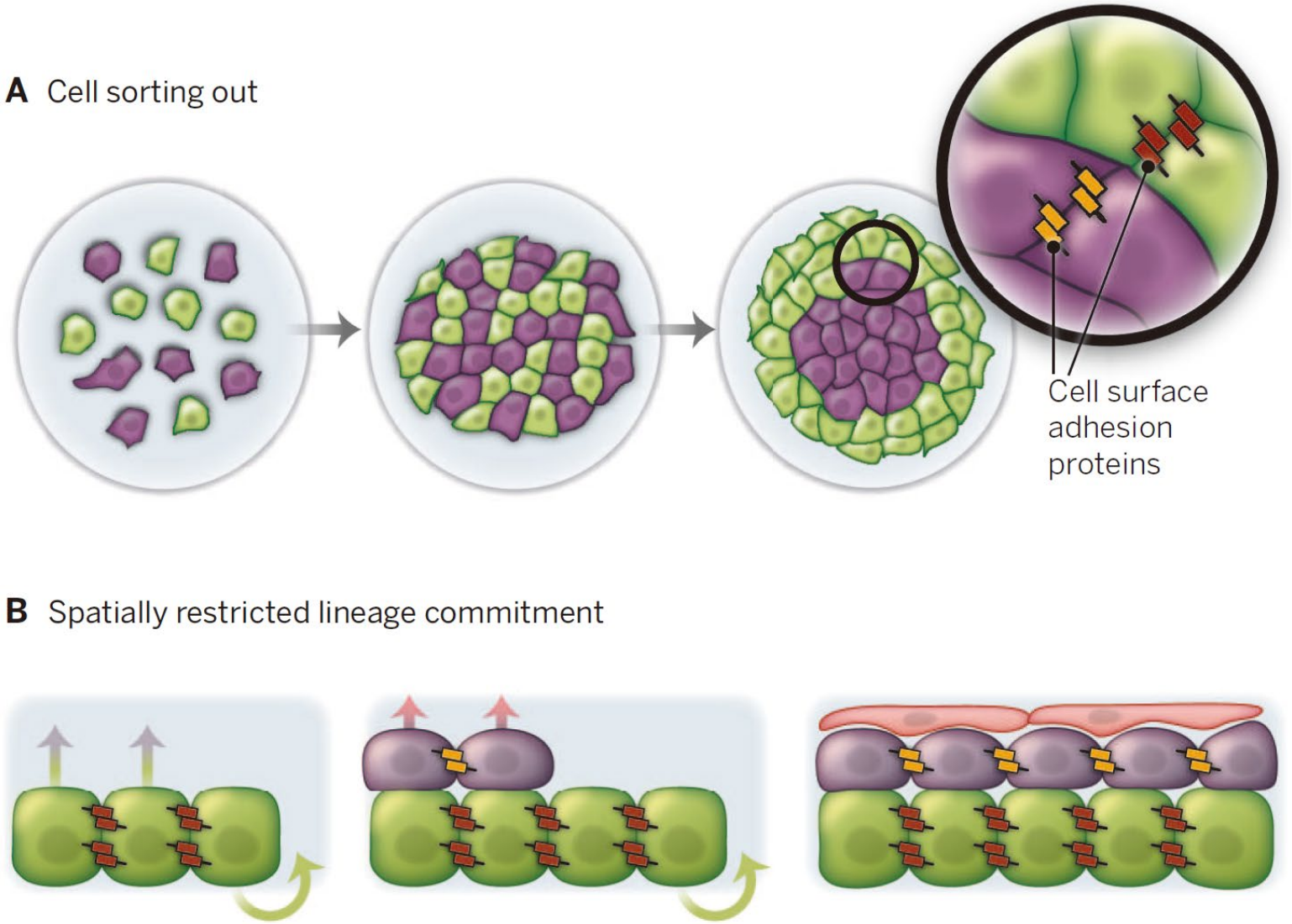

Fig. 2. Principles of self-organization. (**A**) Cell sorting out describes the movement of cells into different domains. Different cell types (purple or green) sort themselves because of different adhesive properties conferred by their differential expression of distinct cell adhesion molecules (shown as brown or orange bars). (**B**) Spatially restricted cell-fate decisions also contribute to self-organization in vivo and in organoids. Progenitors (green) give rise to more differentiated progeny (purple), which, because of spatial constraints of the tissue and/or division orientation, are forced into a more superficial position

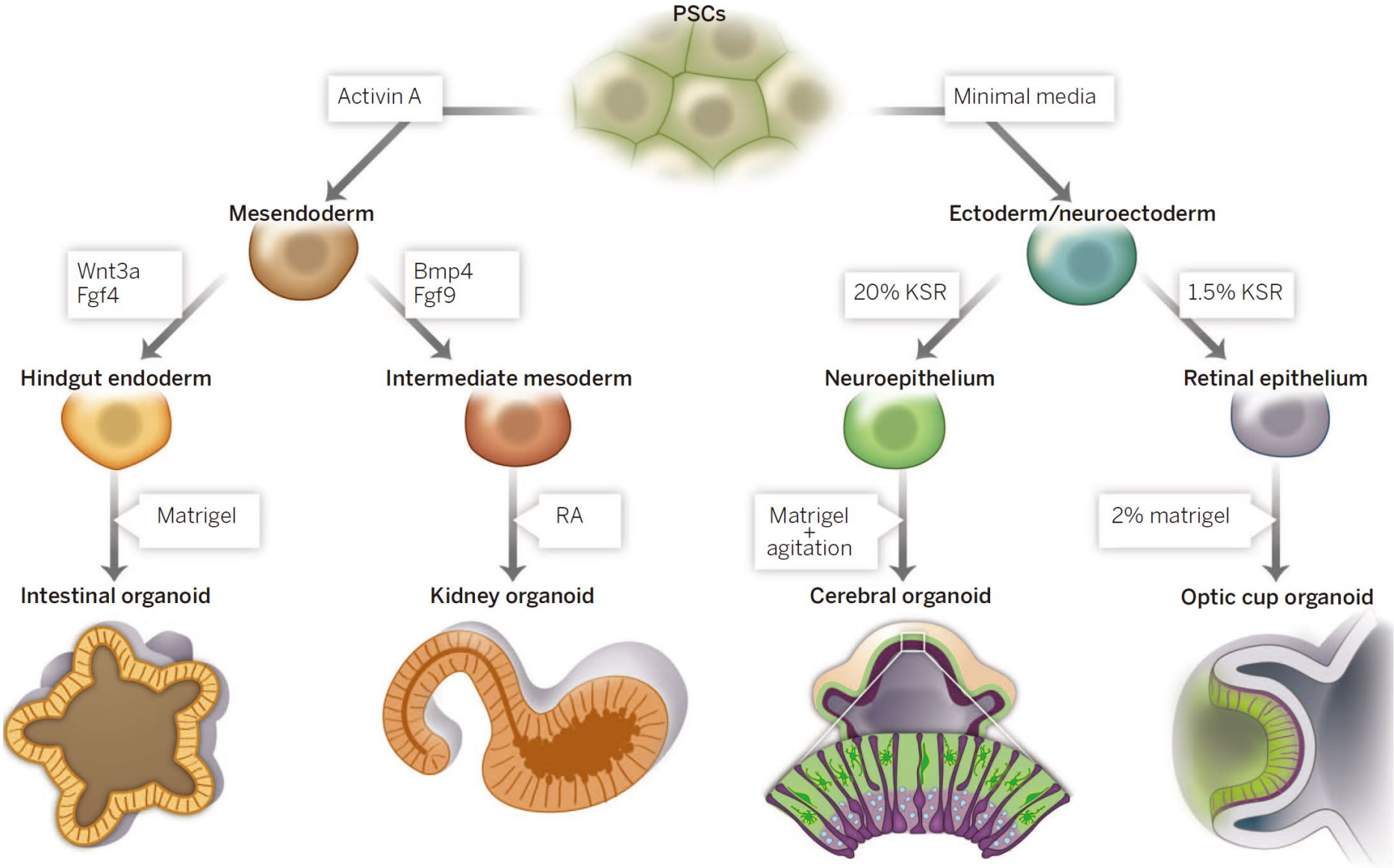
PSCs
Activin A
Minimal media
Mesendoderm
Ectoderm/neuroectoderm
Wnt3a
Fgf4
Bmp4
Fgf9
20% KSR
1.5% KSR
Hindgut endoderm
Intermediate mesoderm
Neuroepithelium
Retinal epithelium
Matrigel
RA
Matrigel
+
agitation
2% matrigel
Intestinal organoid
Kidney organoid
Cerebral organoid
Optic cup organoid

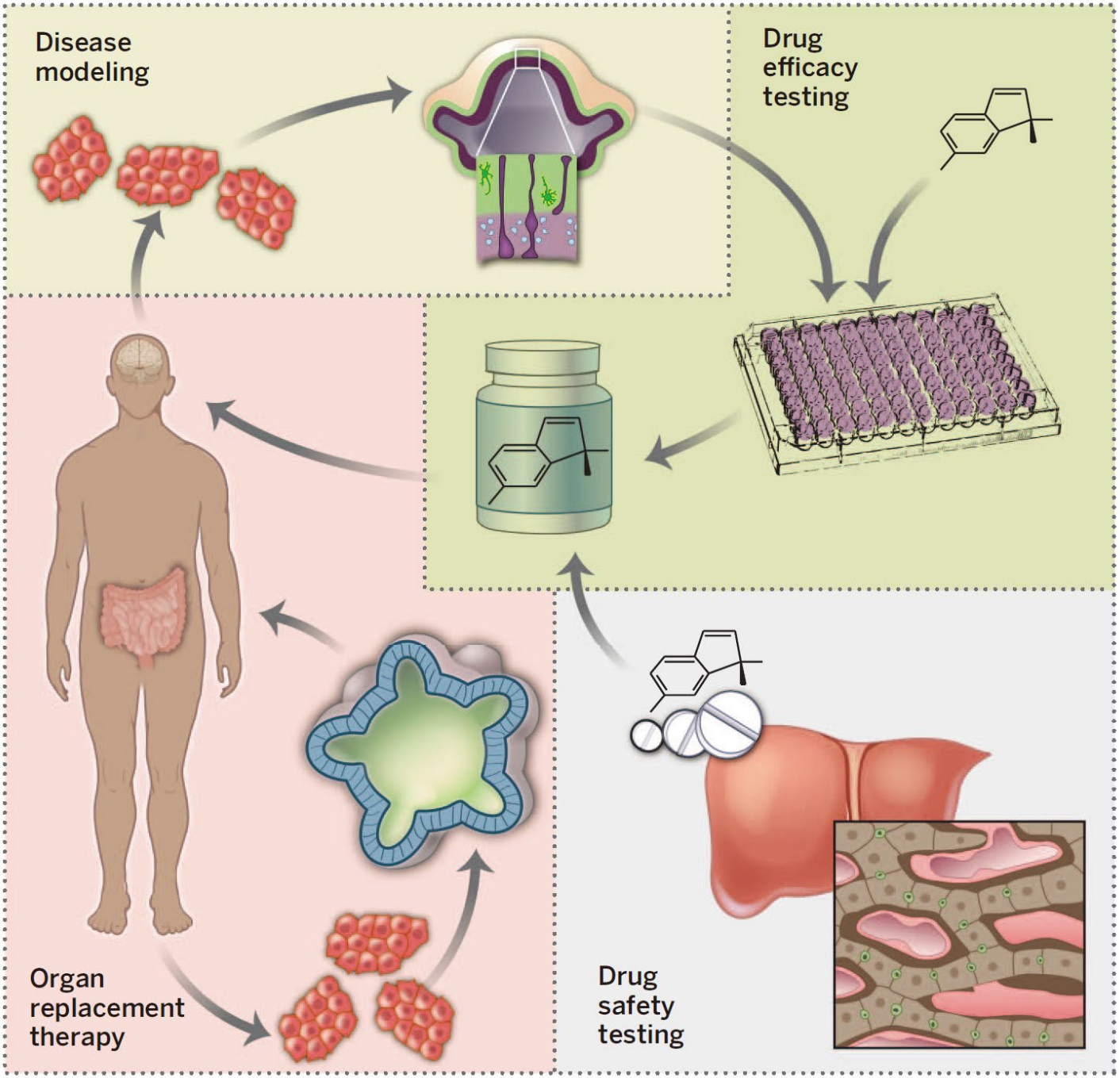
Disease modeling
Drug efficacy testing
Organ replacement therapy
Drug safety testing

Modeling Development and Disease with Organoids

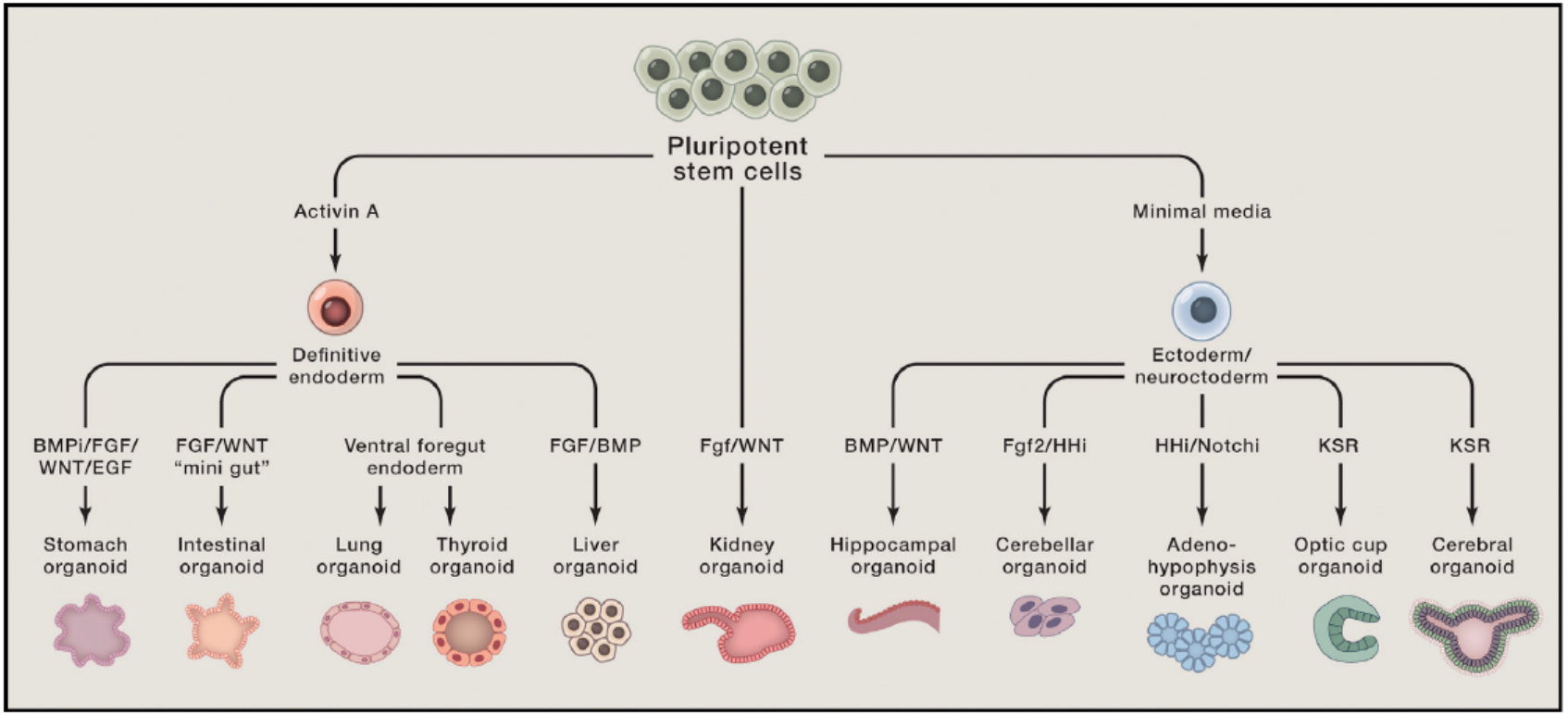

Figure 2. Schematic of the Various Organoids that Can Be Grown from PSCs and the Developmental Signals that Are Employed
Adapted from Lancaster and Knoblich, 2014.

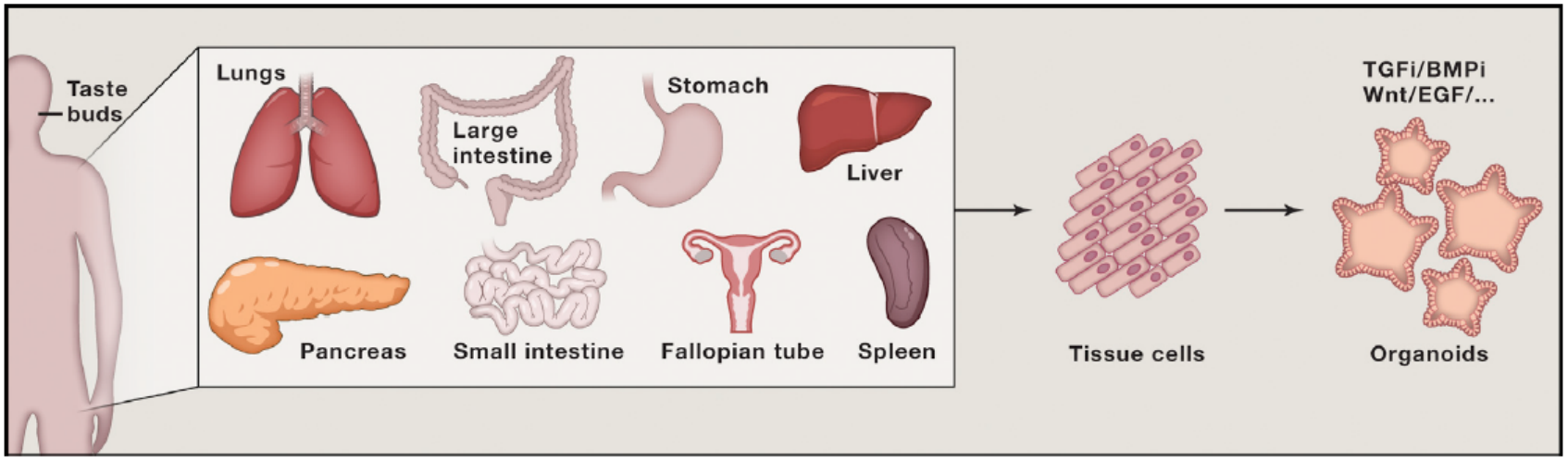

Figure 3. Schematic of the Various Regions of the Body that Can Be Cultured as aSC-Derived Organoids

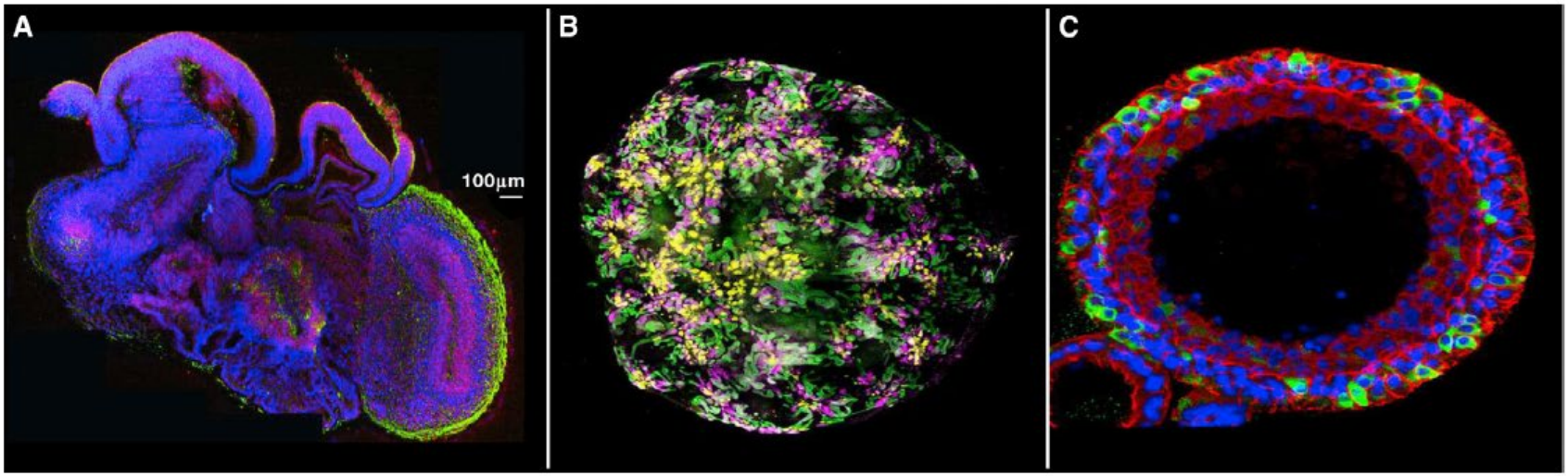

Figure 4. A "Mini-Brain" Generated from PSCs

(A) A complex morphology with heterogeneous regions containing neural progenitors (SOX2, red) and neurons (TUJ1, green) is apparent (Lancaster et al., 2013). Courtesy of Madeline Lancaster.

(B) Immunofluorescent image of an entire kidney organoid grown from PSCs with patterned nephrons. Podocytes of the forming glomeruli (NPHS1, yellow), early proximal tubules (lotus tetragonolobus lectin, pink), and distal tubules/collecting ducts (E-Cadherin, green). Courtesy of Melissa Little.

(C) 3D reconstruction of the midsection of a human aSC-derived lung organoid stained for intermediate filaments of basal cells (green), the actin cytoskeleton (red), and nuclei (blue) and imaged by confocal microscopy (N. Sachs and H.C., unpublished data).